Università
Ca'Foscari
Venezia

Master of Science Degree

in Science and Technology of Bio and Nanomaterials

Thesis

TWO-DIMENSIONAL BIO-ACTIVE NANOSTRUCTURED INTERFACES AIMED AT ACCURATE MONITORING OF CLINICALLY RELEVANT CANCER BIOMARKER PROTEINS

Supervisor
Dr. Federico Polo

Co-supervisor
Dr. Vivek Pachauri

Student
Daniele Storelli
Matriculation number
834752

Academic Year
2019 / 2020

1. Table of Contents

Table of figures

ABSTRACT

Two-dimensional (2D) materials such as graphene, are emerging as ideal candidates for the development of high performance optical and electrical biosensor platforms. 2D system like graphene, featuring unique optical and electrical properties, virtually form an active interface highly susceptible to any changes occurring in the surrounding environment, as its chemical properties can be easily and suitably tuned to offer efficient biofunctionalized hybrid materials. In fact, graphene has been used as an ideal material not only for the development of highly sensitive electrical bio-detector for point-of-care diagnosis. As a semi-metal and a plasmon-active material, it has been recently explored to develop novel opto-electronic detection strategies aimed at enhancing the current optical platforms, such as surface plasmon resonance (SPR), to monitor bio-interactions. Use of 2D materials for optical and electrical sensor platforms, however, pose significant challenges for the development of point-of-care platforms aimed at precise monitoring of bio-interactions. The work described in this thesis focuses on two critical aspects that emerge at the interface and are critical when developing accurate experimental frameworks and novel nanostructured 2D bio-nanointerfaces to precisely monitor an important class of analytes, the cancer biomarker proteins.

The first aspect towards the use of graphene for the development of biosensing interfaces is related to the heterogeneities in the 2D lattice. Lattice defects, imperfections, thickness variations–are some of the reasons that greatly influence the optical parameters of graphene employed in SPR-based studies, a technique that represents the gold standard when investigating the bio-interactions. Specific strategies, aimed at providing high quality graphene transfer onto SPR chip substrate, were employed to carry out detailed optical characterization of graphene layers and metal stacks using state of the art ellipsometry techniques. Precise measurements of the optical parameters of metal stacks and graphene layers were performed to improve the modelling of SPR behavior of graphene-based interfaces, thus obtaining heterogeneity-specific information in SPR measurements. Detailed information on lateral (related to lattice defects, graphene tears and gaps during substrate transfers) and vertical (related to layer thickness graphene and folds) heterogeneities of graphene and similar materials in SPR response and corrective procedures in the interpretation of the response are a critical step towards the accurate study of bio-interactions on 2D material interfaces. The second critical aspect this work focuses on is the use of relatively large bioactive molecules, antibodies (Abs), as specific receptor molecules for the breast cancer biomarker protein, namely HER2-ECD (the antigen). This aspect poses serious challenges for optical and electrical detection approaches

equally. In fact, for the optical detection, tethering heavy-weight receptor antibodies dramatically influence the refractive index and dielectric constant at the gold layer/sample interface, so that a high number of antigens are required to be captured in order to provide a significant SPR response. Similarly, employing Abs at an electrical transducer requires highly sophisticated engineering of biosensor interface in order to perform molecular recognition beyond the Debye-screening limits. Herein, we describe the use of nanobodies (Nbs), bioactive molecules with antigen-specific binding sites that feature a lower molecular weight and a simpler molecular structure with respect to Abs. Nbs have recently been proved as a valid alternative to Abs, potentially allowing the development of nanostructured capturing layers with proper orientation. Graphene based SPR interfaces, developed in the first part of this thesis work, were used to study molecular interactions between HER2-ECD. Surface modification of graphene based SPR interfaces and biofunctionalization with HER2-ECD proteins was optimized through a precise SPR analysis. The capturing capability of Nbs, in a wide range of concentrations, was tested and the binding response was visible already starting from 1 pM concentration.

Currently, analytical tools capable of detecting HER2-ECD level rely on commercially available ELISA (or ELISA-derived) assays employing antibodies recognizing undisclosed or unknown epitopes, providing sensitivity that very often is not adequate to detect the very low level the of cancer biomarker protein (< 12 ng/ml) in real samples. This is particularly true during the treatment of cancer in order to follow-up acquired resistance to HER2-targeted antibody therapy. Moreover, the analyses can be run only in centralized laboratories by qualified personnel, thus increasing cost and time. Therefore, development of novel 2D hybrid materials will enable new user-friendly analytical tools for rapid, reliable analysis of real samples, thus reducing the costs and time required for the analyses. In fact, a further functionalization of the nanometric layer of gold employed in the SPR with nanostructured and optically transparent materials, such as graphene, may be advantageous both in terms of further functionalization, exploiting the carbon chemistry, and electronic properties, enhancing the sensitivity. Two dimensional materials have emerged as ideal candidates for the development of miniaturized biosensor platforms. However, a comprehensive understanding of the bioanalytical mechanisms at such atomically thin 2D material is central to such developments. In this work a graphene-based bio-nanointerface was realized by transferring chemical vapor deposited (CVD) graphene on top of a gold SPR-active substrate. The graphene layers were transferred in different stacked patterns and the interfacial inhomogeneities and topological variations, induced by the transfer process were investigated by using imaging Ellipsometry, Atomic Force Microscopy and Surface Plasmon Imaging techniques. A bioanalytical framework was created to quantify the influence of the 2D layer inhomogeneities on the bio interactions and to tune the accuracy of the biosensing. A microfluidic system together with kinetic SPR analysis were deployed to investigate the biomolecular interactions between the HER2-ECD and two newly developed nanobodies

CHAPTER 1 INTRODUCTION

1.1 Cancer and its impact

Every year cancer exacts a tremendous toll on society, together with hart diseases it represents one of the primary causes of fatalities, accounting in 2018 for 9.6 million deaths.[2] This disease has affected every country under many different aspects. First of all, the quality of life of patients, which ultimately affects their family, causing often irreparable damages that weigh on entire communities. Secondly, the economic aspect, because therapeutic treatment require expensive pharmaceuticals, which often weight entirely on the Healthcare System (as it happens in Italy) and sometimes are not universally accessible, thus causing even more inequalities between rich and poor Countries. Usually, these inequalities clearly manifest in underdeveloped Countries or those undergoing development with an increased incidence of mortality rate by cancer, when compared with the richest ones. In the latter case both a better quality of life, including also a better quality and availability of food, and a stronger and well organized Healthcare System, which can provide not only better treatments but also an early stage detection, that is an important factor for assuring a positive outcome of such disease.

Cancer is associated with an abnormal cellular proliferation, sometimes with the modification of the cell's phenotype with little or no correlation to the original one. The mechanisms that lead to this drastic change can arise from different external factors, that all have in common the modification of the original genetic information. These external factors are called carcinogens and can be categorized in three different groups:

- Physical carcinogens: all the physical phenomenon capable of modifying or damaging the DNA or RNA, such as UV and ionizing radiations or ionizing subatomic alpha and beta particles,
- Chemical carcinogens: all the chemical compounds capable of covalently or non-covalently binding to the nucleotides building blocks of the genome, leading to the formation of miss pairs or mutations.
- Biological carcinogens: viruses, bacteria and parasites capable of modifying the cells genome.

Ageing is another important factor that cannot be categorized as a carcinogen, but can greatly affect the cancer incidence. With an increased age the cells' repair and proof-reading systems are less effective, giving the possibility to the genome mutations to occur more frequently and to greatly alter an already weaker immune system. This disease can usually start with a pre-cancerous lesion that can transform into a malignant tumor, if left untreated, capable of spreading to other parts of the body (metastases). The metastatic phase occurs in the later stages of development of aggressive types of cancer and can significantly complicate the treatment procedures and the outcome.

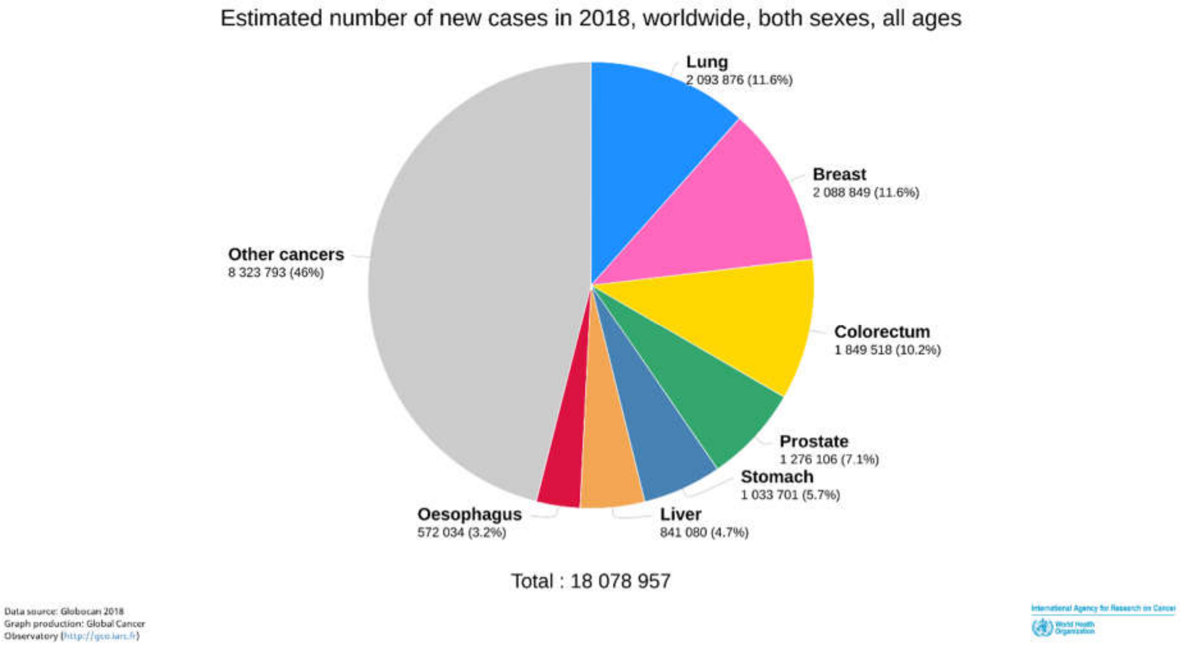

Data source: Globocan 2018
Graph production: Global Cancer
Observatory (http://gco.iarc.fr)

Figure 1. Estimated number of new cancer cases worldwide.[3]

It is well known that prevention can diminish the cancer occurrence and improve the outcome. The first direct form of prevention would be diminishing the exposure to all the exogenous carcinogens, although it cannot be completely controlled to avoid the risk. Therefore, other forms of prevention should be embraced. The most effective strategy is the timing of the diagnosis, and then of intervention and targeting of the therapy. Several studies demonstrated that the early intervention on cancer treatment can improve the survival rate and the overall burden of therapy. A critical problem for the early identification of a tumor onset is represented by the lack of evident symptoms that usually start to appear only when the disease is already at a critical stage. The need for reliable tools to diagnose cancer in its early stages has led researchers worldwide to put a lot of effort investigating the biochemical mechanisms involved in the development of tumors. Presence of characteristic biochemical signaling pathways directly involved in the neoplastic-cells development were studied in detail, which are expected to be employed as a valid alternative to the histochemical screening methods. Biomolecules such as small proteins, nucleic acids etc. related to such biochemical signaling pathways from a panel of molecular targets that can be determined as representative of various forms of stages of cancers.

1.2 Cancer biomarkers

According to the Canadian National Cancer Institute, a biomarker is “a biological molecule found in blood, other body fluids, or tissues that is a sign of a normal or abnormal process, or of a condition or disease”. [4] The nature of this biomolecules can vary from non-coding RNA, polypeptides, hormones, and protein. Biomarkers can be detected in the blood stream or inside physiological secretions such as saliva, urine, etc. Biomarkers can be used for patient assessment in multiple clinical settings, including evaluation of risk of disease, the screening for occult primary cancers, and discrimination between benign and malignant cases or between different type of malignancies. They can also be used to determine prognosis and prediction for patients who have been diagnosed with cancer, and to assess the status of the disease, either to detect recurrence or determine response or progression to therapy. [4] The possibility to employ them as an alternative method or as a support to the traditional diagnostic techniques has driven several research efforts, aimed at finding the relationship a certain biomarker with prognosis. In the past decades the technological and scientific advances in the research field had made possible to discover several biomarker relevant for clinical screening, such as the prostate specific antigen (PSA) for prostate cancer, KRAS gene mutation for colorectal cancer and the HER2-ECD oncoprotein for the breast cancer.[5] With the continuous advances in clinical methods, an increasing number of possible targeted therapies have been made possible, giving the hope for reducing the burden of therapeutic treatment and improve the disease outcome. This requires more sophisticated and minimally invasive diagnostic methods that can positively influence monitoring of patients based on reliable quantification of target disease biomarkers over the course of treatment.

1.3 Breast Cancer and the HER2-ECD biomarker

Breast cancer (BC) is the most frequent type of cancer amongst women. According to the World Health Organization (WHO) 627,000 women died because of breast cancer in the year 2018, which accounts for the 15% of all the diagnosed cases (**Figure 2**).

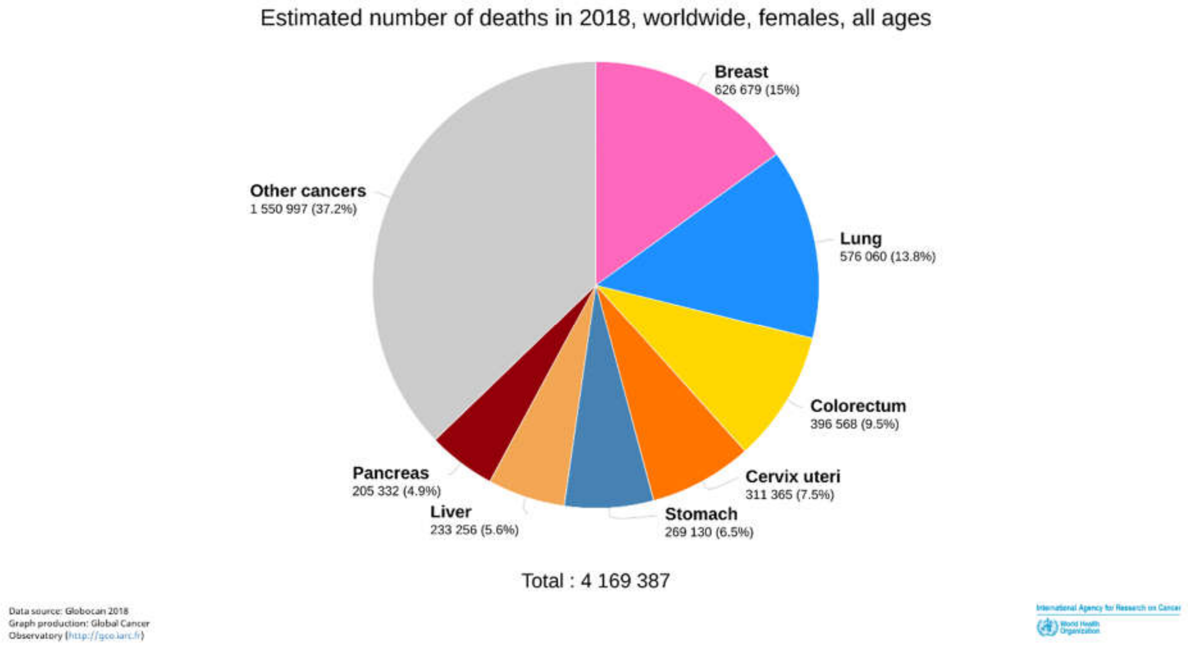

Figure 2. Worldwide incidence and distribution of cancer types among women in the year 2018 amounting for a total of 15% causes related to breast cancer.[6]

Breast cancer manifests in different types each one with its own risk factor and outcome. One of the most important factors involving in BC carcinogenesis is Human Epidermal Growth Factor Receptor 2 (HER2) gene, which is overexpressed in 20-30% of breast cancer cases.[7] HER2 oncogene was first identified as an oncogene activated by a point mutation in chemically induced rat neuroblastoma in the 1980’s and was later found to be overexpressed in some human breast carcinomas.[8] The HER2 oncogene encodes for a 185-kDa transmembrane protein, which is one member of the HER family (HER 1-4) constituting the active tyrosine kinase receptor of the surface of the cell.[7] As shown in the **Figure 3** all members of the HER family have a similar structure composed of an *extracellular domai*n with a ligand-binding site, a lipophilic *transmembrane domain*, and an *intracellular domain* with tyrosine kinase activity. The tyrosine kinase active intracellular domain is absent in the HER3 type protein. HER2-ECD protein is composed of four different subdomains, each one with a different function: Subdomain I and III are N-terminus of the protein, with a very similar structure, and unlike the other members of the HER family, they have a permanent interaction. The subdomain II is the dimerization domain: it is kept in an open conformation by the constant interaction of the sub domains I and III, enabling the HER2-ECD to bind to the other receptors of the HER family, such as the Epidermal Growth Factor (EGF). The sub domain IV is a region that is structurally homologous to sub domain II, but its function is believed to stabilize the protein and to keep it in an open conformation. The heterodimerization of this receptor with other members of the EGF family, results in the autophosphorylation of tyrosine residues within the cytoplasmic domain of the heterodimer and initiates a variety of signaling pathways that lead to cellular proliferation and tumorigenesis.[1]

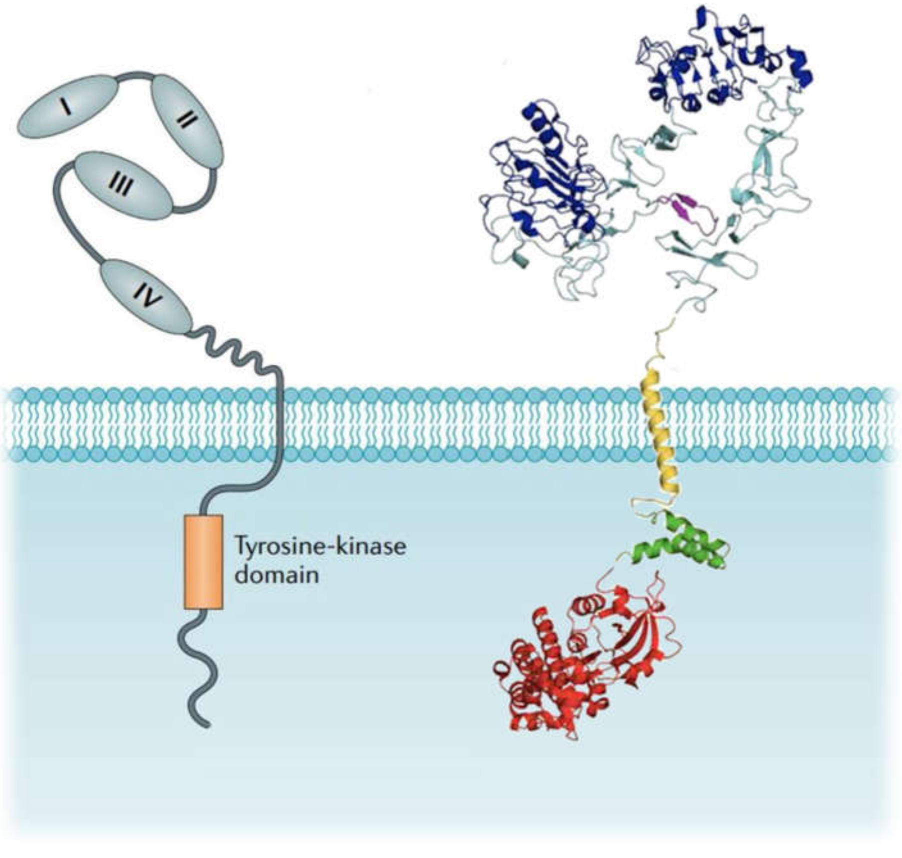

Figure 3. Schematic representation of four subdomains of HER2-ECD protein (left side) and an illustration of the three-dimensional structure of the HER2-ECD protein (right side).[1]

In 1998, a monoclonal antibody against HER2, trastuzumab, was approved for the treatment of metastatic breast cancer. The antitumor effect of the trastuzumab is given by its ability to selectively bind to the IV subdomain of the HER2 extracellular domain (ECD) inhibiting downstream signaling pathways. Trastuzumab was especially found efficacious in patients with high levels of HER2 expressions, showing that an adjuvant trastuzumab therapy could reduce the recurrence rate by half and reduce mortality by 30%.[8] The employment of targeted antitumoral therapies such as the one with trastuzumab despite being an unfettered improvement, have created the need for better and more reliable diagnostics. This is owing to the fact that uses of powerful therapeutics such as trastuzumab do not come without downsides. With respect to trastuzumab, the main drawback is a potential cardiotoxicity. An accurate and continuous evaluation of HER2 expression is therefore critical to ensure safe clinical treatment for breast cancer patients. The presence of the HER2-ECD biomarker is primarily assessed by using two different groups of techniques that relies on two different principles. The first group consists of tissue-based tests such as immunohistochemistry (IHC) and fluorescent in situ hybridization (FISH). The first technique involves selectively identifying the antigens present on the cancerous cells from a tissue section by exploiting the principle of labelled antibody, usually with a fluorescent tag, to selectively bind to the targeted antigens. The second technique works in a similar way, but this time the targeted structures are specific sequences of RNA inside the cells, that get targeted by specific RNA probes, which are eventually going to be coupled with fluorescent tags. Although both techniques represent powerful ways to assess the patient eligibility for an anti HER2 Trastuzumab treatment, these are invasive tests causing discomfort and anxiety for the patients. Further, the tissue samples require a careful handling by experienced personnel in a centralized facility and are practically limited to assessing the HER2 status of the primary tumor. Such screening methods are not compatible for a routine check-up and follow-up of HER2-ECD levels in breast cancer patients.[9] Another downside is the fact that the assessment of the tagging fluorescence that could lead to equivocal results, which would require additional test to exclude different interpretations of the results.[10] The second group of diagnostic procedure relies on the measurement of circulating extra cellular domain (ECD) of the HER2 oncoprotein, which is primarily carried out by using of the enzyme-linked immunosorbent assay (ELISA). This technique uses the binding affinity of monoclonal antibodies (mAbs) directed to the ECD that have been cleaved from the neoplastic cells by means of a metalloprotease.[9] In this case the assessment of the HER2-ECD presence is made in patient's blood sample, in which the targeted proteins are extracted together with the plasma. In the simplest form of the ELISA assay, the antigens from the sample are attached to the surface of some well plates, that have been previously coated with an immobilizing layer or with antibodies specific to the antigen. A rinsing solution is usually employed to wash away any molecules bound nonspecifically to the interface that may interfere with the test. After the successful immobilization of the target molecule, a solution containing the detection antibody is added. The detection antibody is covalently liked to an enzyme, which helps developing a visible signal, usually a color change of the solution, upon addition of a suitable substrate. To quantitatively measure the concentration of the biomarker, a colorimetric analysis is performed to correlate the intensity of the color with the concentration of the biomarker protein. The advantages of the ELISA assay are the high throughput and the fact that it can be employed during a follow up treatment of BC patients. Its sensitivity is high and usually it is sufficient to detect cancer protein biomarkers. However, the protocol beyond ELISA is expensive, requires times, and needs to be carried out only in equipped laboratories by specifically trained personnel. Although ELISA protocol is still a benchmark in clinical analyses, all the above-mentioned aspects pose a question about its versatility as cancer-screening technique.

1.4 A new HER2-ECD Biosensor

In this work, we aimed at developing novel 2D nanostructured bioactive material to provide a new sensing platform, based on surface plasmon resonance (SPR), capable of detecting and investigating the biochemical interactions between clinically relevant concentrations of HER2-ECD cancer biomarker and three newly developed specific receptors, based on nanobodies (Nb) instead of mAbs. Nbs offer several advantages over mAb. In fact, Nbs are small polypeptides chains that resemble the capturing moiety of mAbs and are produced by. Given the simpler structure Nbs can be chemically modified in specific positions and suitably bound on sensing platform while keeping the proper orientation facing the sample solution, thus being more efficient in capturing the analyte. They can also be mass produced keeping the costs low, thus making them available in large amount. To satisfy the request for a reliable user-friendly analytical method, the surface plasmon resonance spectroscopy will be coupled with a new polyimide polymer composite, that will be employed as a new substrate carrier alternative to the classic and much expensive and delicate glass slide substrate. The use of a new substrate material together with the employment of graphene has required an extensive initial characterization of the system that cover the substrate's optical constants and the lateral distribution and chemical interaction of the graphene 2D layer. The substrate and 2D layer characterization will be done by using Spectroscopic Ellipsometry, Atomic Force Microscopy (AFM) and surface plasmon resonance imaging (iSPR), whereas the biomolecular interaction will be assessed by using the surface plasmon resonance in angle scan and kinetic mode.

1.5 Ellipsometry

Ellipsometry is a very sensitive optical method, that makes use of the fact that the polarization state of light may change when the light beam is reflected from a surface. This change in polarization can be influenced by the presence of one or different thin films on the reflecting surface, which enables this technique to provide information about the film properties such as optical constants and thickness. Light is an electromagnetic wave, that is described by an electric and a magnetic field oscillating perpendicular to each other in the direction of propagation. In a simpler description, one can consider only the electric field component of the light wave, as it has a stronger interaction with matter than the magnetic field. If the light wave is a plane wave that travels along the z-axis, the electric field is always orthogonal to the z-axis, and its amplitude projection on the x-y plane produces a vector.[11] The vector's x and y components can be considered as two electric fields of two linearly polarized orthogonal light waves. When the oscillations phases of the two -x and -y components are equal, the shape traced by the oscillating field is a straight line. On the other hand, if the two components are not in phase, the resulting vector rotates along the x-y plane describing a circular or elliptical orbit.

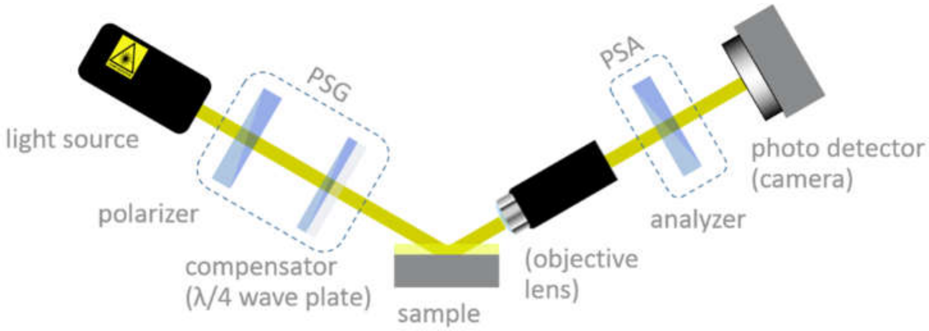

Figure 4. Optical components of an Ellipsometer.

The name Ellipsometry comes from the fact that by illuminating a material with a beam of vertical polarized light, the interaction with the material's surface transforms the two components of the electric field, generating a back reflected light with an elliptical polarization state. The same principle can be applied backwards, meaning that by illuminating a surface with the same elliptically polarized light, but with the vector rotating in the opposite direction, a back reflected vertically polarized light is generated. Nulling Ellipsometry exploits this property to

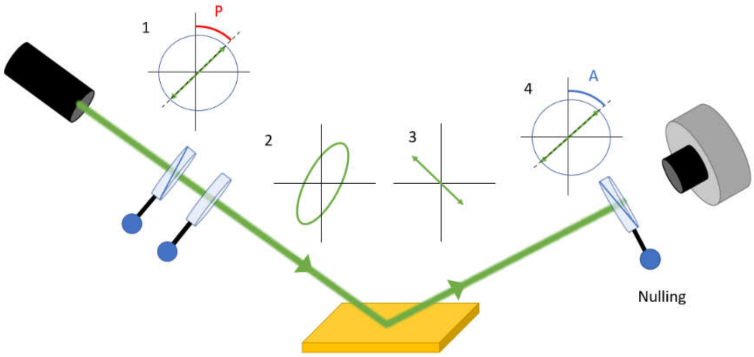

Figure 5. Representation of the Nulling Ellipsometry analysis: (1) The light wave is linearly polarized then at (2) the polarization state is modified by the compensator in an ellipsoidal state. After the reflection, the polarization state of the light beam is converted to a linear one (3) by the interaction with the sample's surface and at (4) the analyser finds the polarization's nulling angle.

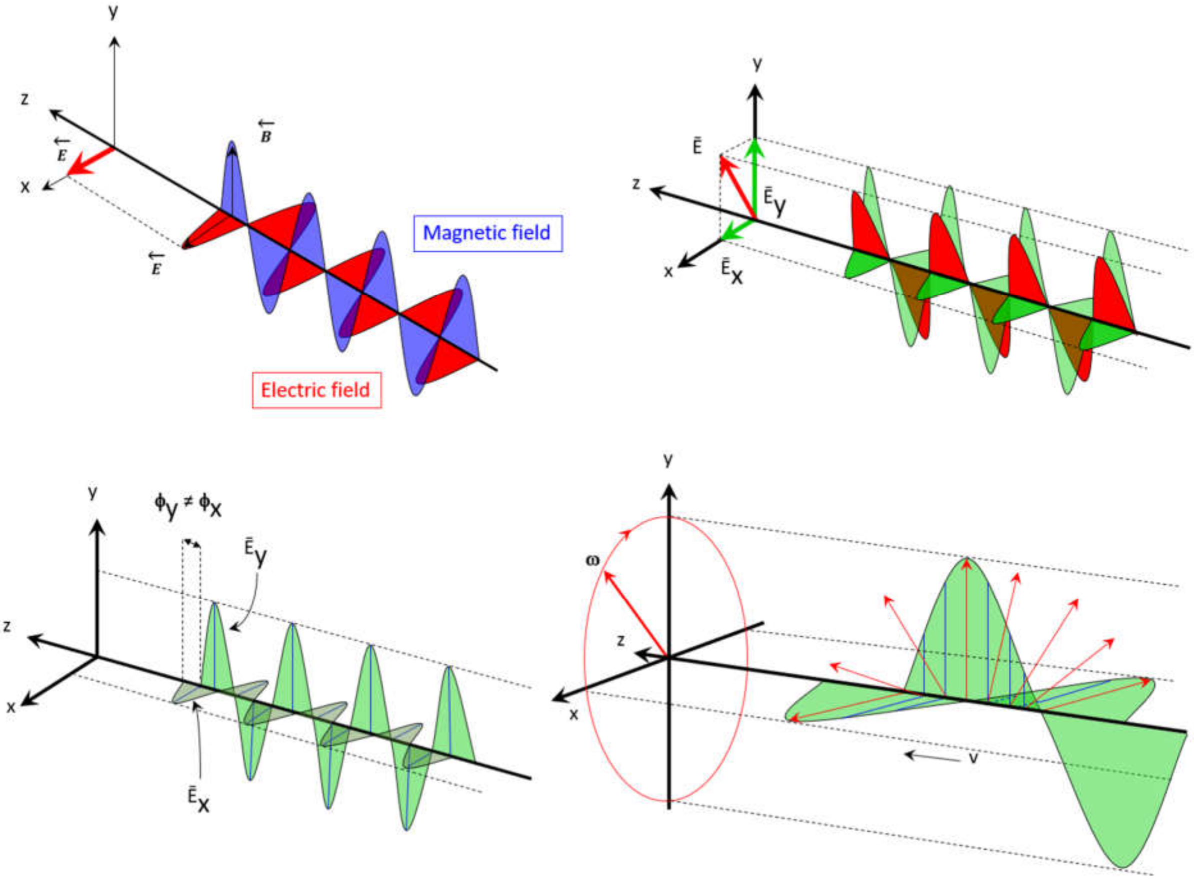

Figure 6. Schematic refiguration of the different light polarization states.

derive information about the sample's surface by means of an optical system composed of a light source, a linear polarized, a compensator, an analyzer, and a detector.

The linear polarizer suppresses all the polarization states of the incident light except the one parallel to its polarization axis, which can be rotated to produce any desired polarization angle. A linear polarizer is also be used as an analyzer, because the incident light will be blocked from hitting the back detector when it is placed with the polarization axis at 90° relative to the light beam. The compensator is an optical device capable of shifting the phase of one single component of the incident light. Therefore, when it is coupled in sequence with the linear polarizer, it can be used to generate any elliptical polarization state. It is now common to define a plane of incidence defined by the wave vector pointing in the traveling direction of the light and a line perpendicular to the reflecting surface. By using this as a new coordinate system we can define the two components of the electric field as parallel (p) and the perpendicular (s) to the plane of incidence. A Nulling Ellipsometer generates the initial elliptical light wave by rotating the linear polarizer while the compensator is kept at a stable position. The correct elliptical polarization state to create a linear polarized back reflected light is found by rotating the analyzer, until the light beam is completely blocked, or the "nulling" position was found.

It is possible to define a matrix R of the sample, that connects the incident and reflected light's vectors E:

$$\begin{bmatrix} E_{p,out} \\ E_{s,out} \end{bmatrix} = \begin{bmatrix} R_{pp} & R_{sp} \\ R_{ps} & R_{ss} \end{bmatrix} \mathrm{X} \begin{bmatrix} E_{p,in} \\ E_{s,in} \end{bmatrix} \tag{1}$$

The concept of ellipsometry is to measure the change of the polarization state of the light wave to obtain information about the sample (the matrix R).[11] For isotropic materials the two components R_{sp} and R_{ps} are equal to 0, transforming R into a diagonal matrix, from which two ellipsometric angles Ψ and Δ can be defined:

$$\frac{R_{pp}}{R_{ss}} = \frac{|R_{pp}|}{|R_{ss}|} \times e^{i(\delta_{pp}-\delta_{ss})} = \tan\Psi \, e^{i\Delta} \tag{2}$$

Where Ψ is and angle which tangent gives the ratio of amplitude change for the *p* and *s* components and Δ denotes the relative phase change of the *p* and *s* components of the electric field vector.[11] The Fresnel equations relate Ψ and Δ to the film thickness and optical constants, however, in most cases the equations cannot be inverted to determine all the unknown parameters, and therefore a different approach is used: At first the parameters Ψ and Δ are measured using a light beam with different wavelengths and angles of incidences, then an optical model is developed and its output is fitted until it equals the Ψ and Δ parameters of the measured data. When the model is correctly fitted to the experimental data, the optical constant that can be derived are a close approximation of the real ones.

1.6 Surface plasmon resonance

Surface plasmon resonance (SPR) is an optical phenomenon involving the resonant oscillation of conduction electrons in a thin layer of noble metal or in nanostructured metal particles (gold, silver).[12] The first documented observation of this phenomenon dates to 1902, when Robert Williams Wood noticed that when metal-backed diffraction grating was shone by a polarized light, a pattern of unusual dark and light bands appeared in the reflected light.

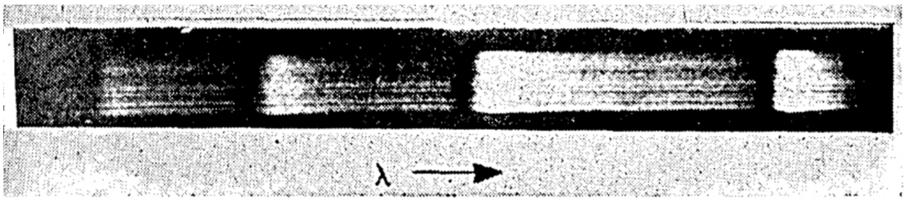

Figure 7. A spectrogram exhibiting Wood's anomalies as first observation of the surface plasmon resonance

Later, theoretical studies of Rayleigh and experiments conducted by Pines and Bohm suggested that the phenomenon was due to energy losses for the excitation of conducting electrons on the noble metal's surface. It was only in the late 1960's that Kretschmann and Otto were able to fully demonstrate the phenomenon, creating the foundations of a powerful analytical technique that nowadays is broadly employed in the research field. The basic components of a surface plasmon spectrometer are a monochromatic light source, usually made of a He-Ne laser with λ at 632.8 nm, two linear polarizers, an optical prism and a detector respectively coupled with two rotating goniometers.

The optical phenomenon responsible for the surface plasmon resonance is taking place on the back of the prism, where the incoming photons of the laser light are physically interacting with the free moving electrons of a thin noble metal layer. This interaction occurs under the conditions of total internal reflection (TIR), taking place at the interface between two media with different optical densities, which in this case would be represented by the glass prism and the air or water. When a light ray is travelling from a media with a high refractive index n_1 to a media with a lower refractive index n_2, the TIR occurs only when the angle of incidence is greater that a certain value, called critical angle θc, given by the equation:

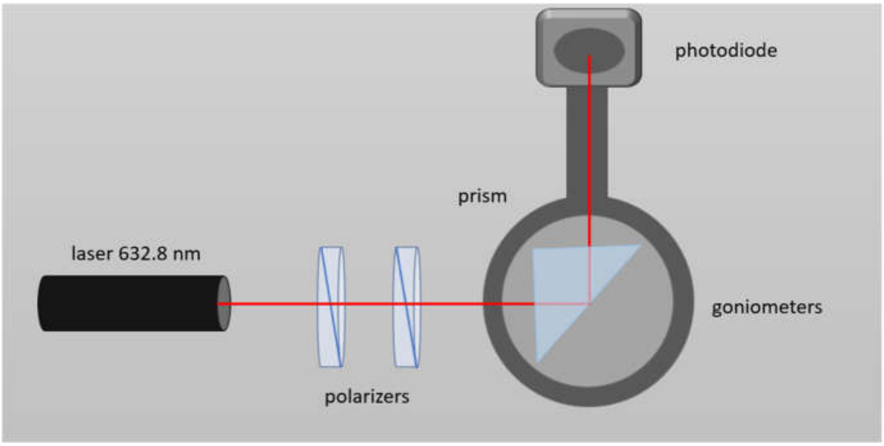

Figure 8. Refiguration of the basic components scheme of a Surface plasmon spectrometer.

$$\theta_c = \sin^{-1}(n_1/n_2) \tag{3}$$

If the light beam is at an angle lower than the critical angle θc, it passes through the less dense medium. On the other hand, if the light ray impinges with an angle greater than θc, it is reflected back inside the denser medium.

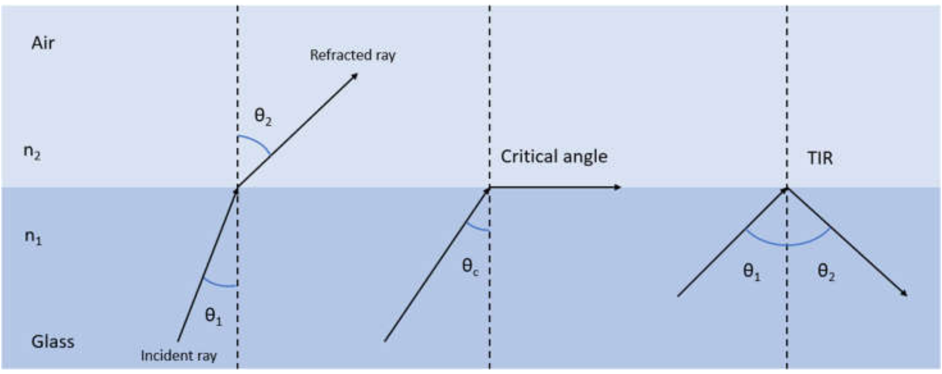

Figure 9. Representation if the total internal reflection.

Although the light is reflected inside the prism, the electric and magnetic fields partially propagate beyond the reflecting surface with a distance on the order of the wavelength, creating an evanescent wave. The intensity of this evanescent wave I(z) decays exponentially with the perpendicular distance z from the interface:

$$I(z) = I_0 e^{-z/d} \tag{4}$$

$$d = \frac{\lambda_0}{4\pi}\left[n_1^2 \sin^2\theta - n_2^2\right]^{-1/2} \tag{5}$$

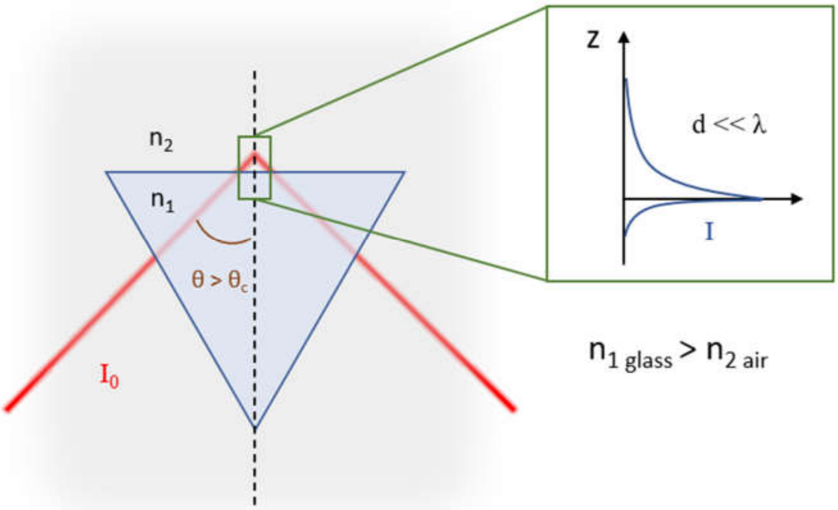

Figure 10. Schematic refiguration of the total internal reflection (TIR) with the formation of a decaying evanescent wave at the interface between the glass prism and air (left side). It can bee seen how the intensity I of the evanescent wave quickly decays with the distance Z from the prism surface (right side)

Where I_0 is the initial intensity, λ_0 is the wavelength, n_1 and n_2 are the refractive indexes of the two media.

The polarization state of the incident light is also influencing the propagation depth of the evanescent wave, which is optimal only when the electric field is set perpendicular to the surface or with a P polarization state. This can be achieved by placing two linear polarizers before the prism, which can be both used to control the intensity and the polarization state of the light beam.

When a thin noble metal layer is placed on the reflecting side of the prism, its free moving electrons will undergo a physical interaction with the evanescent electromagnetic wave. The best noble metals suitable all practical uses in SPR spectroscopy is gold, because of its inertness and defined resonance peak. The gold deposition is usually done by a two-stage plasma evaporation process, either on a glass slide or directly on the prism's reflecting surface. In the first stage a 5 nm titanium or chromium adhesion layer is directly evaporated over the glass surface, followed by the gold evaporation forming the final thickness of SPR active thin film of about 50 nm. The first adhesion layer is necessary to provide a stable anchoring surface to the gold. The newly evaporated metal layer is now forming an almost 2D material, whose electrons show their momentum components predominantly constrained on the x-y directions. By solving the Maxwell's equation for a multilayer system, two different vectors can define:

$$K_X = \left(\frac{2\pi}{\lambda}\right)\sqrt{\varepsilon_0}\,\sin{(\theta)} \tag{6}$$

$$K_{SP} = \left(\frac{2\pi}{\lambda}\right)\sqrt{\frac{\varepsilon_1\varepsilon_2}{\varepsilon_1 + \varepsilon_2}} \tag{7}$$

Where K_X is the wave vector of the light travelling inside the glass prism, K_{SP} is the wave vector of the surface plasmons, ε_0 is the permittivity of the glass, ε_1 is the permittivity of gold and ε_2 is the permittivity of the air. The surface plasmon resonance is possible only when the K_X vector is matching with the plasmonic vector K_{SP}. This condition can be achieved by changing wavelength λ, the permeability ε_2 and ε_0 or the angle θ. The wavelength and the optical permittivity can be considered as constants for the state of high stability of the He-Ne lasers and the high purity of optical glass prisms currently available. The only variable parameter left is the angle θ, which is the angle to which the prism should be rotated to reach the surface plasmon resonance.

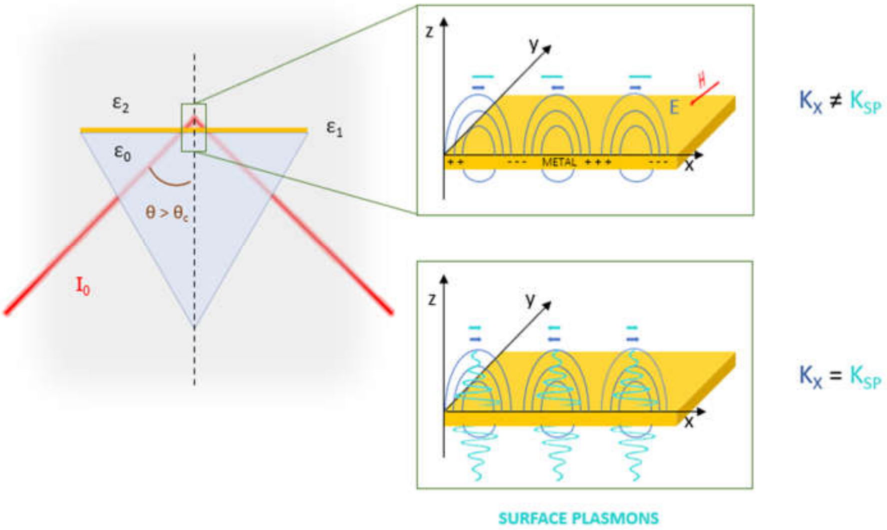

Figure 11. Schematic representation of the SPR working principles.

When a photodiode sensor is coupled with the rotating prism, the measure of back reflection (% of reflectivity) from the prism can be plotted over the angle θ creating this way a sensogram similar to the one in **Figure 12**, where the plasmonic resonance is visible as a steep decrease of

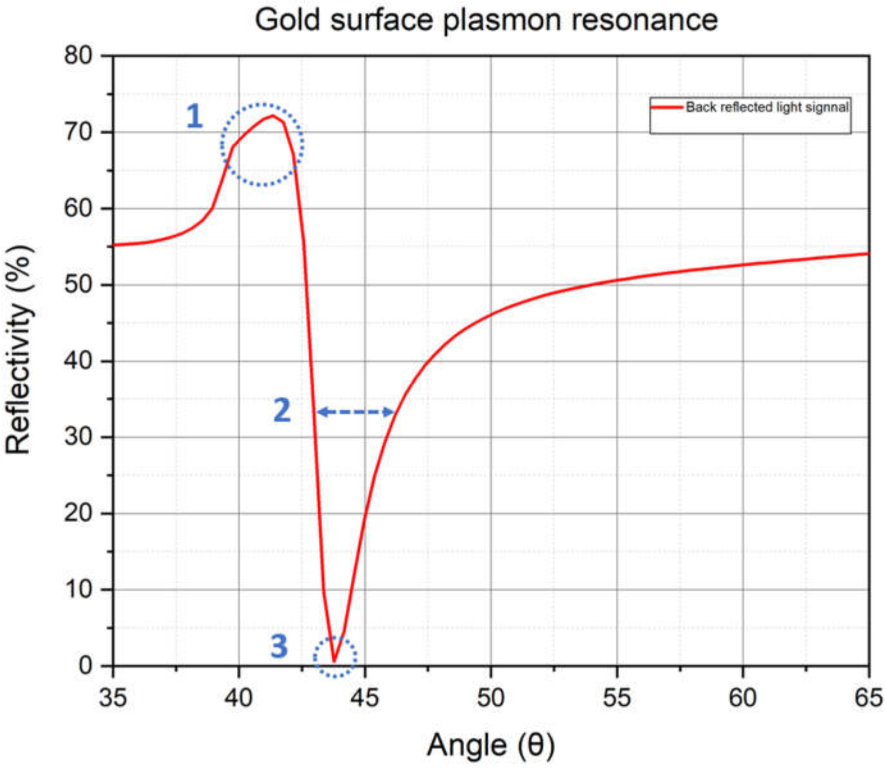

Figure 12. Example of SPR sensorgram obtained with a gold chip. Three different area of interest are evidenced: (1) the total internal reflection angle, (2) the full width at half maximum, (3) the resonance angle.

the reflectivity. This phenomenon is due to the oscillating plasmons that dissipate part of the energy absorbed from the incoming photons as heat.

The optical permittivity and the refractive index of the media can be expressed in their complex forms:

$$\varepsilon = \varepsilon' + i\varepsilon'' \tag{8}$$

$$\tilde{n} = n - ik \tag{9}$$

Where ε' and ε'' are the real and complex parts of the dielectric constant ε, and n and k are the real and complex components of the refractive index $\tilde{n}$, where k is also called extinction coefficient.
$\tilde{n}$ and ε are connected together by the following relation:

$$\tilde{n} = \sqrt{\varepsilon} \tag{10}$$

With respect to the sensorgram in **Figure 12**, three different areas of interest can be determined: the first one is the edge of the total internal reflection (TIR) that depends on the value of the critical angle θ_c, determined by the difference of the dielectric constants of the two infinite media, represented by the prism and the external medium, usually air or water. The second important point of interest is the resonance angle, whose position is determined by the optical constants of the prism, the surrounding medium, and the type of metal.[13] The full width at half maximum is the third characteristic point of the sensorgram, where the broadness of the resonance peak is determined by the imaginary part of the metal's dielectric constant.

Any chemical or physical modification of the gold layer affects its refractive index. Consequently, the value of the plasmons' vector K_{SP} changes, thus causing a new different plasmon resonance angle. An SPR based sensor can detect refractive index changes smaller that 10^{-5} [14], which can be used to accurately determine the added layer or adlayer thickness and the kinetics of molecular or biomolecular interactions. However, this sensitivity of the refractive index change will only extend for the length of the evanescent wave, therefore the sensitivity decreases with the distance. Usually the maximum distance required from the gold layer to achieve a good sensitivity is around 300 nm, being the optimum distance around 100 nm. [12] When developing a biosensing surface it is important to consider how the interaction between the ligand and the receptor is going to affect the refractive index shift and consequently the sensitivity of the detection. To achieve the best response at low analyte concentrations, the noncovalent interaction between the analyte and the ligand should induce the highest refractive index change and the interaction should take place as close as possible to the gold surface. The refractive index directly reflects a mass density, that can be defined as mass per unit volume of adsorbed material. This relationship between the refractive index and the density can be expressed as follows:[15]

$$d = M * N = \frac{M}{A}\left[\frac{(n^2 - 1)}{(n^2 + 2)}\right] \tag{11}$$

Where M is the molecular weight, N is the number of moles for unit volume and A is the molar refractivity of the material. The above relationship can be used to calculate the adsorbed mass in μg/cm^2:

$$m = dt = \frac{0.1M}{At}\left[\frac{(n^2 - 1)}{(n^2 + 2)}\right] \tag{12}$$

Where the thickness t is expressed in nanometers. When the adlayer is composed of multiple layers with different refractive indices, the refractive index value is replaced with a linear combination of the molar reflectivity and the number of moles per unit volumes:[15]

$$\frac{(n^2 - 1)}{(n^2 + 2)} = A_1N_1 + A_2N_2 + A_3N_3 + \cdots A_nN_n \tag{13}$$

From the above equations we can conclude that when designing a biosensor, the best way to increase the sensitivity towards biomolecular interaction is decreasing the molecular weight ratio between the receptor and the analyte, with the analyte carrying the higher mass. SPR biosensor sensitivity can be decomposed into two components – sensitivity to refractive index changes produced by the binding of analyte to biomolecular recognition elements on the sensor surface SRI, and the efficiency E, with which the presence of analyte at a concentration c is converted into the change in the refractive index n:[16]

$$S = \frac{\Delta P}{\Delta n} \cdot \frac{\Delta n}{\Delta M} = S_{RI} \cdot E \tag{14}$$

Where P is the sensor output, which turns out to be the incidence angle Δn in this case. The latter one is the amount of refractive index shift by the biomolecular binding. M refers to the moles of biomolecules binding onto the surface, S_{RI} represents the sensitivity to the refractive index change and E the adsorption efficiency of the target biomolecules.[17] The sensitivity of a SPR biosensor based on the angle shift detection can be defined for an antibody – antigen interaction, as the ratio between the difference of the resonance angle and the refractive index:

$$S_{\theta n}^{L} = \frac{\Delta\theta_{res}}{\Delta n_D} \left(\frac{deg}{RIU}\right) \tag{15}$$

Where:

$$\Delta\theta_{res} = \theta_{res\,\langle antigen\rangle} - \theta_{res\,\langle antibody\rangle} \tag{16}$$

$$\Delta n_D = n_{D\langle antibody\rangle} - n_{D\langle antigen\rangle} \tag{17}$$

When considering biomolecular analysis, the interaction between the receptors on the sensor's surface and the analyte in solution is way too fast to be accurately measured by acquiring successive sensorgrams. This is the reason why all SPR instruments that enable bio essays have also a kinetic analysis mode. During a kinetic SPR measurement, before any introduction of the analyte, a first sensogram is acquired over the biosensor's substrate to determine its exact plasmonic resonance angular dip. The substrate's resonance angle is then set as a reference point for all the successive kinetic measurement, by keeping the instrument at that particular angle throughout all the measurement, usually at the lower flank of the decreasing reflectivity within the surface resonance peak, as it can be seen in the **Figure 13**. When the analyte binds to the gold layer chip surface, the resonance of the surface plasmon is shifted to higher angles due to the build-up of the dielectric layer. This shift causes the reflectivity at the flank of the resonance peak to increase over time until a constant value of the reflectivity is reached. The new obtained kinetic sensogram shows a change in reflectivity plotted over the time instead of the angle, providing the shift of the resonance dip with respect to a static point of reference.[13]

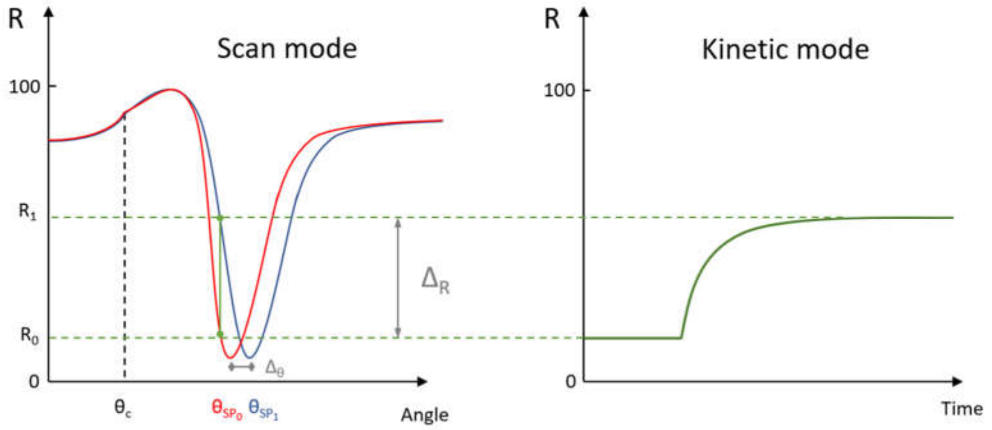

Figure 13. Schematic representation of the kinetic mode principles. By keeping the measurement on the lower flank of the surface resonance peak, the surface modification of the adlayer determines an angle shift that in the kinetic mode is registered as a difference in reflectivity.

1.7 2D materials based SPR platforms

Recently the use of 2D materials has emerged as a valid way to improve the sensitivity of SPR biosensor, since they can broaden the surface functionalization and improve the plasmonic resonance response. The discovery in 2004 from Novoselov and Geim of a reliable approach for producing monolayer graphene,[18] has drawn interest toward the development and employment of graphene as a sensing substrate. More recently in 2009, a new robust and reliable method has been developed to produce large area monolayer graphene trough the chemical vapor deposition (CVD) process.[19] This process consists on the growth of a graphene monolayer on the surface of a metal substrate, usually either Ni or Cu, with low molecular hydrocarbons such as CH_4. The implementation of graphene in a SPR biosensor can bring many advantages, due to its unique electronic and optical properties. Monolayer graphene has a characteristic honeycomb network of carbon atoms sharing together sp^2 hybridized orbitals that form strong in-plane covalent σ bonds. While the 2s, $2p_x$ and $2p_y$ orbitals contribute to form the in-plane bonds, the remaining $2p_z$ orbitals form an out of plane π bonds matrix, which are perpendicular the graphene planar structure.[20] The half-filled π bonds are responsible for the free moving electrons, these charge carriers of zero effective mass, also called Dirac fermions, can travel for micrometers without scattering even at room temperature.[21] The presence of an atomic layer with similar properties on a gold surface alters the propagation constant of the surface plasmons, which ensures the modification of the sensitivity to refractive index change, leading to and increased sensitivity.[17] The high surface to volume ratio together with π-π interactions of graphene can significantly improve the adsorption properties of a substrate and compared to gold. Moreover, its well-known surface chemistry increases the versatility for the functionalization of different receptor molecules.

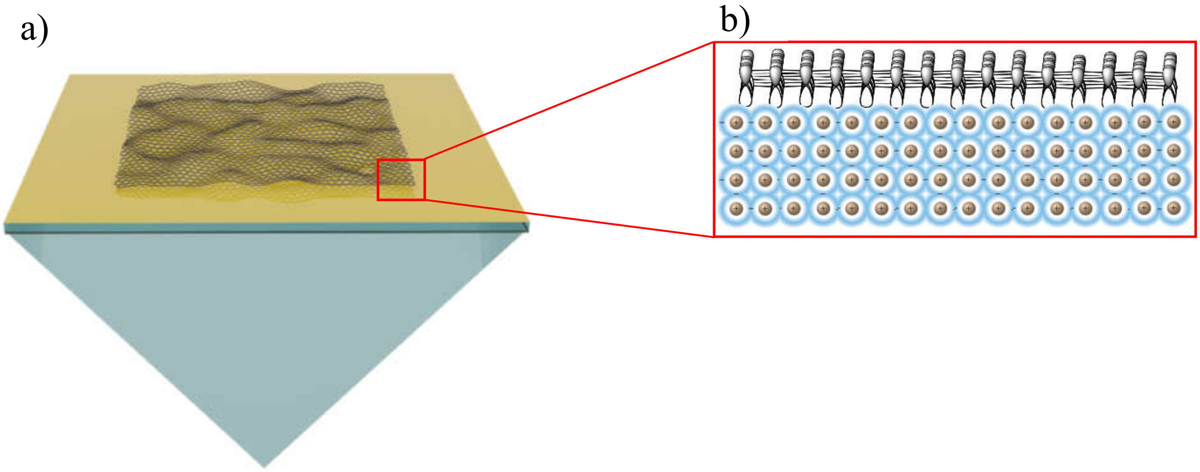

Figure 14. a) Representation of the graphene layer over the SPR chip, b) scheme of the graphene's SPz orbitals interacting with the electron cloud of the underlying metal.

CHAPTER 2 EXPERIMENTAL

2.1 Chemicals

N-(3-Dimethylaminopropyl)-N′-ethylcarbodiimide (EDC), N-hydroxysuccinimide (NHS), Ethanolamine 99,5%, Sodium Acetate buffer 2M pH 5.2, Toluene (99%), polystyrene pellets, purchased from Sigma-Aldrich. Hydrogen peroxide (H_2O_2 30%), Hidrocloric acid (HCl 37%), purchased from Technic France. Toluene (99.8%) purchased from Rotisol. Acetone and Isopropanol purchased from Michrochemicalg GmbH. PBS-Tween tablets (pH 7.4) purchased from Merck. Sodium hydroxide (NaOH) purchased from Gie-Tech.

2.2 Biomolecules

The HER2-ECD biomarker employed in this thesis work was purchased from Sino Biological, the nanobodies were produced by Prof. Angelini at Ca’Foscari University of venice

2.3 Surface Plasmon Resonance

All the SPR analyses and measurements were carried out with the RT2005 spectrometer by Res-Tec. As detailed in **Figure 15**, the light source is a He-Ne laser (λ=632.8 nm), which was stabilized with an additional monochromator and correctly aligned with two reflecting mirrors and two iris diaphragms. Two linear polarizers, placed between the two diaphragms, were used to control the light intensity and the polarization state. The prism, made of high refractive index LaSF9 glass (n = 1.8449), was coupled with the sample’s glass slide with an index matching oil (Cargille Series B n = 1.7000). The prism and the glass slide were held together with a metal

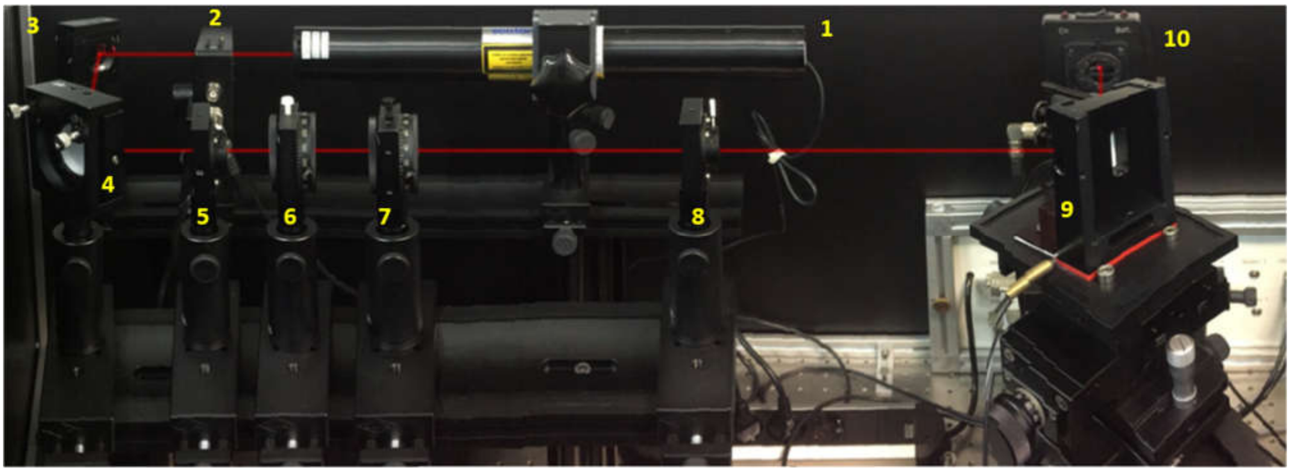

Figure 15. Res-Tec RT2005 setup, on the picture are visible: (1) Laser source, (2) monochromator filter, (3) and (4) 45° mirrors, (5) and (8) iris diaphragms, (6) and (7) linear polarizers, (9) Sample holder, (10) photodiode

sample holder (**Figure 16a**), which was placed over the goniometer (**Figure 16b**) by sliding it inside two parallel guides.

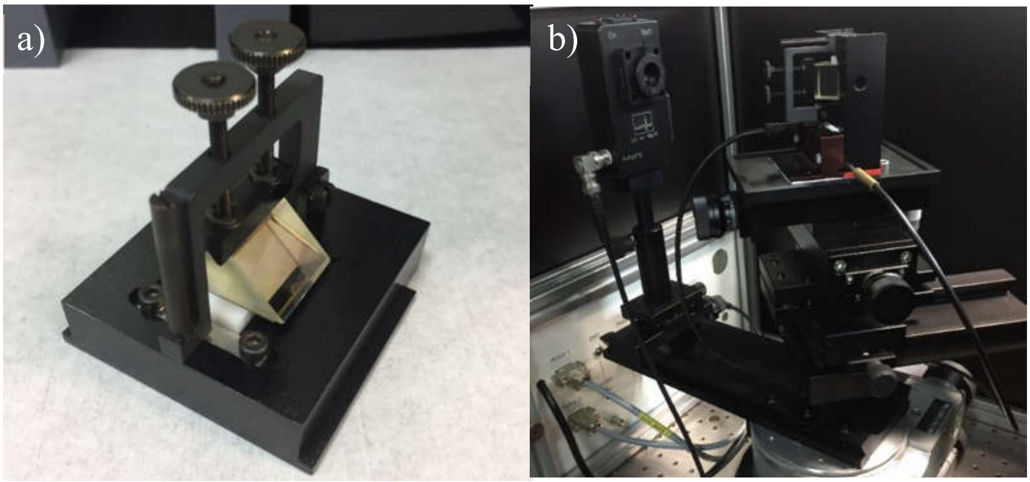

Figure 16. Detailed pictures of the sample holder: in the picture a) the sample holder is remove from the instrument and the prism with the gold chip beneath are clearly visible; in the picture b) the sample holder is positioned on top of the rotating goniometer.

The surface plasmon resonance was measured with a photodiode, which is connected to a second goniometer that moves with an angle two times greater than the sample's goniometer. The movement of the two goniometers, the temperature of the sample holder and the photodiode were connected to an external drive and a lock-in amplifier, respectively, that are both connected with a serial port to a desktop PC. The WasPlas software was used to control the instrument and acquire the sensrograms.

2.4 Ellipsometry

All the ellipsometric measurements were carried out with the Ellipsometer Nanofilm_EP4 from Accurion (**Figure 17**). The light source is a multi-wavelength laser with λ ranging from 300 to 1000 nm. The entire system is controlled via PC through the proprietary software EP4. The data modelling to obtain the substrates optical constants were carried out by using the proprietary software EP4 model and DataStudio by Accurion.

Figure 17. Nulling ellipsometer Nanofilm-EP4 employed in the present thesis work.

2.5 Atomic force microscopy

All the atomic force microscopy (AFM) measurements were carried out with the Veeco Dimension 3100 atomic force microscope. And the obtained images were modelled and measured by using the free software Gwyddion.

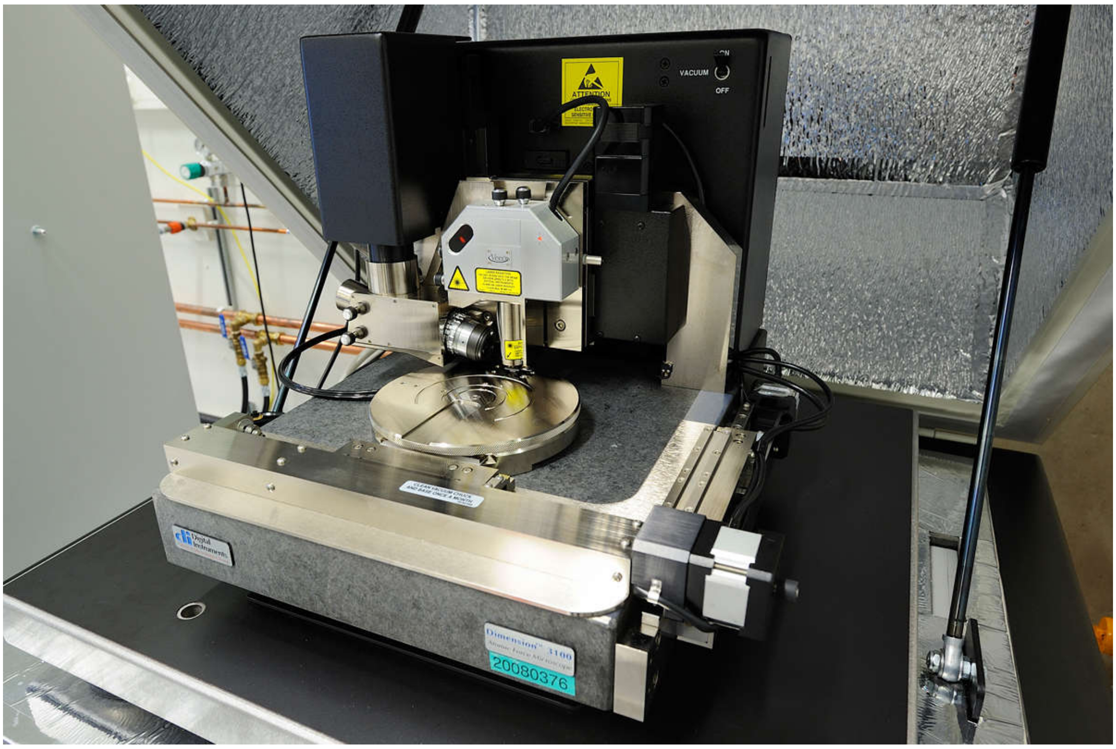

Figure 18. Veeco Dimension 3100 atomic force microscope used to acquire all the AFM images. Image taken from https://amolf.nl/veeco-dimension-3100-afm

2.6 Optical microscopy

All the optical microscopy images were obtained by using the Nikon Eclipse L150.

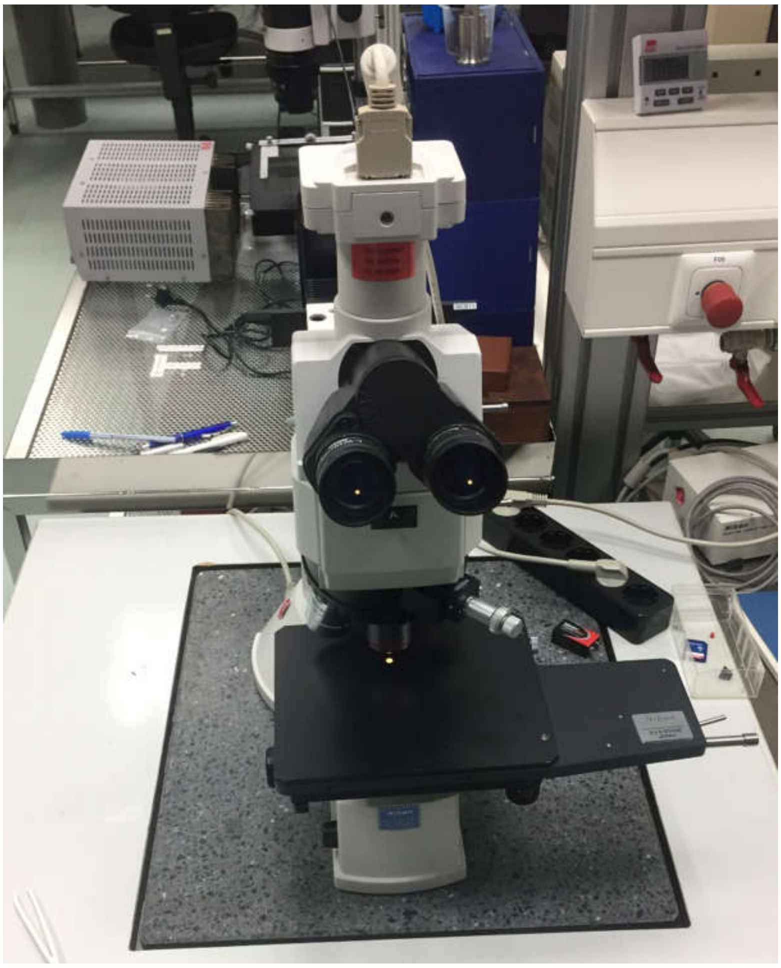

Figure 19. Nikon Eclipse L150 optical microscope used to acquire all the optical microscopy images.

2.7 SPR Chip preparation

2.7.1 Flexible SPR chips based on transparent polyimide

Polyimide foils present physical properties that make them eligible for the use as gold substrate carriers in the surface plasmon resonance spectroscopy. The characteristic high glass transition temperature (T_g), high surface strength and low thermal expansion make them suitable to carry the gold substrate, as they can withstand the thermal evaporation process without displaying stress deformations. The high optical transmittance ~ 90% and low surface roughness enables them to be used as a substitute to high refractive index glass or quartz chips, with the advantage of having a lower production cost. The characteristic elasticity of these composite materials can be exploited to create optical devices with an overall better versatility and robustness, which are important aspects to consider when developing a reliable device. In this work the polyimide foil was chosen with a thickness of 100 μm, necessary to provide enough structural rigidity when placed at the interface between the fluidic cell and the prism. The gold-plated chips were obtained by cutting them out of larger polyimide foils on which the gold layer deposition had been previously performed.

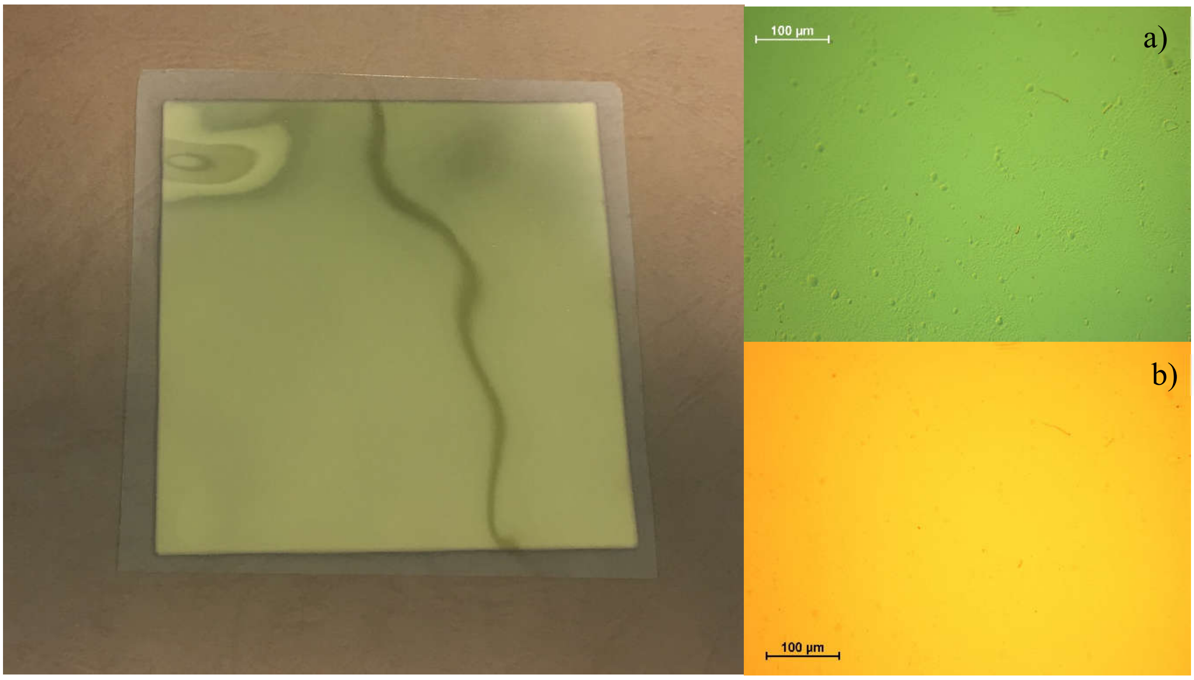

Figure 20. Picture and optical microscope images of the gold sputtered polyimide foil. a) Optical microscope image obtained with the differential interference contrast (DIC) setting; b) optical microscope image obtained with unpolarized light.

To maintain the substrate’s surface as straight as possible, the size of the chips was increased in order to put the foil under tension by anchoring it on the sides of the sample holder with the aid of adhesive tape. The applied tension was necessary to decrease the distortion of the reflected laser beam and the formation of air bubbles within the contact matching oil layer, both caused by the deformation of the polyimide layer introduced by the pressing action of the prism holder and the shape of the fluidic cell.

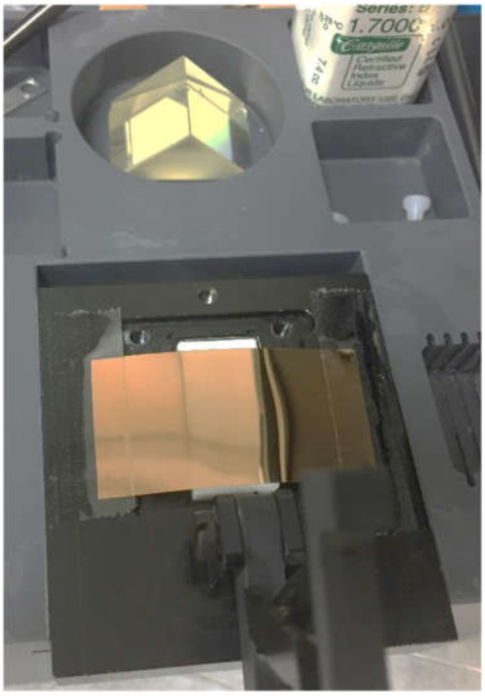

Figure 21. Picture of the tensioning method employed to increase the smoothness of the polyimide chip.

To avoid any leakage during the fluid elution, a double-sided tape was used as the main gasket, by placing it at the interface between the fluidic cell and the polyimide chip.

2.7.2 Initial gold chip preparation

Gold chip substrates were employed for the graphene transfer and the biofunctionalization, which were obtained from a polyimide foil with a thickness of 100µm. An important step prior to the surface modification was an accurate characterization of the substrate’s optical constants with the nulling ellipsometry technique. This was necessary to avoid the use of the optical constants present in the literature, since they were not measured for the same materials and experimental procedures. In particular, the purity of the two metals employed and deposition processes can be sufficient to provide different optical constants, which might eventually affect the final data modelling and the accuracy of the experiments. To ensure an accurate measurement of the substrate's optical constants, the same two metals used to create the thin metal layer on the sample were deposited separately on top of two different glass slides with a thickness of ~ 100 nm. The 100 nm thickness was chosen to make sure that the ellipsometer's light beam was completely absorbed by the metal layer, therefore avoiding any interaction with the underlying glass layer that could have led to inaccuracies of the measurements. The measurement was performed with the following setup: The wavelength of the light source spectrum ranged from 360 – 1000 nm and was divided in 150 sampling intervals. The incident angle was set to be measured at three different angles of the light beam, starting from 61° with 3 steps of 7° increments until 75°. The nulling of the ellipsometer was set to four zones to provide an optimal accuracy of the measurements.

2.7.3 Fluidic cell design

Since all the surface activation and functionalization steps were going to be performed directly on the SPR system, the presence of a good fluidic system was necessary to carry out all the measurements. For this reason, three different fluidic cells, each one with a different central fluid channel (**Figure 23**), were designed with a CAD software to ensure the best compatibility with the chip and SPR system. Teflon was chosen as the main material to produce the fluidic cells, because its chemical inertness is optimum to avoid interaction with the eluting fluid. To prevent any fluid leakage from the system, a Polydimethylsiloxane (PDMS) gasket was placed at the interface between the gold chip and the fluid cell. During the SPR kinetic measurements the fluidic cell with the best suited central fluid channel (**Figure 23c**) were employed. The remaining fluidic system consists of a pump, an exchangeable syringe, and a waste solution container. A capillary tube with the diameter of 300 µm was used to connect all the parts together using the shortest distance possible to employ the least amount of solution during the analyses.

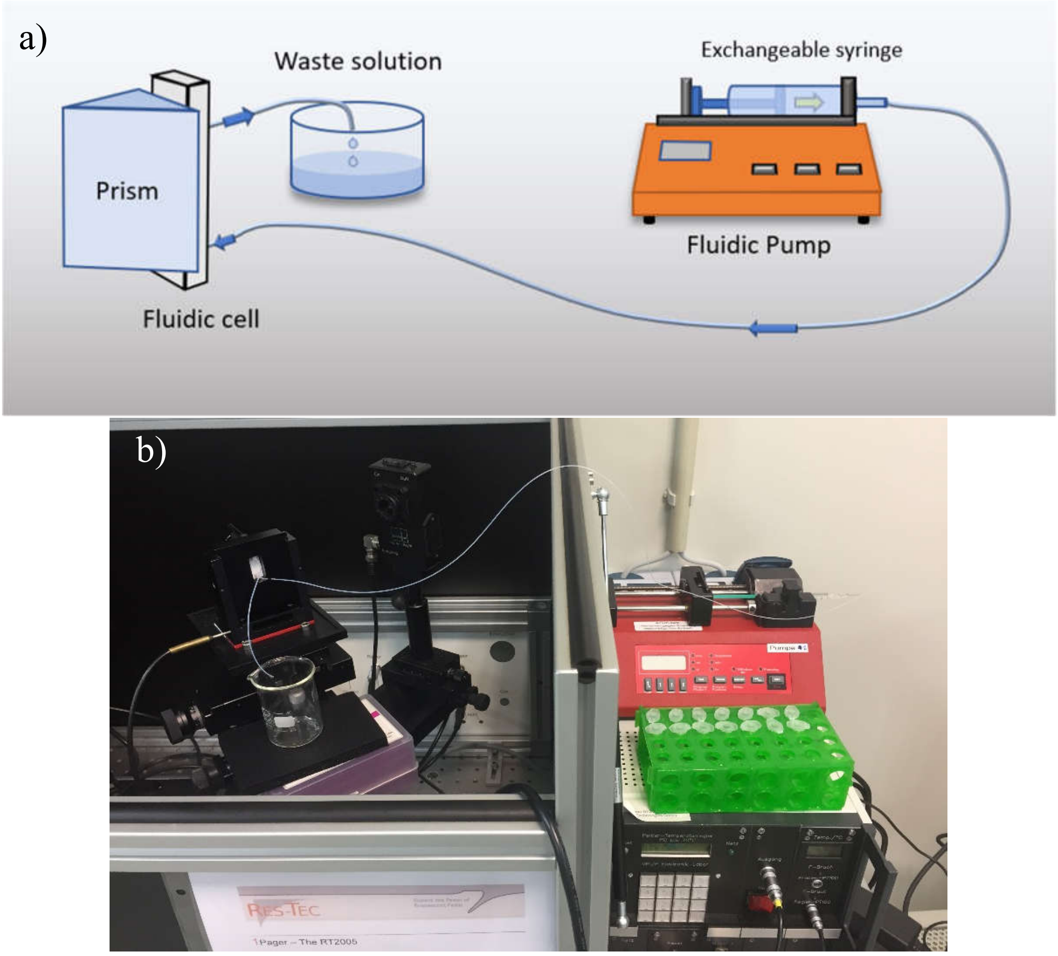

Figure 22. a) Schematic representation of the fluidic system employed for the kinetic measurements. b) Actual setup employed during the measurements.

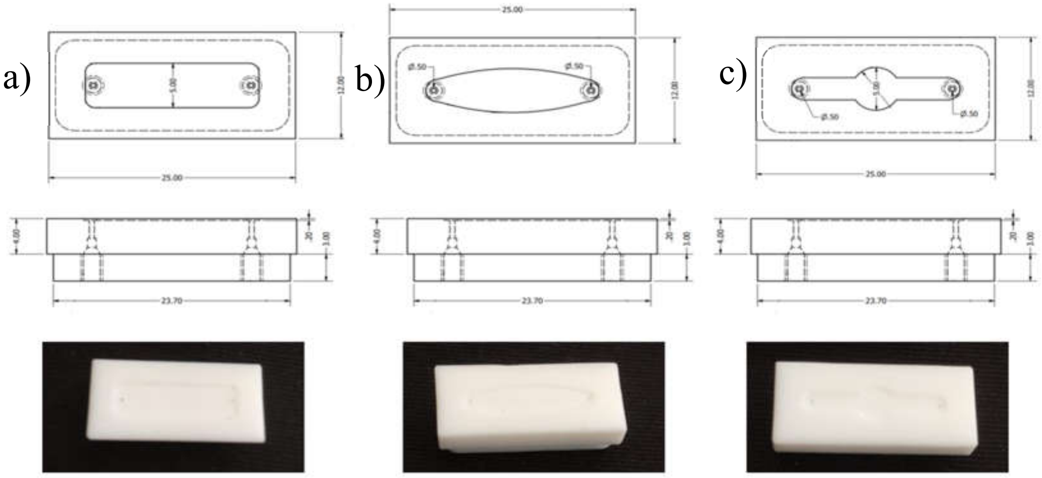

Figure 23. Schematics and pictures of the three different models of fluidic cell designs. From the cross section the two fittings for the inlet and outlet pipes are visible, whilst from the top view the different designs of the fluid channels are visible.

2.7.4 Graphene transfer

From the copper foil carrying the CVD graphene (**Figure 18a**), a square piece of 5x5 mm was cut for each golden chip to be transferred with graphene. The dimension of the copper pieces was chosen to cover all the central area of the chip in contact with the fluid. Then each cut copper foil was coated with a polystyrene. The polystyrene layer was applied by coating the CVD side of the copper foil with a solution prepared by dissolving 70 mg of polystyrene in 3 mL of toluene. The presence of the polystyrene layer was crucial to provide mechanical support for the graphene monolayer during the later etching and phishing procedures.

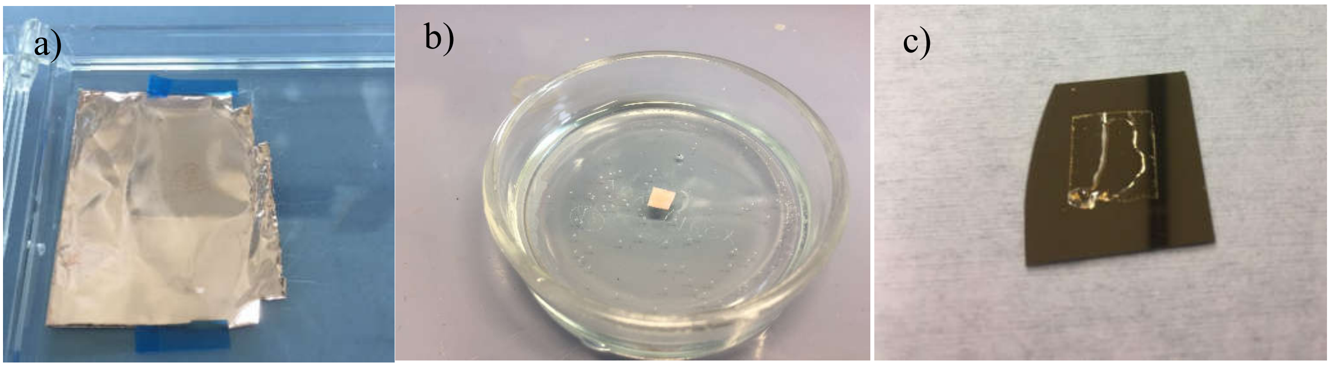

Figure 24. Graphene transfer process. a) Copper foil with the CVD graphene on top. b) 5x5 mm polystyrene coated copper foil section floating on the etching solution. c) Gold chip after the phishing process of the floating polystyrene layer.

The freshly coated copper foils were placed inside a drying oven at 40°C for 5 minutes to remove the toluene. After the drying process, the copper pieces were placed over an etching solution to remove the copper (**Figure 18b**). The etching solution was prepared by mixing 42 mL of deionized water with 2.5 mL of 30% H_2O_2 and 7.5 mL of 37% HCl. After all the copper layer had been removed, on the etching were left only the polystyrene layers with the attached CVD graphene. The polystyrene flakes were carefully transferred on two deionized water baths to clean off any copper ions left and to remove all the air bubbles generated by the etching process. At this point the floating polystyrene layers were lifted out of the water bath by phishing them with the gold chips. The gold chips on which the polystyrene layers had been successfully transferred were placed in a toluene bath over night to dissolve away the polystyrene layer. A different wax mediated graphene transfer was performed on a gold glass chip, which was later used to study and determine the physical and optical characteristics of the graphene layer. In the wax mediated graphene transfer, on the 5x5 mm cut copper foil instead of the polystyrene layer a paraffin layer was deposited. The paraffin layer was formed by drop casting on top of the copper flake a solution prepared by mixing paraffin and toluene in a 1:1 ratio. After the paraffin solution was drop casted on top of the copper flake, the copper layer was etched away with the same etching solution used during the polystyrene method. After cleaning the remaining wax layer with the graphene attached in two DI water baths, the wax layer was fished with the gold chip and subsequently the wax layer was removed from the chip surface by immersing it in a toluene bath at 60°C overnight. The advantage of using a paraffin mediated transfer is that paraffin is a very efficient support layer, that can be easily eliminated afterwards during the cleaning process. The isotropic expansion of wax upon heating performs a stretching action on the graphene layer that results in smoother graphene transfers with less wrinkles and surface defects.[22]

2.7.5 Surface activation with EDC/NHS protocol

The use of a solution of N-(3-Dimethylaminopropyl)-N′-ethylcarbodiimide (EDC) and N-hydroxysuccinimide (NHS) is a well-known and reliable protocol employed to conjugate biomolecules on biosensor's surfaces. It is frequently referred as a "surface activation" process, since the two employed reagents EDC and NHS provide a succinimide-ester terminated surface layer, ready to form a covalent amide bond with an amino linker or with the lysine groups of the target protein.[23] Due to high conversion efficiency, mild reaction conditions, excellent biocompatibility with little influence on the bioactivity of target molecules, and much cleaner products,[24] the EDC/NHS protocol became a standard for activating carboxy terminated substrates. The chemical reactions responsible for the surface activation are described in **Figure 19**, where graphene oxide is employed as substrate. Two separate solutions of the reagents should be prepared in advance and mixed right before starting the bioconjugation procedure, and immediately placed in contact with target surface. The reaction can be divided in 2 main steps: in the first step of the reaction, the nitrogen of the carbodiimide deprotonates the carboxylic group of the graphene, forming a carboxylate anion that will perform a nucleophilic attack on the carbodiimide's electrophilic carbon, thus leading to the formation of an O-acylisourea ester. In the second step of the reaction, the hydroxyl group of the NHS molecule performs a nucleophilic substitution on the electrophilic carbon of the newly formed ester, forming an amine reactive NHS ester and a urea molecule leaving group as by-product.

An important aspect to consider while setting up the protocol is the pH value of the buffer solution, because it plays two key roles. (i) During the initial surface activation, to increase the EDC/NHS reaction rate, where it shows an optimal value around 8.5, whereas it is inhibited below 3.5. (ii) During the bioconjugation shown in **Figure 29**, where a pH should be chosen considering both the isoelectric point of the ligand protein and the ionization of the carboxylic groups of the substrate. Usually to satisfy both previous conditions, the pH should be set with a value of 0.5 – 1 unit below the isoelectric point of the ligand to maintain its amino groups positively charged. However, the pH should never be set with a value below 4, otherwise the

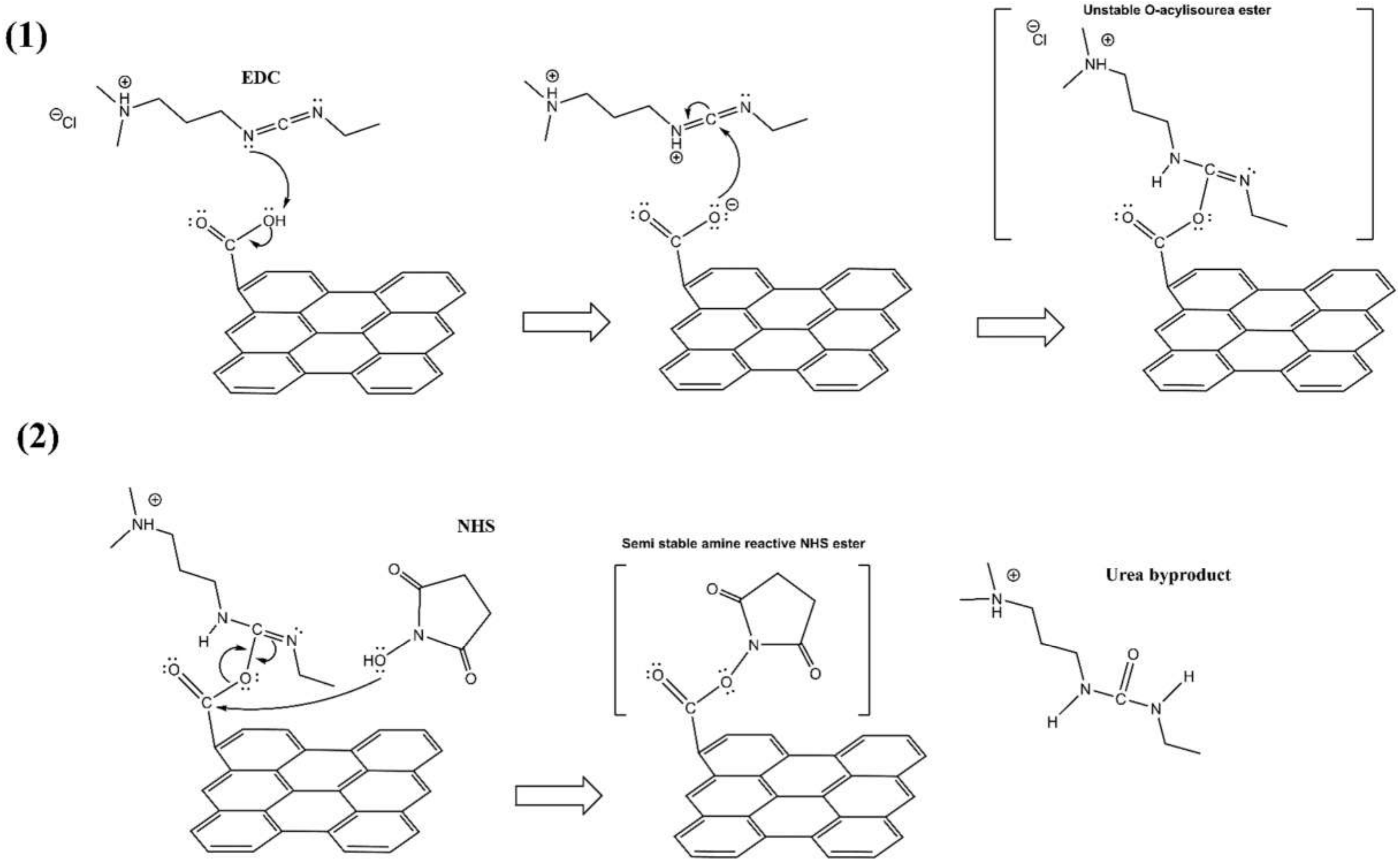

Figure 25. Schematic representation of the EDC/NHS surface activation reaction. (1) In the first part of the reaction of the reaction the O-acylisourea leaving group if formed, (2) in the second reaction the NHS reacts with the carbonyl forming the final semi stable NHS-ester, ready for the amide group formation.

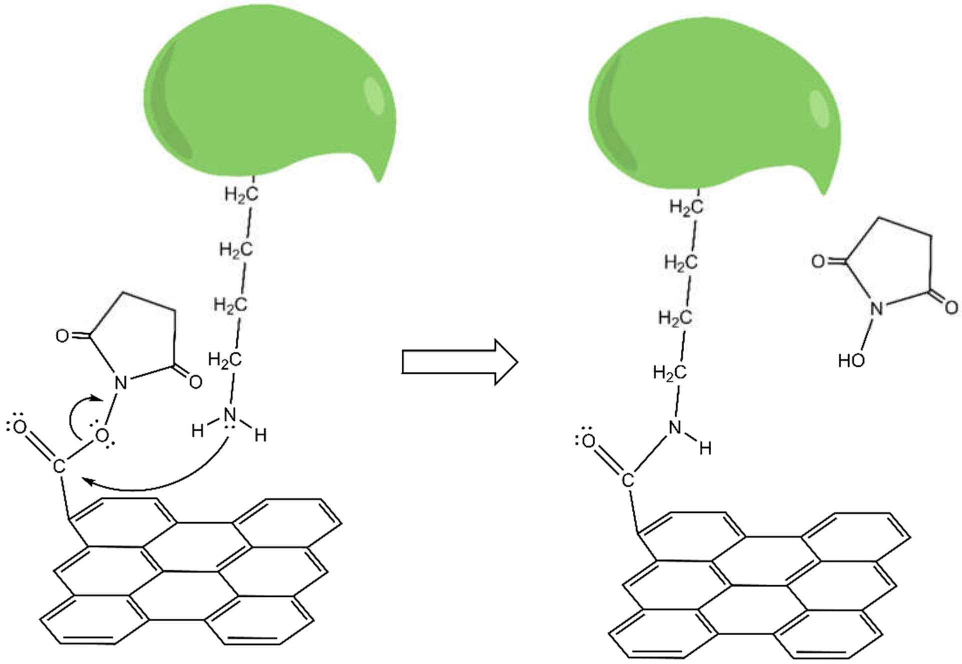

Figure 26. Amide bond formation between the carbonyl and the HER2-ECD lysine amine group.

carboxyl groups would lose their negative charge, necessary to establish an electrostatic attraction between the substrate and the ligand also known as preconcentration.[25]

The preconcentration effect of the electrostatic interaction between the substrate matrix and the biomolecules is important during the bioconjugation because it brings in closer contact the amino groups of the biomolecules with the activated NHS-esters, creating a more favorable condition for the formation of the amide bonds.[26]

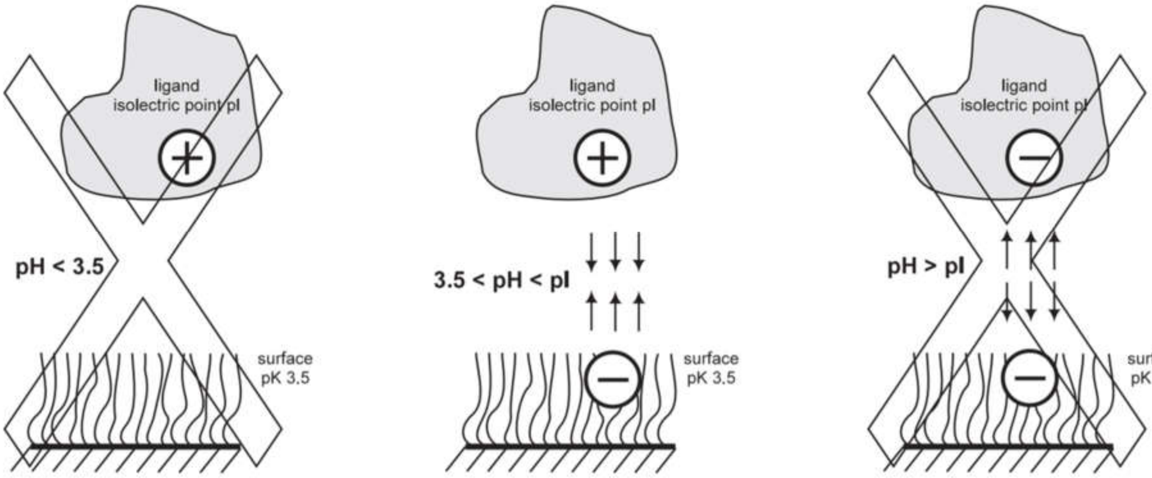

Figure 27. Schematic representation of the preconcentration effect or electrosorption of the biomolecule on the sensor's surface. It can be seen how the pH value relative to the isoelectric point affects the electrostatic interaction between the biomolecule and the sensor’s surface.

CHAPTER 3 RESULTS AND DISCUSSION

3.1 Initial gold chip characterization

3.1.1 Gold and Titanium optical constants

The dispersions of both the titanium and gold layers were calculated in the wavelength range from 360 to 1000 nm. The values obtained at 633 nm were later employed in the software for the simulation of the plasmonic resonance. The dispersion obtained from the online literature (https://refractiveindex.info/) were also taken into account to evidence the difference in the dispersion coefficient, which could be originated from the different experimental conditions and metal purity. Even though the values do not seem to differ that much, the resonance angles and the peak shapes were affected in a greater way when fitting the data with the simulation software. This difference can eventually influence the modelling for the adlayer thickness and refractive index.

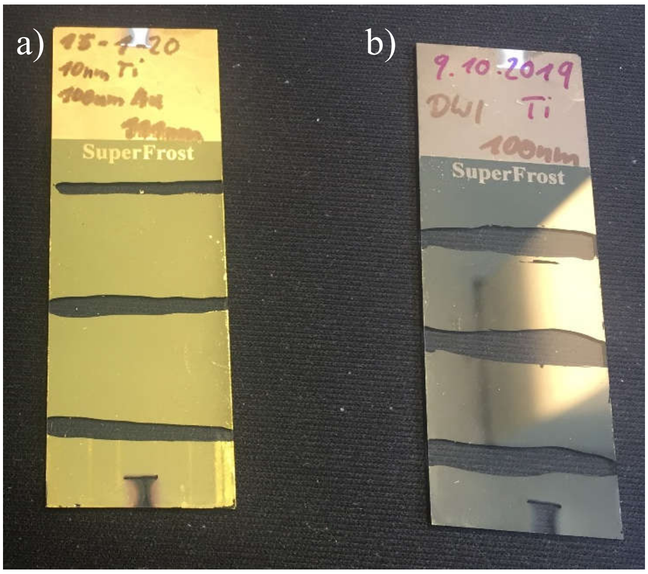

Figure 28. Glass slides used for the Spectroscopic Ellipsometry measurements. a) Glass slide with a 10 nm Ti adhesion layer and 100 nm Au layer. b) Glass slide with 100 nm Ti, in this case no adhesion layer is present because titanium does not need one.

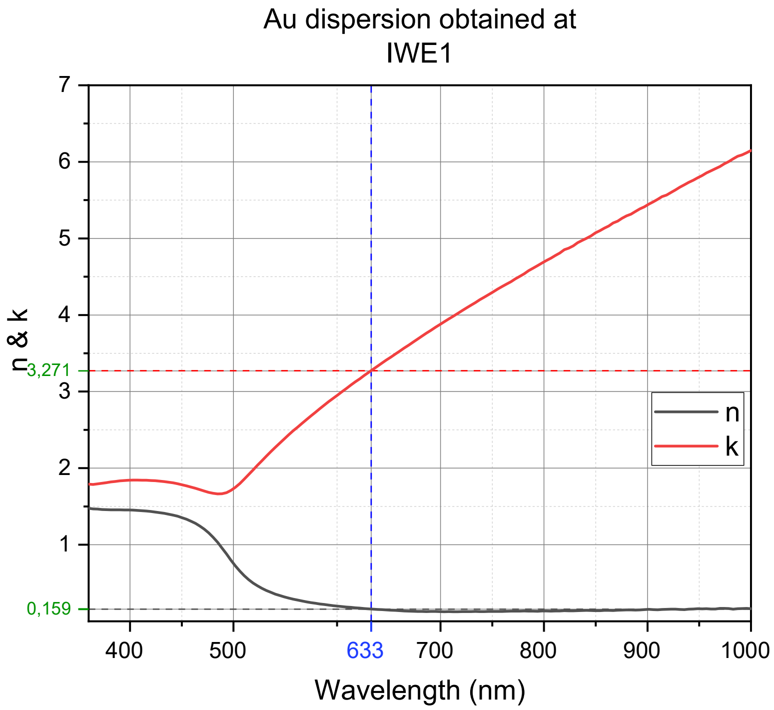

Figure 29. Refractive index dispersion of the 100nm Au layer deposited on the glass slide present in **Figure 26a**, obtained with the Ellipsometer of the Institute of Materials for Electrical Engineering 1 (IWE1) at RWTH Aachen.

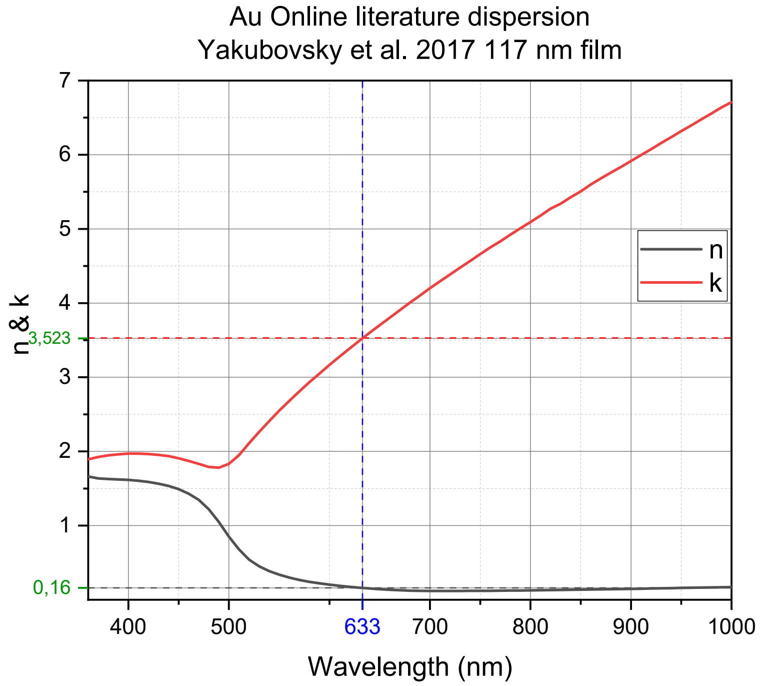

Figure 30. Gold refractive index dispersion obtained from the online database available at the website https://refractiveindex.info/?shelf=main&book=Au&page=Yakubovsky-117nm

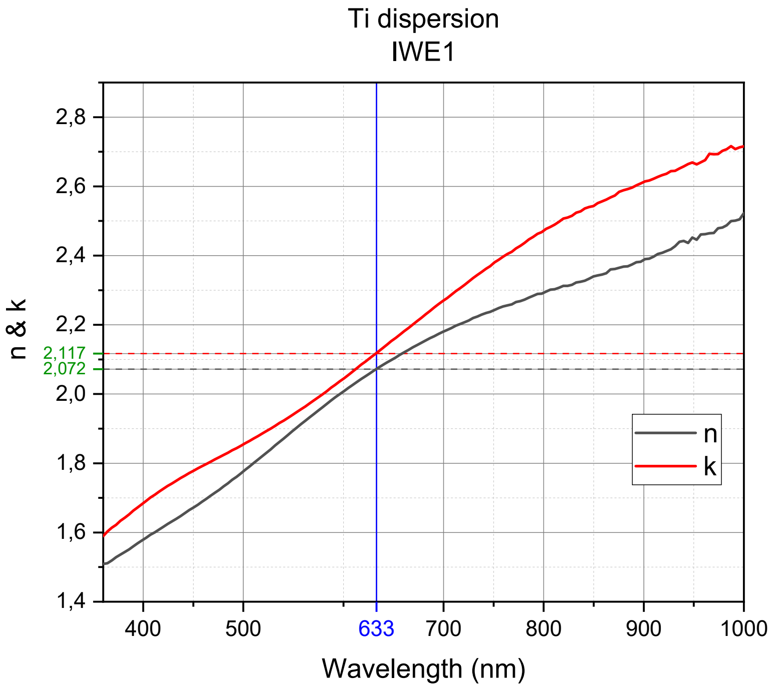

Figure 31. Refractive index dispersion of the 100nm Ti layer deposited on the glass slide present in **Figure 26b**, obtained with the Ellipsometer of the Institute of Materials for Electrical Engineering 1 (IWE1) at RWTH Aachen.

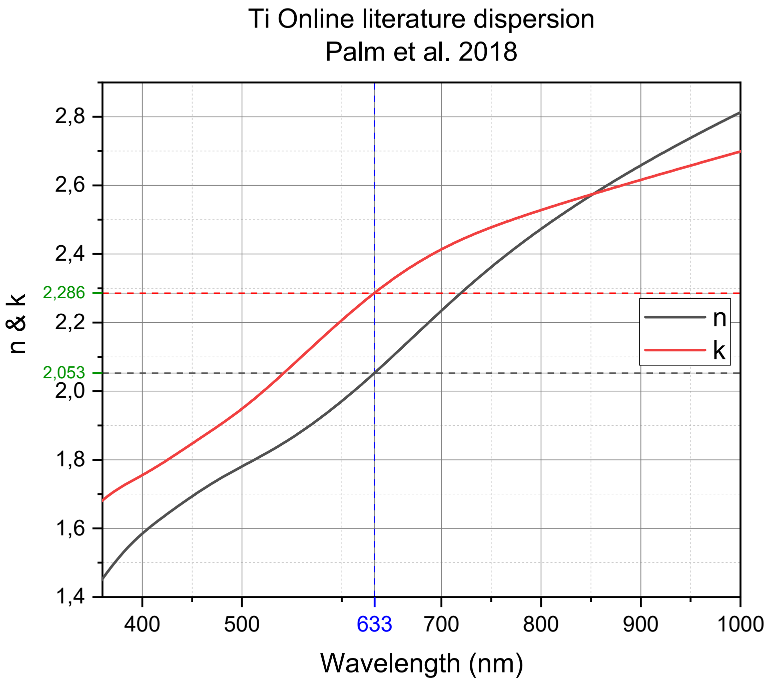

Figure 32. Titanium refractive index dispersion obtained from the online database available at the website https://refractiveindex.info/?shelf=main&book=Ti&page=Palm

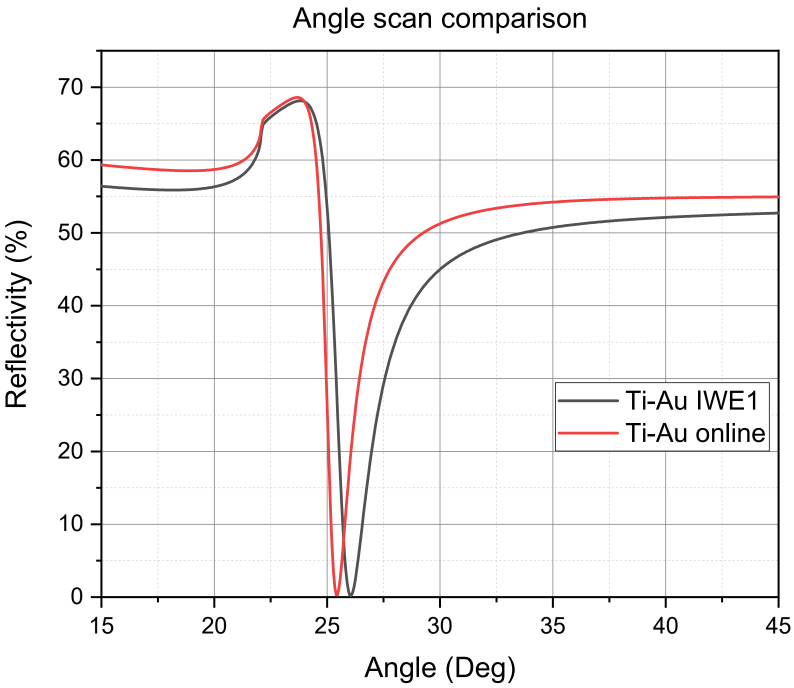

Figure 33. Comparison between the simulated SPR angle scan sensorgrams generated by using the optical constants obtained from the online literature Au and Ti dispersion in the **Figures 28 and 30**, and the Au and Ti optical constants obtained from the ellipsometric measurements at the IWE1 in the **Figures 27 and 29**. It is clearly visible how both the resonance angles and the peak shapes were affected by the difference of the optical constants.

3.1.2 Graphene optical and physical properties

The optical constants of graphene were measured on a chip where a successful and very clean graphene transfer had been carried out. This time instead of polystyrene, a paraffin wax mediated transfer was opted. The paraffin offers a good structural support to the graphene layer and its different thermal expansion properties can be exploited to perform a stretching action on the graphene monolayer, resulting in a lower presence of wrinkles and surface imperfections (**Figure 32**). To accurately chose the areas for the measurements a map of the transferred graphene was made by merging several optical microscope images together, as shown in **Figure 32**. The detailed map of the graphene distribution was used to precisely chose the areas where to perform the ellipsometry, AFM and optical microscope measurement which were easily compared afterwards. As it can be seen from the map in **Figure 32**, the graphene surface

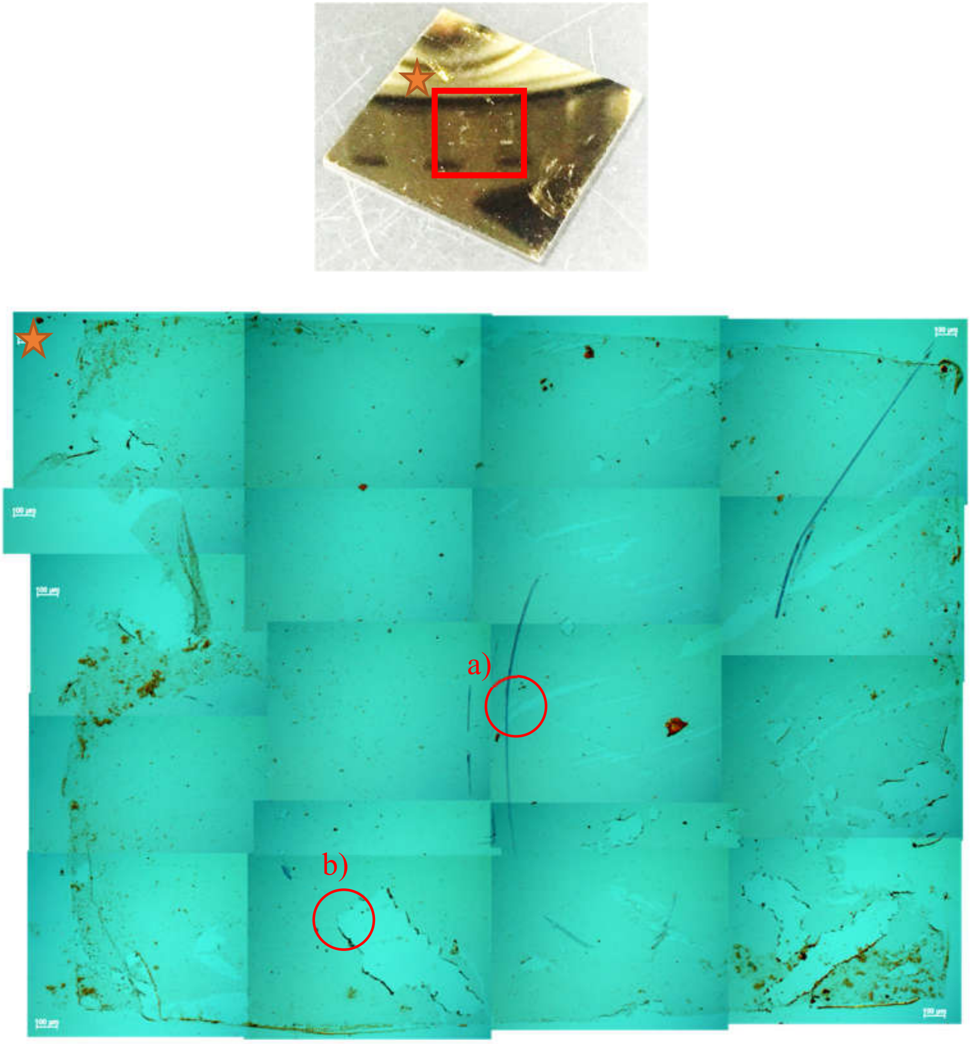

Figure 34. In this figure a map of the wax mediated graphene transfer was created by merging several optical microscope pictures taken at high magnification. a) and b) are the upper right and lower left regions respectively, where the Ellipsometry, AFM and optical microscope analyses were performed. A picture of the gold chips was placed on top for using it as a reference when positioning the sample for the analyses.

displays a complex surface, characterized by the presence of folds, raptures and impurities. The central region displays the highest level of homogeneity for the lower presence of surface contamination, raptures ad folds. On the outer edges instead, the residues of the wax layer from the transfer process are still visible as brown particles. On the left edge a pronounced surface folding is clearly visible, probably occurred during the wax removal with the toluene. The surface raptures were used to both determine the optical constants and the thickness of the graphene monolayer, because they offer a clear and defined edge where there is a sharp boundary between the graphene layer and the substrate layer. The two red circled areas on the map are the regions of interest where all the measurements were carried out, respectively being (a) the upper right region and (b) the lower left region, respectively. The Ellipsometric measurement was set to be performed with a single angle of incidence at 50 and with a wavelength an interval ranging from 390 to 1000 nm and a sampling interval of 151 steps, out of which the 632,8 nm of the SPR laser wavelength was selected.

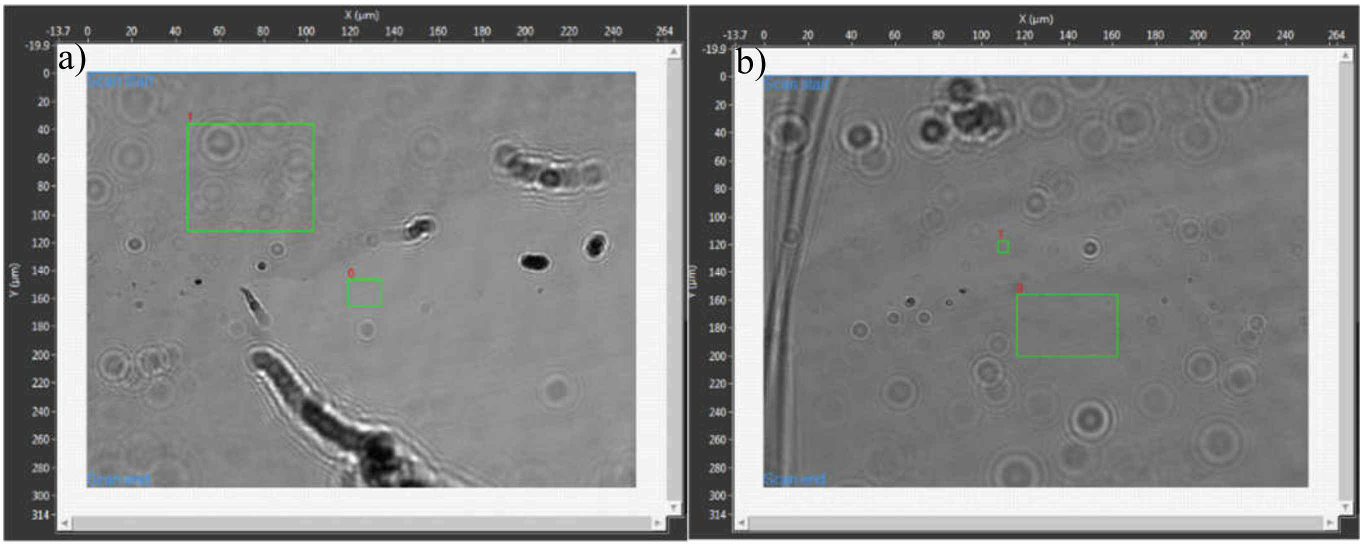

Figure 35. Ellipsometric analysis performed on two different areas of graphene surface. a) Lower left region of the sample, the 0 region of interest (ROI) is gold, whilst the ROI 1 is monolayer graphene. b) Upper right region where the 1 ROI is gold and the 0 ROI is monolayer graphene.

The thickness of the graphene monolayer was measured by using the atomic force microscope (AFM) Veeco Dimension 3100. For this measurement, the same regions of interest were chosen by using the map to position the microscope probe on the same (a) and (b) regions. In the **Figures 34 and 35,** the pictures acquired with the atomic force microscope are compared with optical microscope images acquired at 100x magnification on the same spot. In the same two pictures the height profiles of the graphene layer were measured by using the free software Gwyiddion.

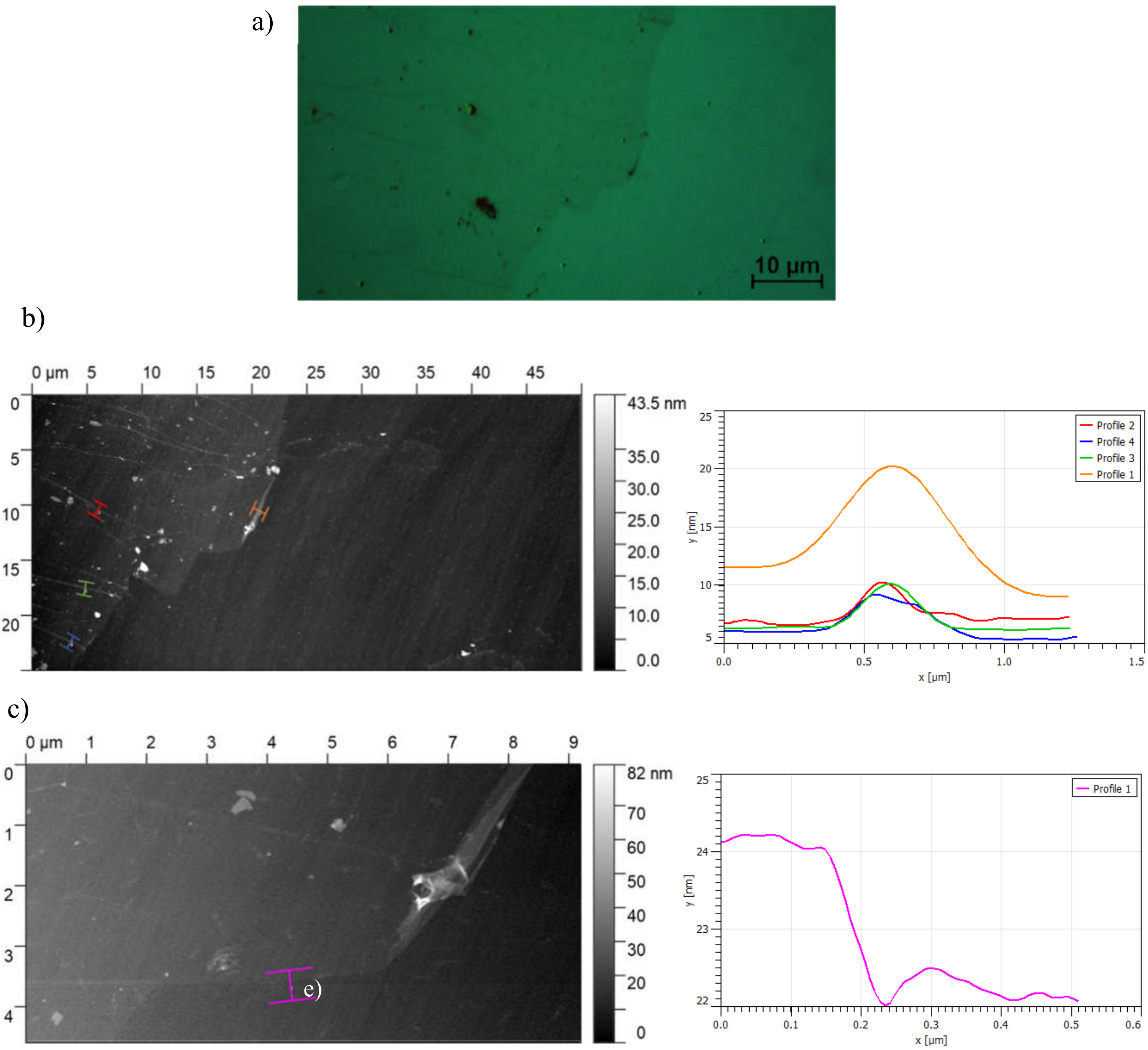

Figure 36. Surface analysis of the lower left region of the graphene layer performed with AFM and optical microscope. a) Optical microscope image at 100x magnification. On the same spot of the optical microscope image two AFM measurements were performed. a) Low magnification AFM image with on the right the height profiles curves of the graphene folds, color matched with the measurement spots. b) High magnification AFM image with on the right the height profile taken on the edge of the graphene layer.

The height profile was measured on both the surface folds and the edges of the graphene and they display and average height of the graphene layer of approximately 2 nm, while the height of the folds displays a much wider distribution with heights ranging between 3 nm for the smallest folds and 9 nm for the biggest one. The value obtained for the graphene thickness is in agreement with previously described findings, where the thickness of the monolayer

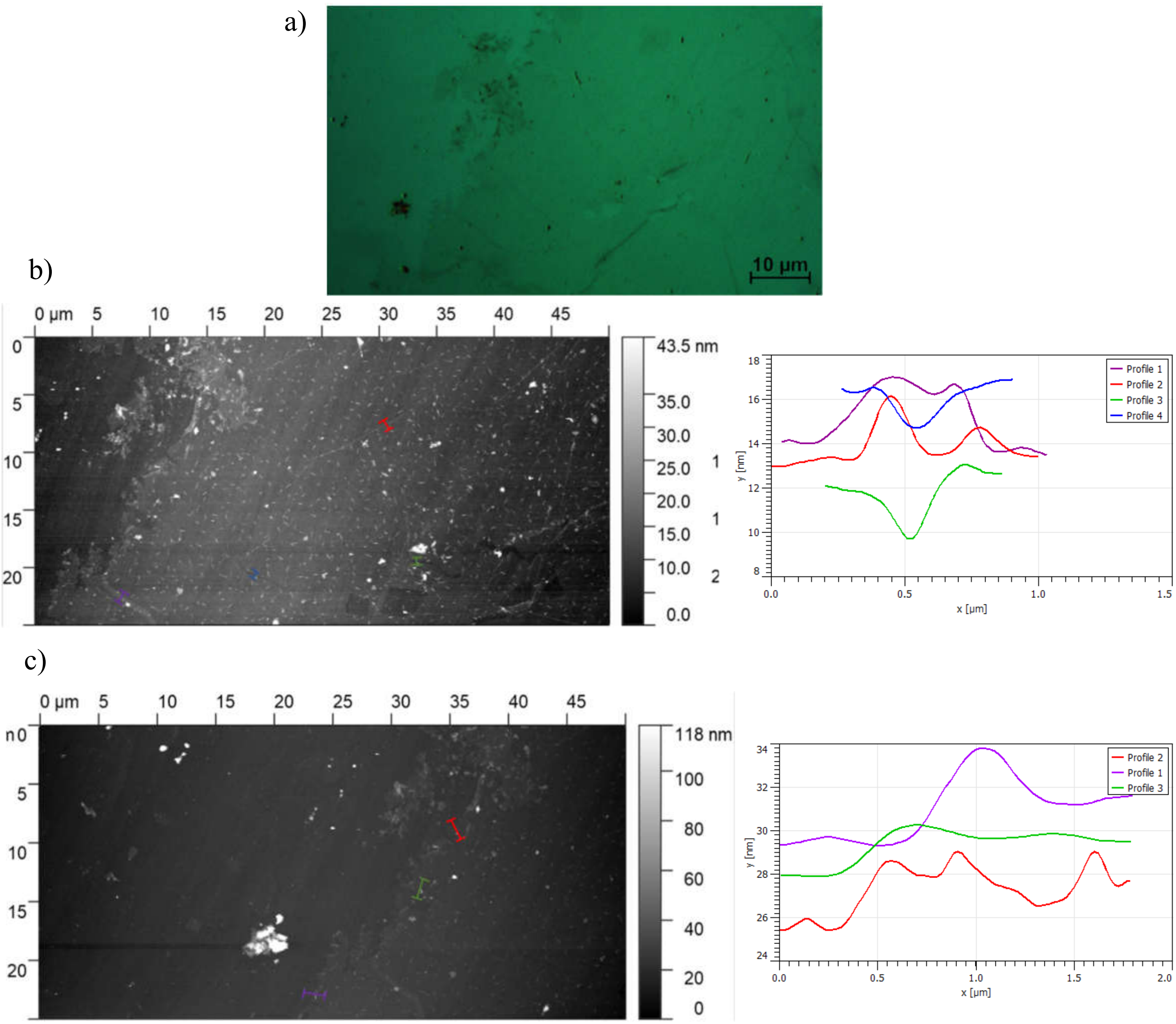

Figure 37. Surface analysis of the upper right region of the graphene layer performed with AFM and optical microscope. a) Optical microscope image at 100x magnification. On the same spot of the optical microscope image two AFM measurements were performed. a) Low magnification AFM image with on the right the height profiles curves of the graphene folds, color matched with the measurement spots. b) High magnification AFM image with on the right the height profiles taken on different edges of the graphene layer.

graphene is 1,51 ± 0,16 nm.[27] The measured thickness of the graphene layer was implemented in the calculation of the graphene's optical constant with the ellipsometer modelling software DataStudio. The obtained refractive index dispersion is in accordance with the previous measurements done by Weber et al., displaying n and k values of 2.7302 and 1.3555 at the SPR laser wavelength of 632.8 nm, respectively.[28]

3.1.3 Gold substrate angle scan

A first angle scan was performed on the SPR substrate before and after the graphene deposition to acquire the reference sensorgrams for the later biofunctionalization. Both the resonance dip angle and the peak shape were affected by the presence of the graphene, giving the confirmation of the successful transfer of the graphene functional layer on top of the gold layer. The shift of minimum angle indicates the change in the real part of dielectric constant introduced by the graphene, while the width and the minimum of the intensity peak are related to the graphene's imaginary part of the dielectric constant, which in this case is typical of a material that absorbs light at the laser wavelength of 632,8 nm. When compared to the simulations, the obtained sensogram is not displaying a resonance dip that reaches the zero reflectivity. This can be related to the fact that the polyimide layer was not completely flat in the area reached by the laser beam, causing the polarized wave not being completely perpendicular to the gold substrate. The unevenness of the polyimide film is determined by the underneath channel of the fluidic cell, that is removing the mechanical support needed to keep the polymer evenly adherent against the glass prism. Another cause for the shallower resonance dip can arise from the increased surface roughness of the sputtered gold layer, that might be due to the lower thermal conductivity of the polyimide layer. As it can be seen from the Scanning Electron Microscopy (SEM), the gold layer deposited on top of the polyimide displays a rough surface.

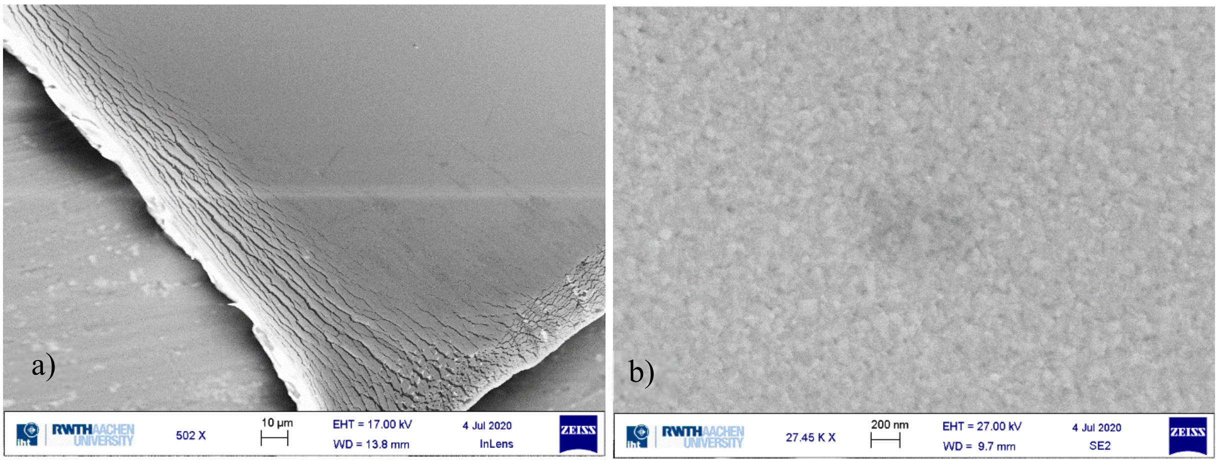

Figure 38. Scanning electron microscope images of the gold sputtered polyimide chip surface, where a) is a lower magnification overview of the chip's surface while b) is a high magnification image, that clearly displays the granular and discontinuous structure of the deposited gold layer.

The discontinuous surface created by the increased number of gold crystal grains induces a damping effect on the surface plasmons, that decreases their propagation length on the metal's surface, resulting in a shallower plasmonic resonance dip.[29]

When performed with water, the angle scan measurement resulted in a sensogram characterized by a resonance angle at a much larger angle of 59° given by the presence water as the surrounding media, which has a much higher refractive index (n = 1,3334). Another noticeable characteristic is a different total internal reflection peak, that now appears shallower compared with the measurement in air. This is due to the different refractive index of the two surrounding infinite media, that this time are the LASF9 glass and water.

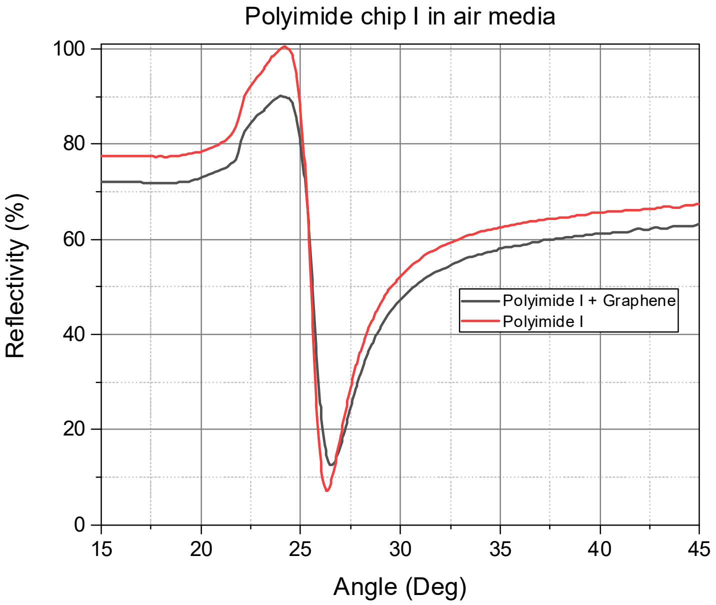

Figure 39. Angular scan of the polyimide flexible chip 1 before and after the graphene deposition

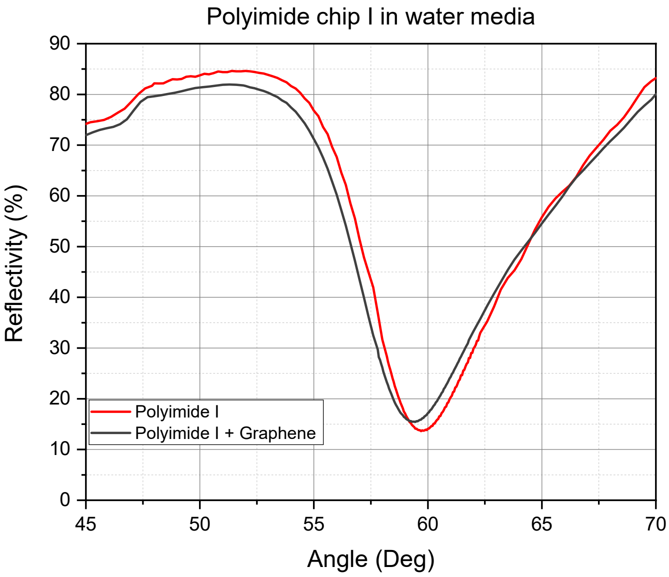

Figure 40. Angular scan in water media of the flexible polyimide chip 1 before and after the graphene transfer

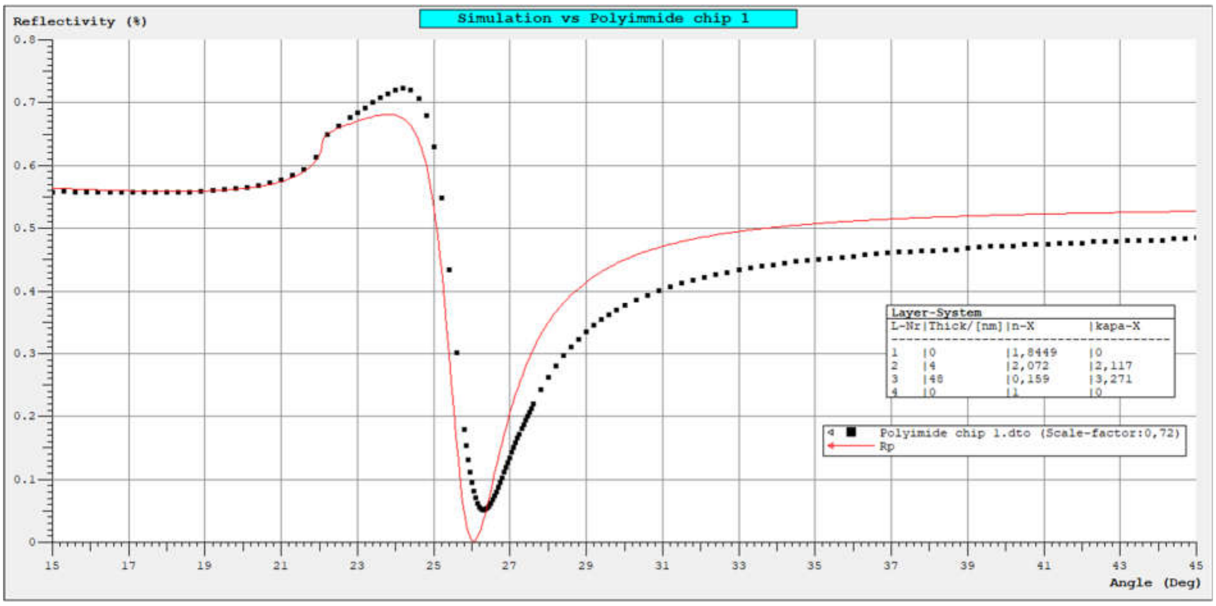

Figure 41. Comparison between the measured sensogram with the simulation made with the software WinSpall 3.02

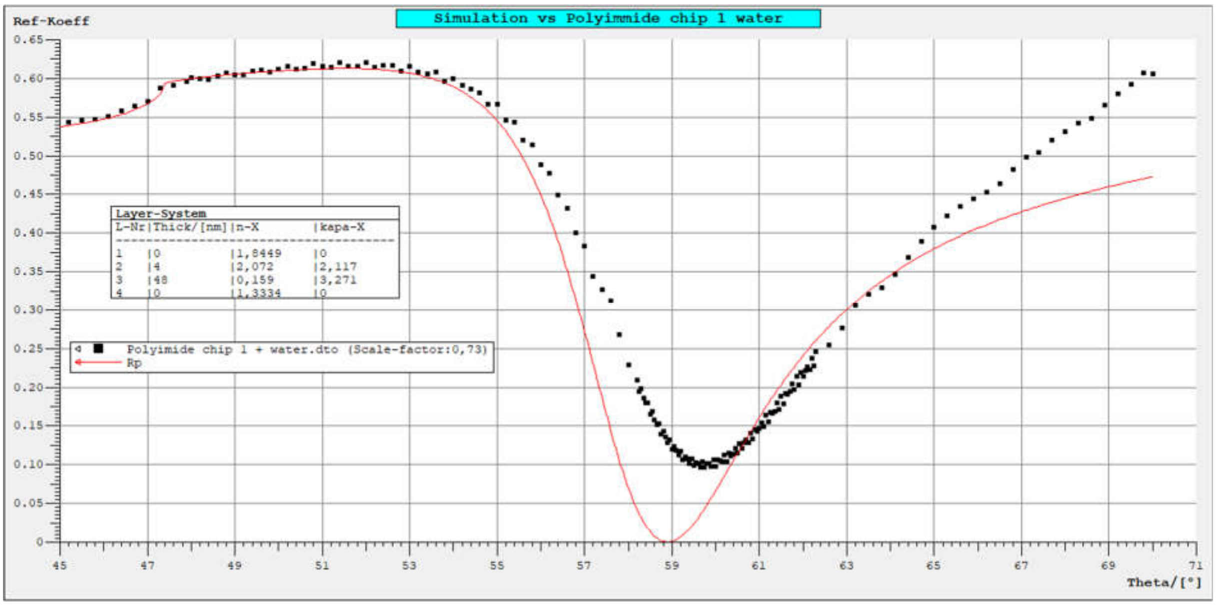

Figure 42. Comparison between the measured sensogram with the simulation made with the software WinSpall 3.02 in water media

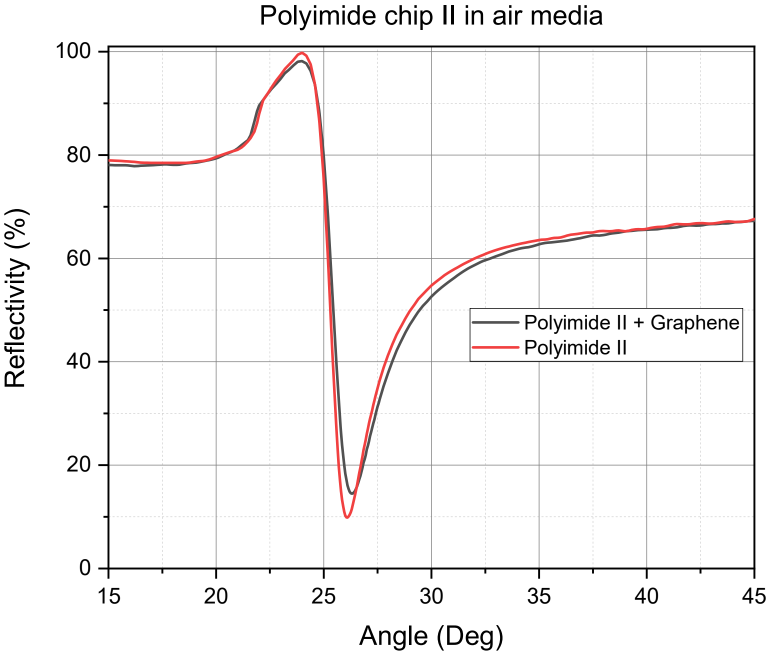

Figure 43. Angular scan of the polyimide flexible chip 2 before and after the graphene deposition

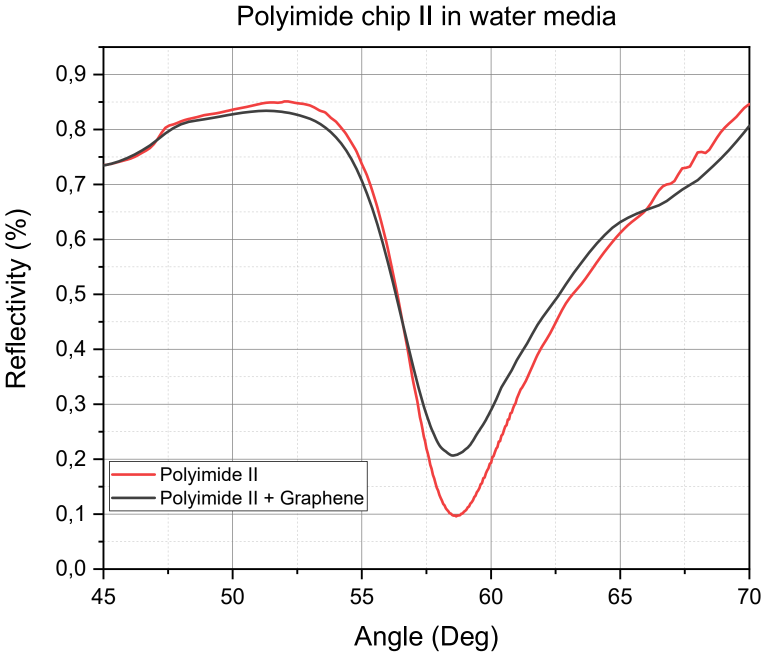

Figure 44. Angular scan in water media of the flexible polyimide chip 2 before and after the graphene transfer

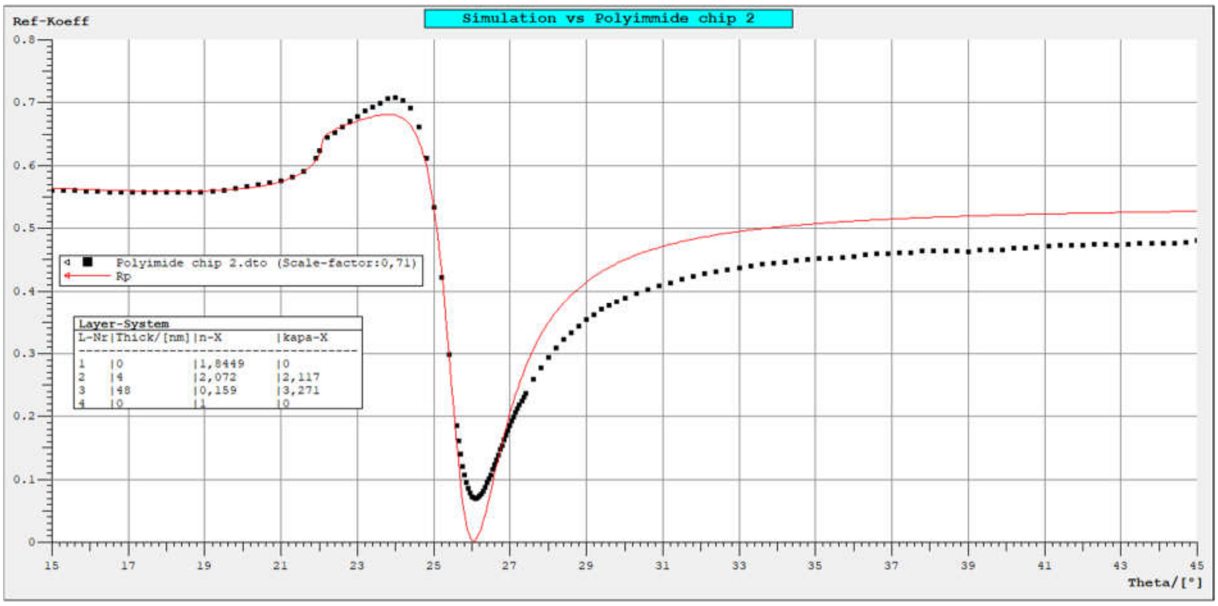

Figure 45. Comparison between the measured sensogram with the simulation made with the software WinSpall 3.02

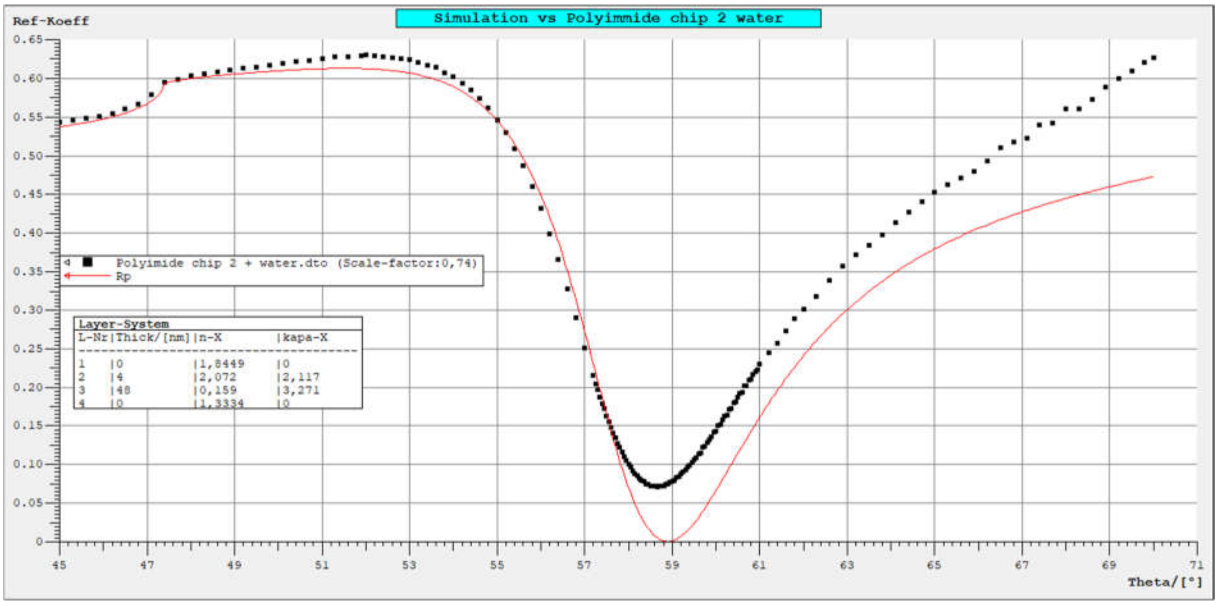

Figure 46. Comparison between the measured sensogram with the simulation made with the software WinSpall 3.02 in water media

3.1.4 Surface activation

The substrate activation was carried out directly inside the fluidic cell by injecting the activating solution inside the fluidic cell with the aid of a syringe pump. The required activating solution was prepared by mixing two aqueous solutions of respectively 50µL of 20 mM 1-ethyl-3-(3-dimethylaminopropyl)-carbodiimide (EDC) and 500 µL 50 mM N-hydroxysuccinimide (NHS) that were mixed together with 450 µL of PBS buffer solution at pH 6 right before starting the surface activation procedure. The flow rate of the pump was set to different values according to the chosen activation time.

3.1.5 HER2-ECD functionalization

The lyophilized HER2-ECD biomolecules were reconstituted in a stock solution by diluting it in 800 µL of sterile water, forming a stock solution with a concentration of 250 µg/mL.

All the HER2-ECD solutions employed for the functionalization process were prepared by withdrawing 80 µL of the cancer biomarker form the stock solution and dissolving it 920 µL of acetate buffer at pH 4.3. The flow rate during the functionalization of the HER2-ECD molecule was changed according to the chosen reaction time.

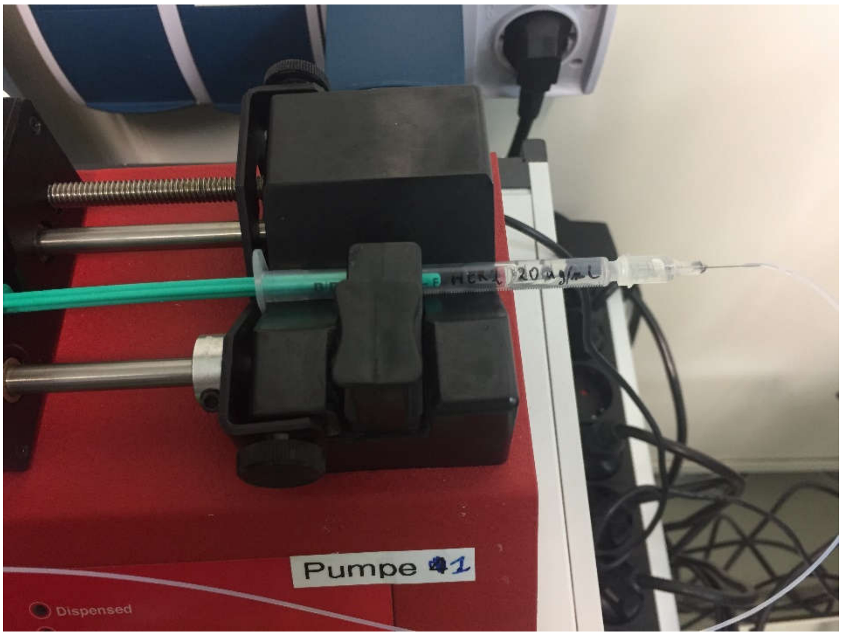

Figure 47. Syringe containing the 20 µg/mL HER2-ECD solution, placed on top of the fluidic pump.

3.1.6 Nanobodies elution

The binding affinities of two nanobodies M-061 and M-062 were measured by injecting them inside the fluidic cell at increasing concentrations. The two nanobodies were stored in two stock solutions at -20°C: M-061 700 µL 84.7 µM and M-062 1 mL 77.8 µM. To prepare the serial dilutions for the kinetic measurements, two initial simple dilutions of each nanobody were prepared by taking an aliquot of 11.8 µL of the M-061 nanobody and 12.8 µL of the M-062 and diluting them in 988.2 and 987.2 µL of PBST buffer at pH 7.4, respectively. The successive serial dilutions were made by taking 100 µL from the first dilutions of the nanobodies and diluting them with 900 µL of PBST, obtaining the following serial concentrations: 1 pM, 10 pM, 100 pM, 1 nM, 10 nM, 100 nM, 1 µM.

Figure 48. Tube rack holding the tubes organized with descending concentration from 1µM to 1pM

3.1.7 Kinetic measurements

For the kinetic measurements, a total of 4 polyimide chips (polyimide chips 2, 6, 1, and 8) were used. These 4 chips were chosen from a group of 11 chips where the graphene was previously transferred, by selecting the ones where the transfer procedure had the best results.

3.1.7.1 Effect of PBST on the flexible SPR polyimide chip

A kinetic measurement during the PBST elution into the fluidic cell was done over the time of 102 minutes with a flow rate of 5 µL/min, to assess the stability of the reflectivity signal over time. In the smoothed sensorgram of **Figure 50**, the intensity of the of reflectivity is not stable over time, indeed it is oscillating over time, reaching the maximum around the 100 minutes mark, where the signal is eventually stable at 25.5%. A similar behavior was not expected in the presence of the sole PBST solution and might be related to the absorption over time of either the contact matching oil or the injected solution moisture by the polyimide layer. The absorption of either the matching oil or the moisture could have caused the warping of the polyimide layer that resulted in the increase of the reflectivity signal.

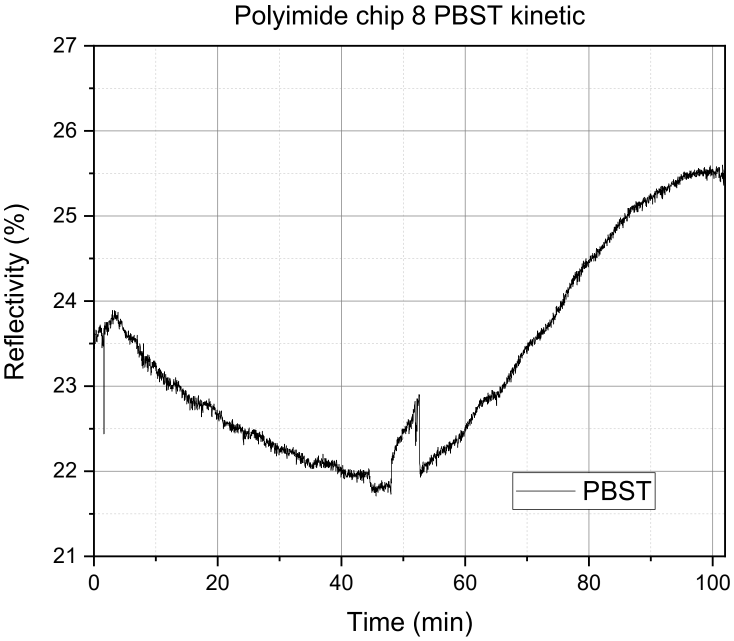

Figure 49. Kinetic sensorgram performed on the polyimide chip 8 during the elution of only PBST solution over the period of 110 minutes at a stable flow rate of 5 µL/min.

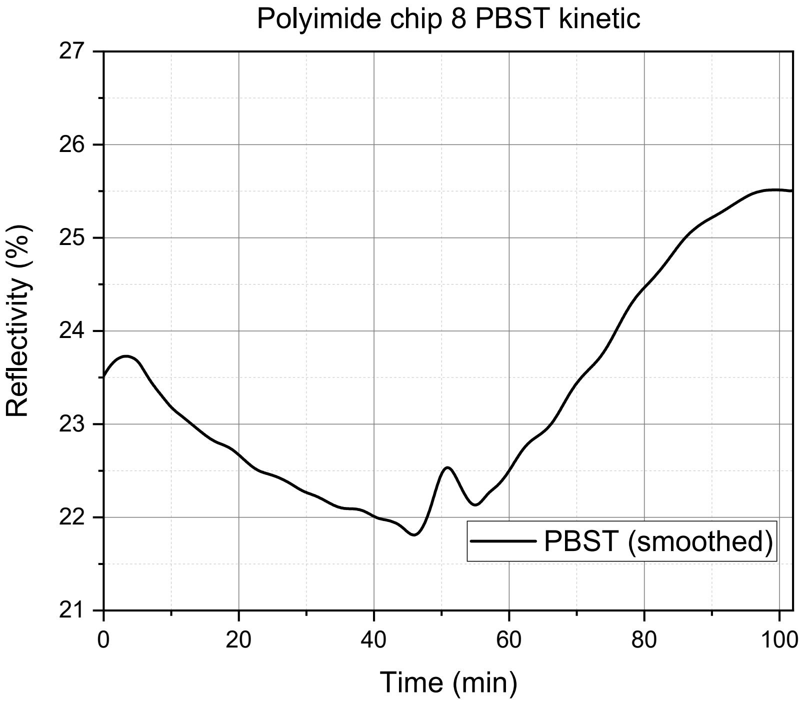

Figure 50. Kinetic sensorgram performed on the polyimide chip 8 during the elution of only PBST solution over the period of 110 minutes at a stable flow rate of 5 μL/min.

3.1.7.2 Monitoring the EDC/NHS surface activation

A kinetic measurement was carried out during the surface activation of the polyimide chip 1, to monitor the signal change induced by the formation of the surface-activated layer on the graphene substrate. The kinetic measurement was performed over a period of 130 minutes, during which the solution was injected with a steady flow rate of 5 µL/min. In **Figure 51** the smoothed kinetic sensorgram displays how the signal was not stable during the reaction time. The intensity of the reflectivity showed a similar behavior to the PBST kinetic measurement, with a constant increase of the signal after the 60-minute mark, reaching the 26.5% stable point the end. This constant increase of the reflectivity might be related to a buildup on the graphene's surface of the EDC/NHS byproduct such as urea or the distortion of the polyimide layer induced over time from the absorption of the moisture from the solution. The increment of one unit in respect to the PBST sensorgram might be related to the formation of the active surface on the graphene substrate, that induced a shift of the resonance peak towards a higher angle.

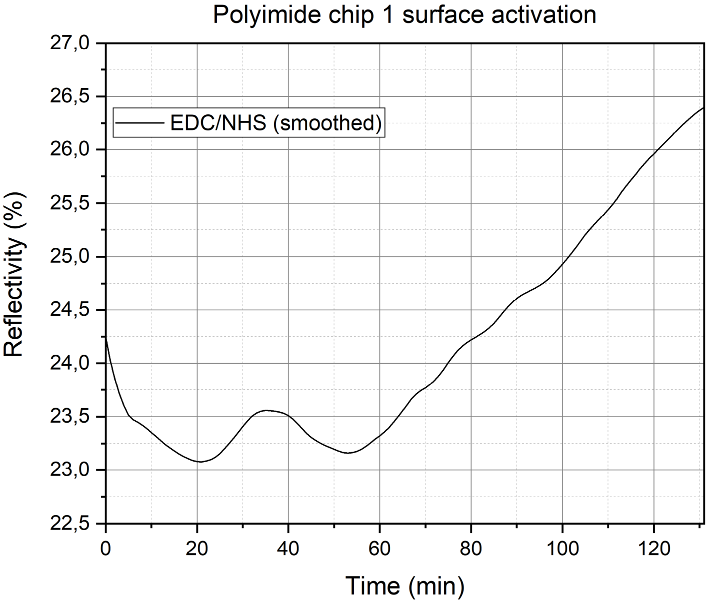

Figure 51. Smoothed kinetic measurement performed on the polyimide chip 1 during the graphene surface activation with the EDC/NHS protocol.

3.1.7.3 Monitoring of the HER2-ECD binding on the graphene surface

To monitor the HER2-ECD functionalization on the polyimide chip 1, the injection of the caner biomarker was performed over the period of 3 hours with a flow rate of 5 μL/min. During this time, a kinetic measurement was carried out to keep track of the reflectivity signal over time. In **Figure 52** it is visible how the signal curve had a similar behavior to the curve in the EDC/NHS and PBST kinetic measurements. This time the reflectivity signal reached a maximum value of around 28%, which is considerably higher than the past two measures. The noticeable increase of the reflectivity might be related to the preconcentration effect of the HER2-ECD biomolecules on the graphene's surface, generated by the electrostatic interaction between the negatively charged hydroxyl groups on the graphene's surface and the positively charged HER2-ECD biomolecule in solution.

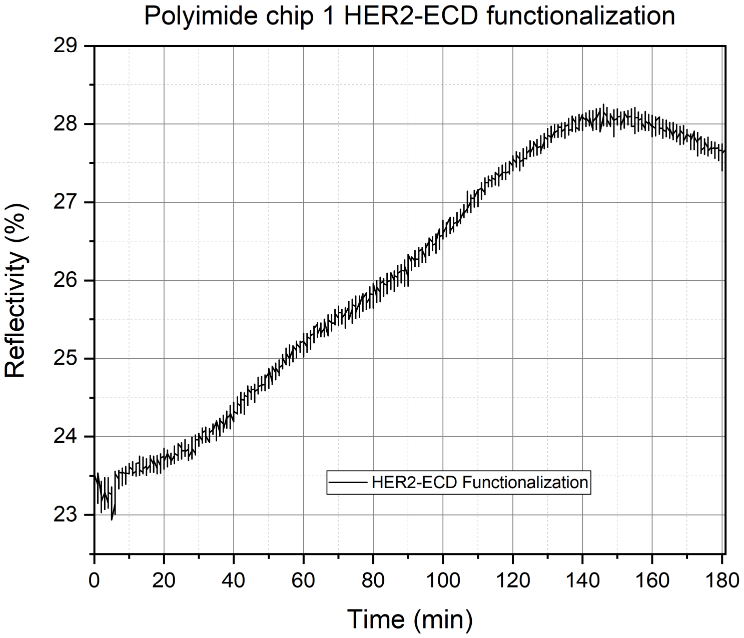

Figure 52. Kinetic measurement performed on the polyimide chip 1 during the functionalization of the HER2-ECD biomolecule on the activated graphene's surface.

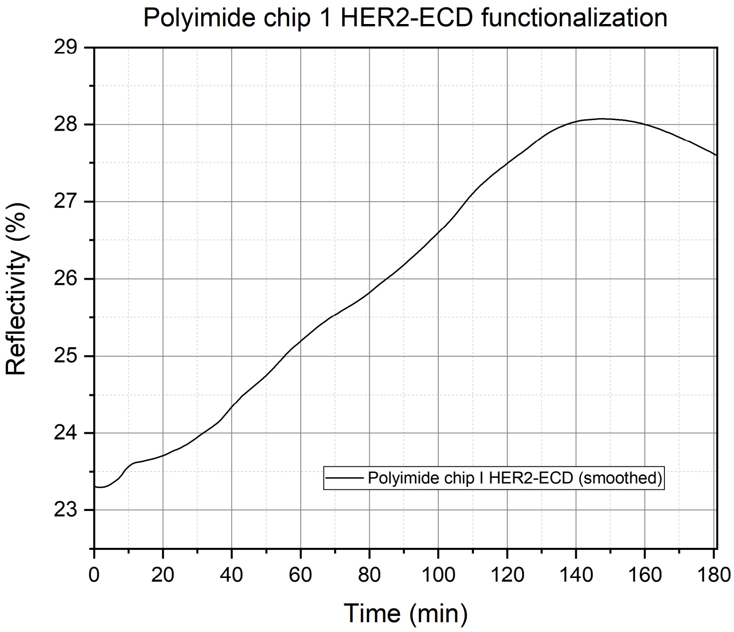

Figure 53. Smoothed Kinetic measurement performed on the polyimide chip 1 during the functionalization of the HER2-ECD biomolecule on the activated graphene's surface.

3.1.7.4 Nanobodies Kinetic measurements

All the nanobodies elutions were carried out in 10 minutes intervals, during which the fluidic pump was kept at a flow rate of 10 µL/min for the first 5 minutes and stopped for the remaining 5.

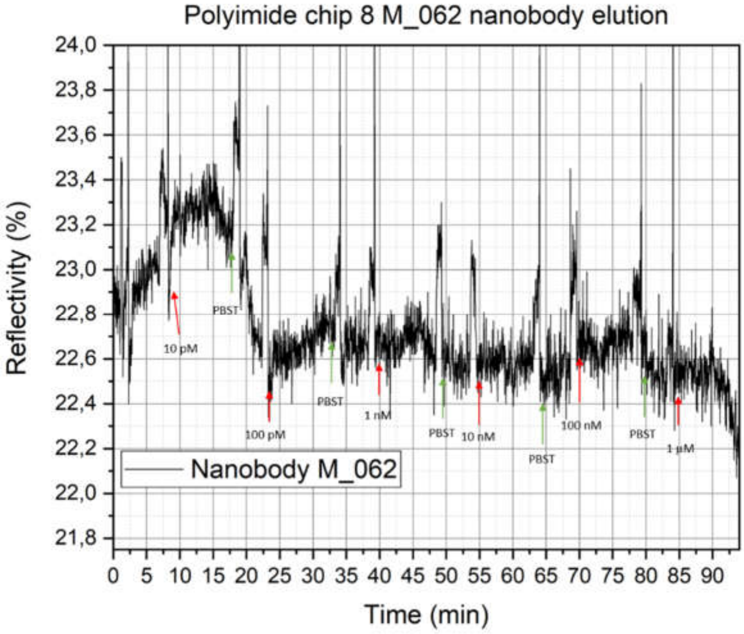

Figure 55. Kinetic sensorgram of the M-61 nanobody elution with the polyimide chip 8.

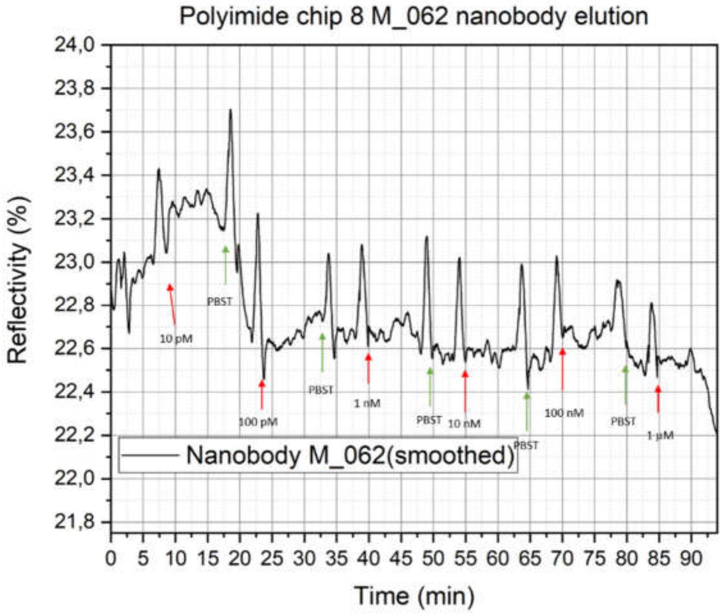

Figure 54. Smoothed Kinetic sensorgram of the M-61 nanobody elution with the polyimide chip 8.

The first kinetic measurement was performed with the nanobody M-61 on the polyimide chip 8. PBST at pH 7.4 was used as regenerating solution, by injecting with 2 minutes intervals between the nanobodies injections. The first unsmoothed sensorgram in **Figure 54** displays a lot of background noise that makes it difficult to assess the binding curves at different concentrations. In the smoothed sensorgram of **Figure 55**, it is visible how after an initial steep increment, the reflectivity signal kept decreasing, showing its lowest value during the latest injection with the highest concentration. This might be due to an over saturation of the binding sites that were not successfully regenerated with the use of the sole PBST solution. Another reason for the decreasing signal might be related to the distortion of the polyimide layer over time, causing an irreversible shift of the plasmonic resonance angle towards a lower angle.

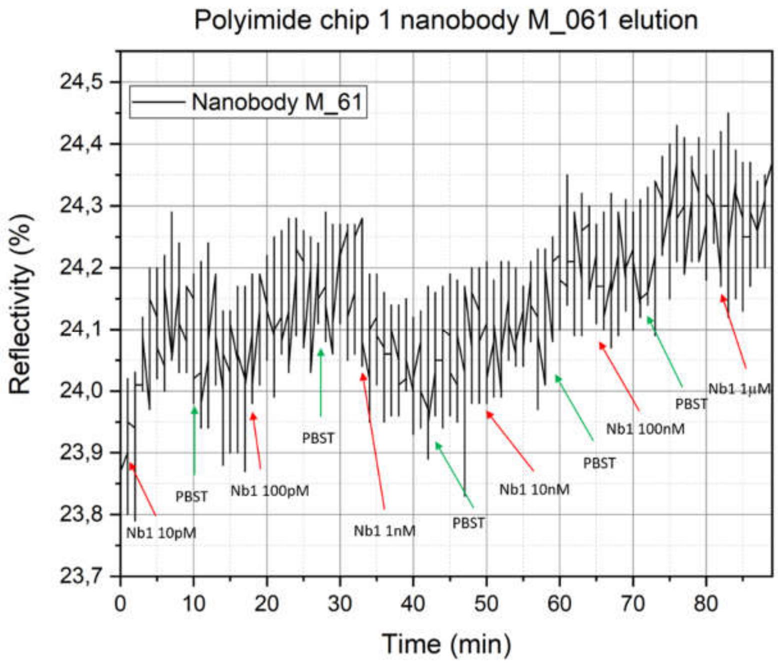

Figure 56. Kinetic measurement of the nanobody M-61 elution at 6 different concentrations.

The second kinetic measurement was performed with the nanobody M-61 on the polyimide chip 1. Also, this time PBST at pH 7.4 was used as regenerating solution, by injecting with 2 minutes intervals between the nanobodies injections. From the smoothed kinetic measurement in **Figure 57** it can be seen how the signal is not stable. The decrease in the central part of the sensorgram might be related to the oversaturation of the binding sites of the HER2-ECD biomarker or to the warping of the polyimide chip over time.

To improve the kinetic measurements performed on the polyimide chip 2, a 10 mM solution of NaOH was used as the main regenerating solution, and the PDMS gasket was replaced with a biocompatible double adhesive tape. The double adhesive tape was used to ensure a tight seal between the polyimide chip and the fluidic cell, without applying excessive downward pressure with the glass prism, decreasing this way the mechanical stress on the polyimide layer. With this new chip configuration and regenerating solution, the sensorgram was displaying a stabler signal (**Figure 59**). Even if a gradual decrease was still present towards the end, the overall measurement displayed a noticeable improvement. The decrease of the signal might be related

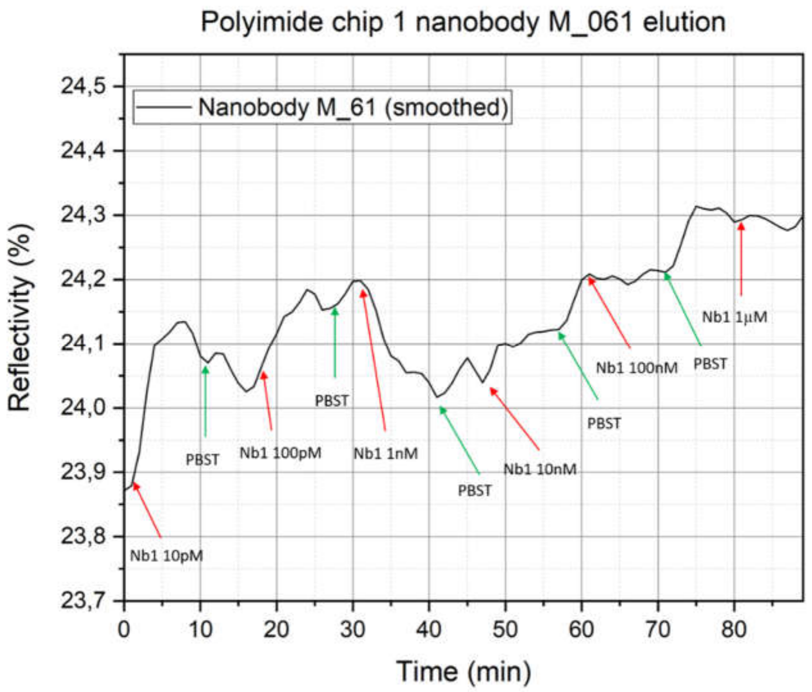

Figure 57. Smoothed kinetic measurement of the nanobody M-61 elution at 6 different concentrations.

to the high concentration of the 10 mM NaOH solution that could have denatured the HER2-ECD biomolecule, decreasing the number of the available binding sites.

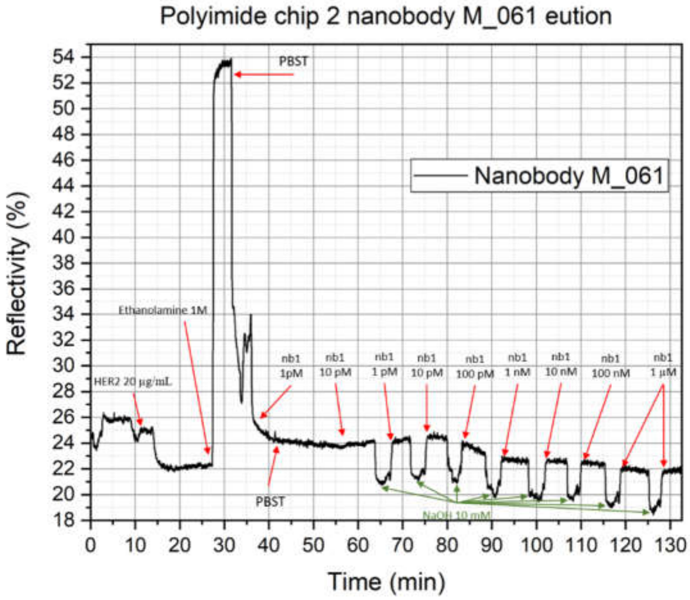

Figure 58. Kinetic measurement performed on the polyimide chip 2 during the elution of the M_61 nanobody at 7 different concentrations. The first two elution were carried out with PBST as regenerating solution, but later it was replaced with NaOH 10 mM.

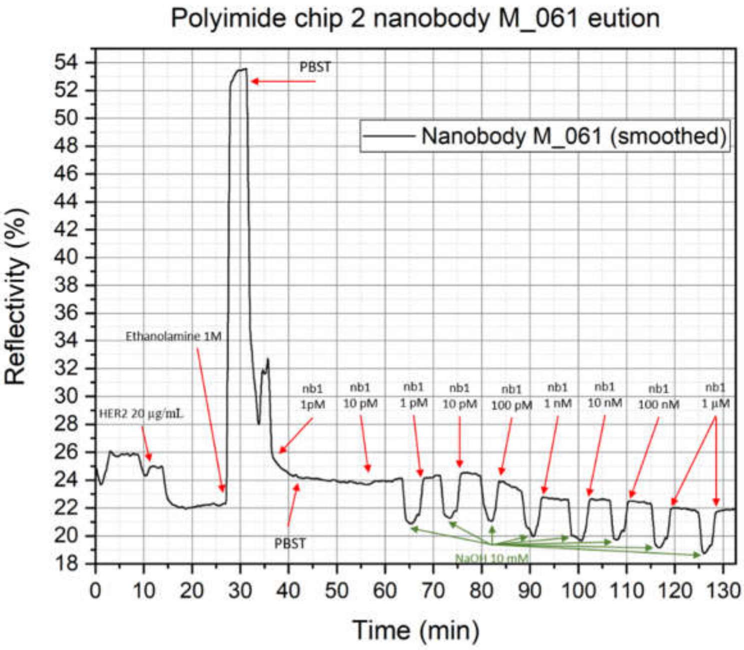

Figure 59. Smoothed kinetic measurement performed on the polyimide chip 2 during the elution of the M_61 nanobody at 7 different concentrations. The first two elution were carried out with PBST as regenerating solution, but later it was replaced with NaOH 10 mM.

The last kinetic measurement was performed on the polyimide chip 6 with the nanobody M-061. The employed regenerating solution was prepared with NaOH with a lower 5 mM concentration. From the smoothed sensorgram in **Figure 61** the signal displays an increasing intensity with higher concentrations of the nanobody injections and a better stability. This might be related to the fact that this the lower concentration of the 5 mM NaOH had a positive effect

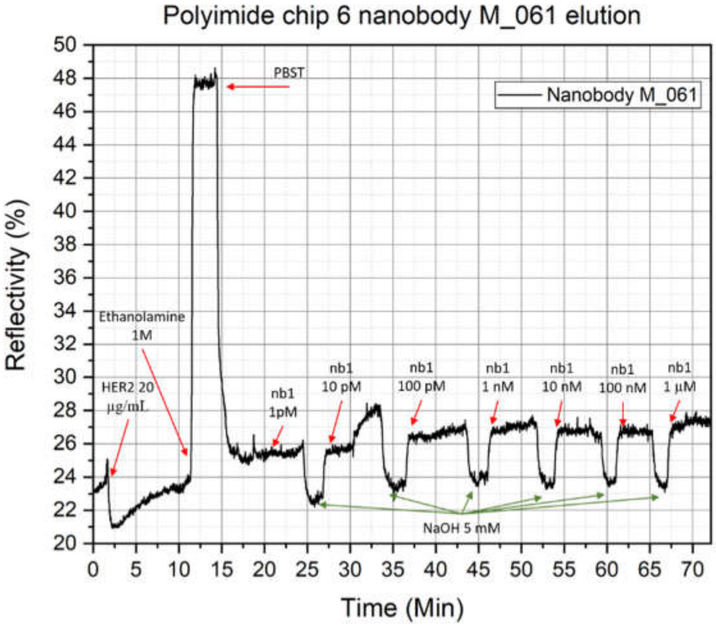

Figure 60. Kinetic measurement performed on the polyimide chip during the elution of the M_61 nanobody at 7 different concentrations.

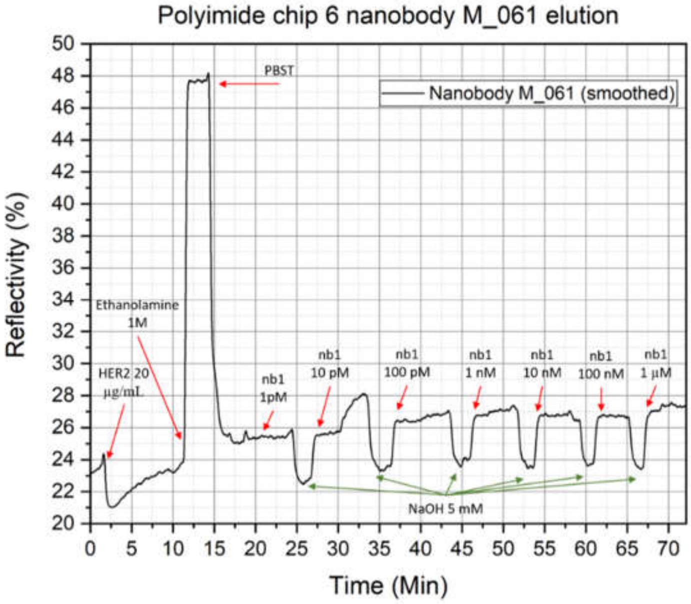

Figure 61. Smoothed kinetic measurement performed on the polyimide chip 6 during the elution of the M_61 nanobody at 7 different concentrations.

on the HER2-ECD biomarker, successfully regenerating the binding sites without affecting their availability to the nanobody receptor molecules.

3.1.7.5 SPR angle scans comparison with the simulations

Several SPR angle scans were acquired on each polyimide chip during the kinetic measurements, to assess and compare the plasmonic resonance dip at the beginning of the measurement with only the PBST solution and at the end after the functionalization of the HER2-ECD molecules and nanobodies elution. The angle scans performed with the PBST solution were also compared with the simulated angle scans generated with the WinSPall 3.01 software. An Iterative fitting of the simulated angle scan over the experimental was carried out for each polyimide chip, allowing the software to fit the optical constant of the graphene layer.

The SPR scans performed before and after the kinetic measurements on the polyimide chip 8 (**Figure 62**) displays an increase of the signal noise with time, visible especially in the sensorgram after the PBST kinetic measurement and HER2-ECD functionalization. In the smoothed sensorgram of **Figure 63**, the resonance dip angles are more visible after the denoising. With the smoothed resonance dips, a shift towards a higher angle after the HER2-ECD functionalization is visible, confirming the successful functionalization of the HER2-ECD biomolecules on the activated graphene’s surface.

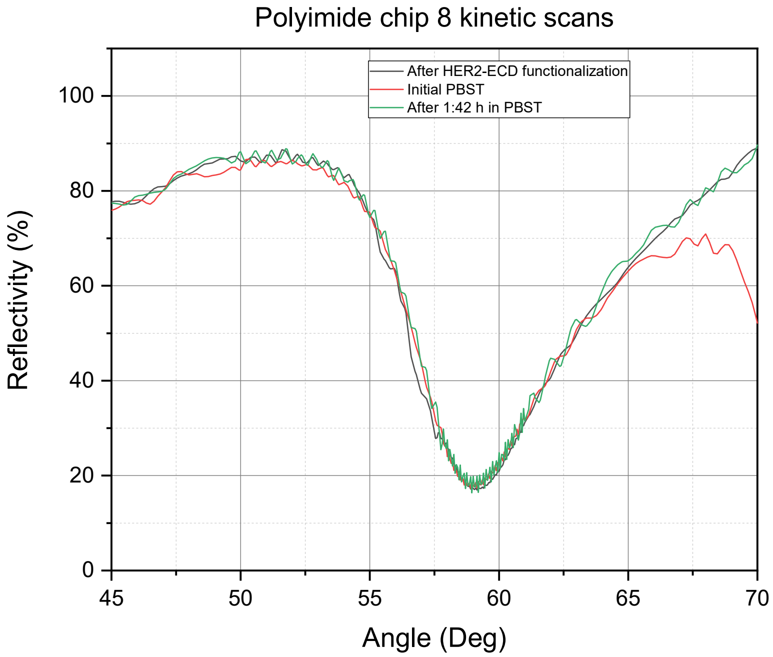

Figure 60. Polyimide chip 8 SPR angle scans measured in PBBST before the surface activation, after the EDC/NHS surface activation and after the HER2-ECD functionalization and M-62 nanobody elution.

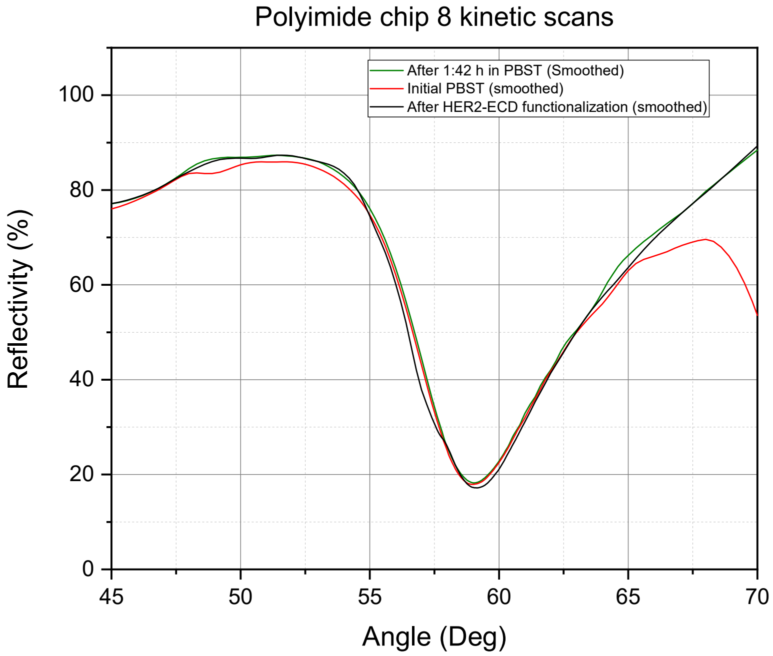

Figure 61. Polyimide chip 8 smoothed SPR angle scans measured in PBBST before the surface activation, after the EDC/NHS surface activation and after the HER2-ECD functionalization and M-62 nanobody elution.

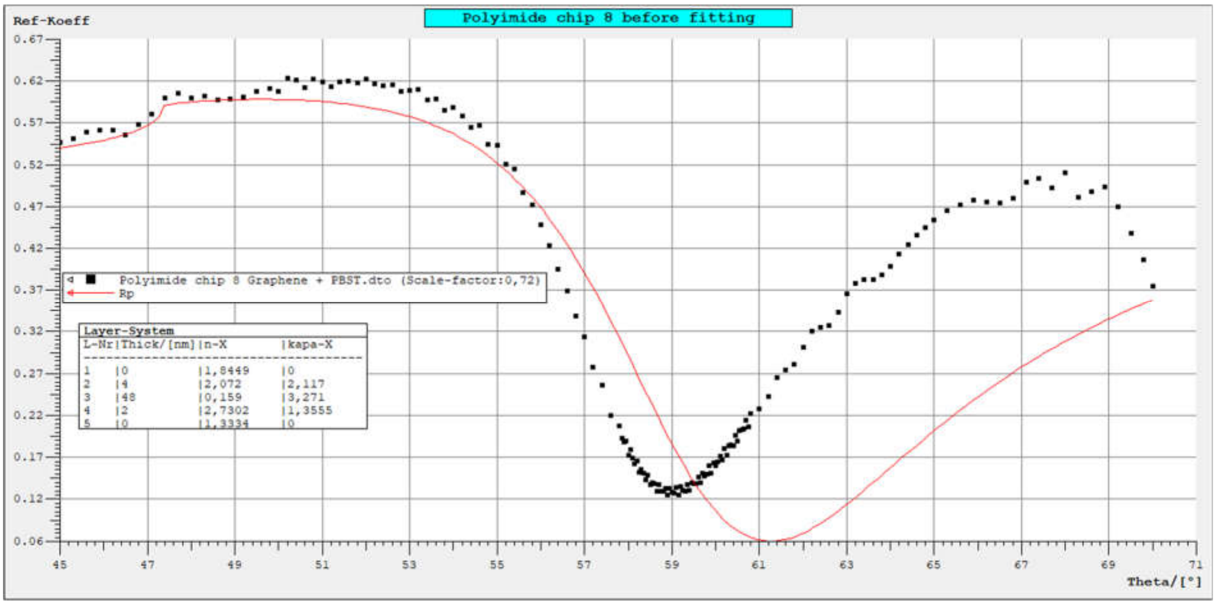

Layer-System

L-Nr	Thick/[nm]	n-X	kapa-X
1	0	1,8449	0
2	4	2,072	2,117
3	48	0,159	3,271
4	2	2,7302	1,3555
5	0	1,3334	0

Figure 62.Comparison between the angle scan of the polyimide chip 8 in PBST media and the simulated angle scan with the software WinSpall 3.01.

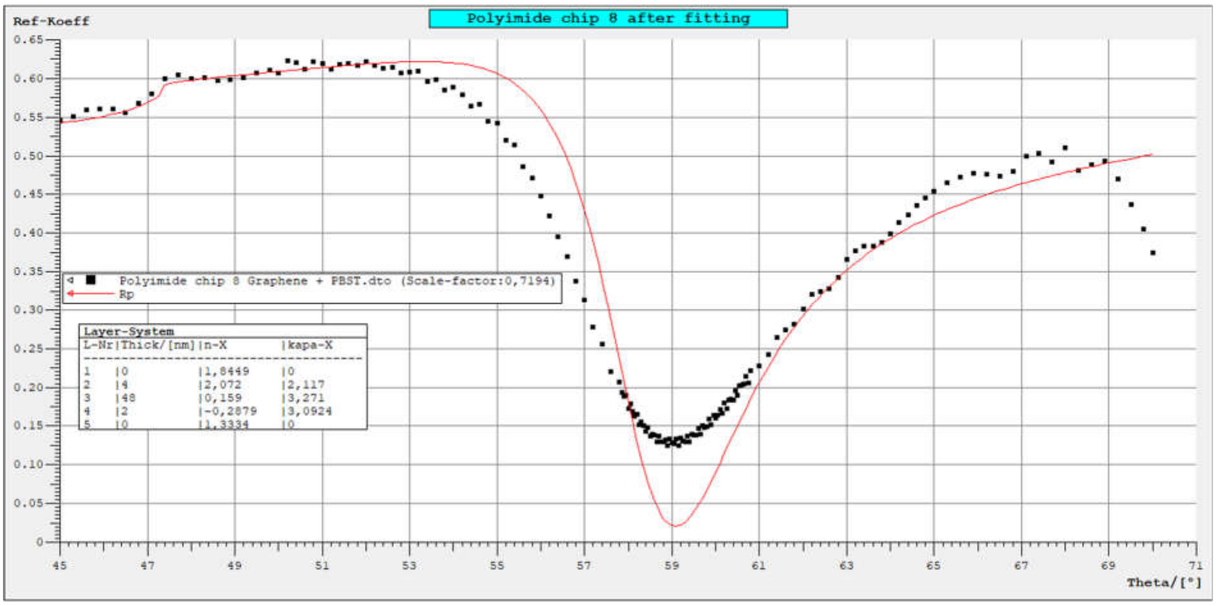

Layer-System

L-Nr	Thick/[nm]	n-X	kapa-X
1	0	1,8449	0
2	4	2,072	2,117
3	48	0,159	3,271
4	2	-0,2879	3,0924
5	0	1,3334	0

Figure 63. Fitting of the simulated sensogram with the measured one by changing only the optical constants of the graphene layer. The fitting was done with an iterative simulation in WinsPall 3.01.

In **Figure 64** a simulated SPR angle scan in PBST was compared with the measured one in PBST. The difference between the simulated and measured resonance dips is around 2° and it is a confirmation that there was a problem with the polyimide layer surface. The iterative fitting of the simulated SPR sensorgram was done by allowing the software to change only the n and k optical constants of the graphene, because the graphene thickness and all the other substrate physical constants were known from the previous Ellipsometric and AFM measurements. As it can be seen from **Figure 65**, the graphene's refractive index is displaying a negative n value, which does not have any physical meaning, once again confirming that there was a problem with the sensor alignment.

The angle scans performed on polyimide chip 1 all display in **Figure 66** a resonance dip positioned at the same reflectivity and resonance angle. In the smoothed angle sensorgram of **Figure 67** a shift of towards higher angle is visible on the measurements performed after the HER2-ECD functionalization and elution of the nanobody. This is a confirmation of a successful functionalization of the HER2-ECD biomolecule on the graphene surface, that induced the plasmonic resonance conditions to be met at a new higher angle value.

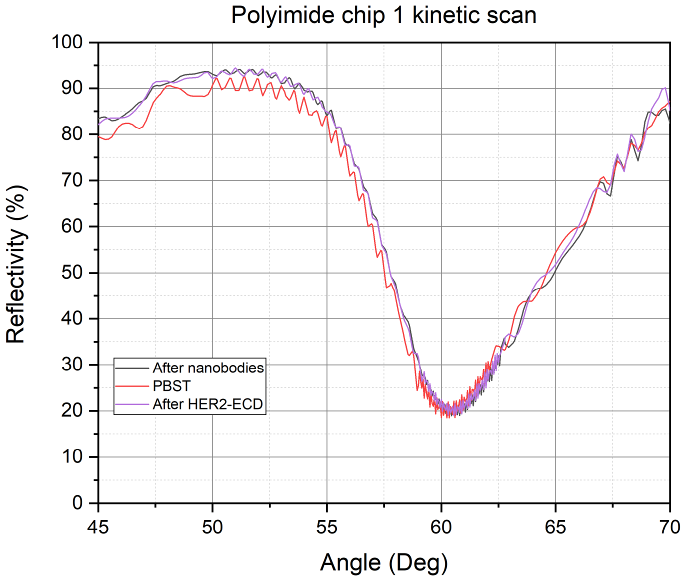

Figure 64. Polyimide chip 1 SPR angle scans measured in PBBST before the surface activation, after the EDC/NHS surface activation and after the HER2-ECD functionalization and nanobody elution.

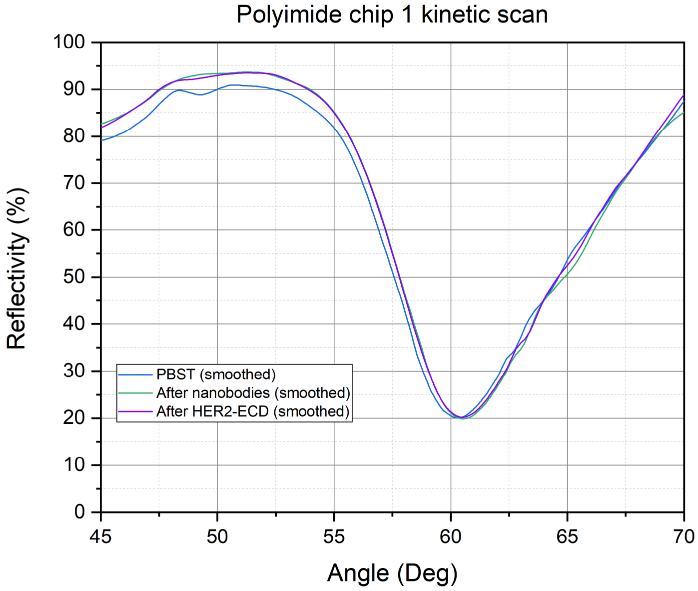

Figure 65. Polyimide chip 1 smoothed SPR angle scans measured in PBBST before the surface activation, after the EDC/NHS surface activation and after the HER2-ECD functionalization and nanobody elution.

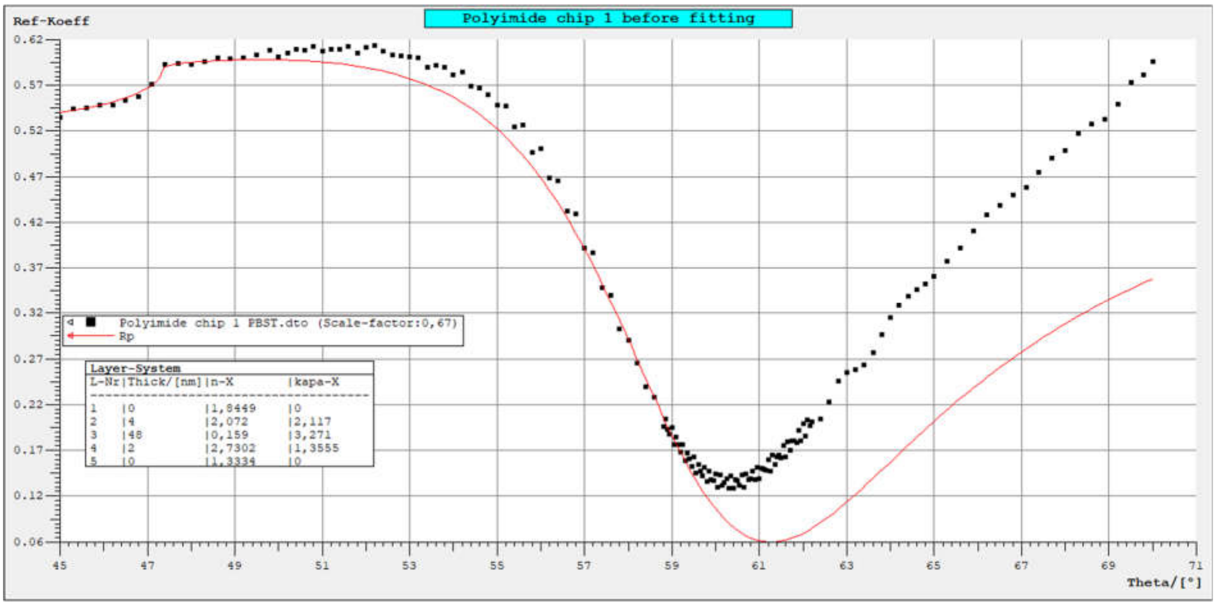

```
■   Polyimide chip 1 PBST.dto (Scale-factor:0,67)
←   Rp

Layer-System
L-Nr|Thick/[nm]|n-X        |kapa-X
-----------------------------------
1   |0         |1,8449     |0
2   |4         |2,072      |2,117
3   |48        |0,159      |3,271
4   |2         |2,7302     |1,3555
5   |0         |1,3334     |0
```

Figure 66. Comparison between the angle scan of the polyimide chip 1 in PBST media and the simulated angle scan with the software WinSpall 3.01.

The comparison between the simulated angles scan and the measured angle scan in PBST in **Figure 68**, were displaying a decreased difference in the resonance peak, but after the fitting the new graphene optical constants visible in **Figure 69** were still too different from the initial ones. This difference between the measured and simulated angle scans might be still related to the warping of the polyimide layer over time.

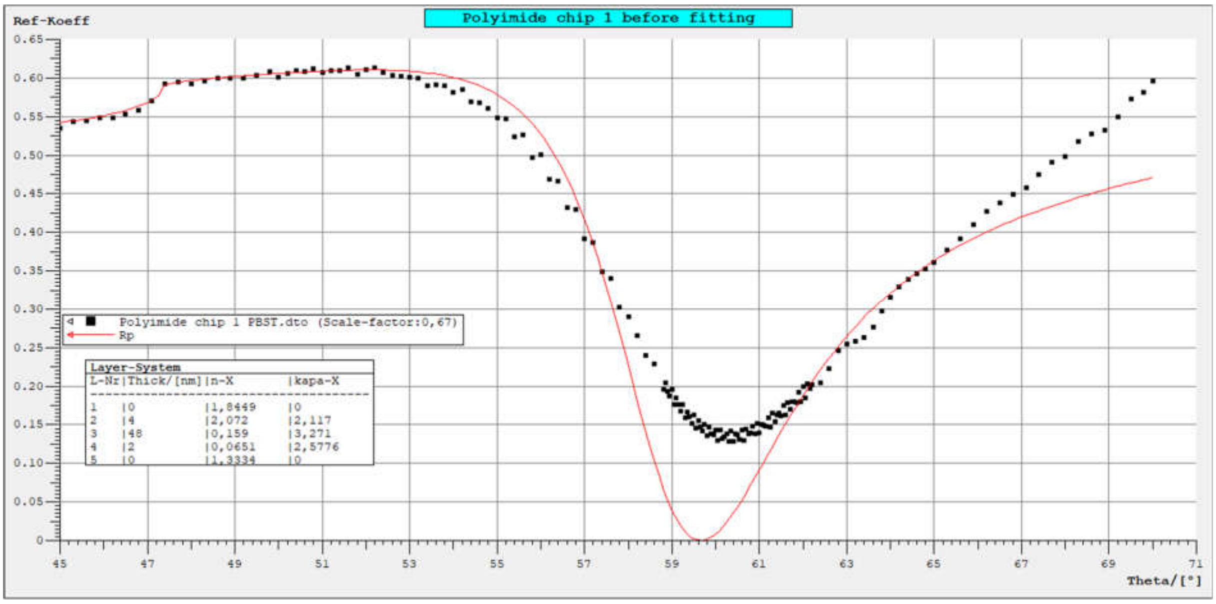

```
Layer-System
L-Nr|Thick/[nm]|n-X          |kapa-X
--------------------------------------
1    |0         |1,8449      |0
2    |4         |2,072       |2,117
3    |48        |0,159       |3,271
4    |2         |0,0651      |2,5776
5    |0         |1,3334      |0
```

Figure 67. Fitting of the simulated sensogram with the measured one by changing only the optical constants of the graphene layer. The fitting was done with an iterative simulation in WinsPall 3.01

In the **Figures 70** and **71**, the SPR angle scans performed on the polyimide chip 2 right before the surface activation with EDC/NHS, after the surface activation and after the functionalization with the HER2-ECD biomarker and elution with the M-61 nanobody are

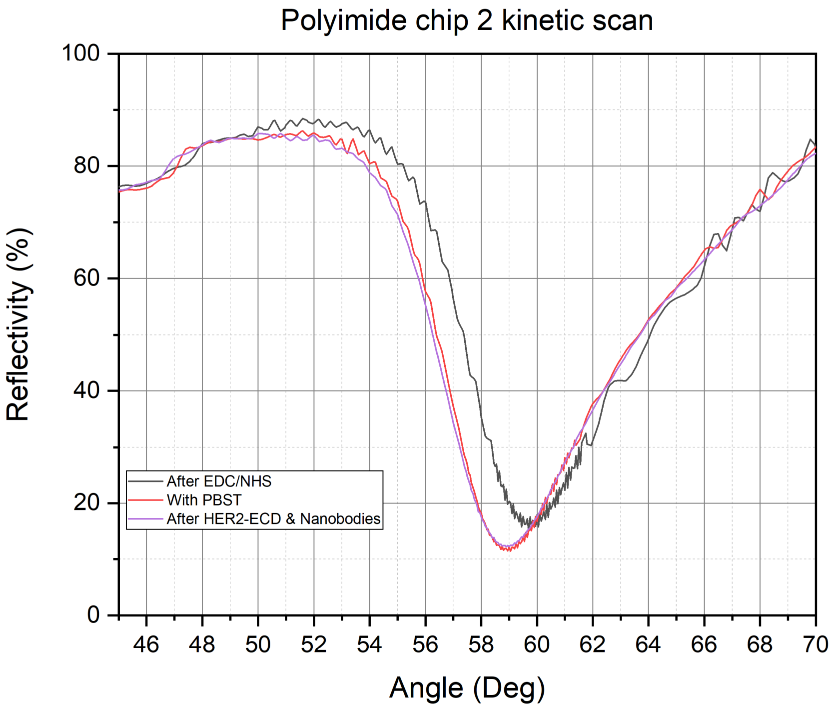

Figure 68. Angle scans performed during the kinetic measurements to assess the resonance angle changes.

visible. The angle scan sensorgram taken after the EDC/NHS surface activation displays a noticeable noise increase and a resonance dip shifted towards the upper right side. The two angle scans taken with only PBST and after the HER2-ECD functionalization display a stabler signal, with the HER2-ECD sensorgram having a resonance dip slightly shifted toward a higher resonance angle as expected after the buildup of the HER2-ECD dielectric adlayer on the graphene's surface.

A simulation of the polyimide chip with graphene in PBST media was compared with the initial SPR angle scan in PBST (**Figure 72)**.

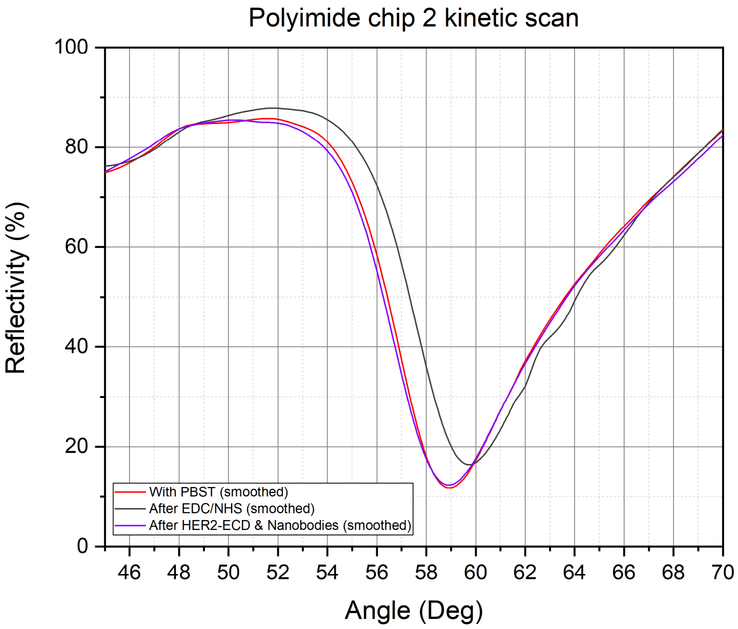

Figure 71. Angle scans performed during the kinetic measurements to assess the resonance angle changes. The signal was smoothed to evidence the angle shifts

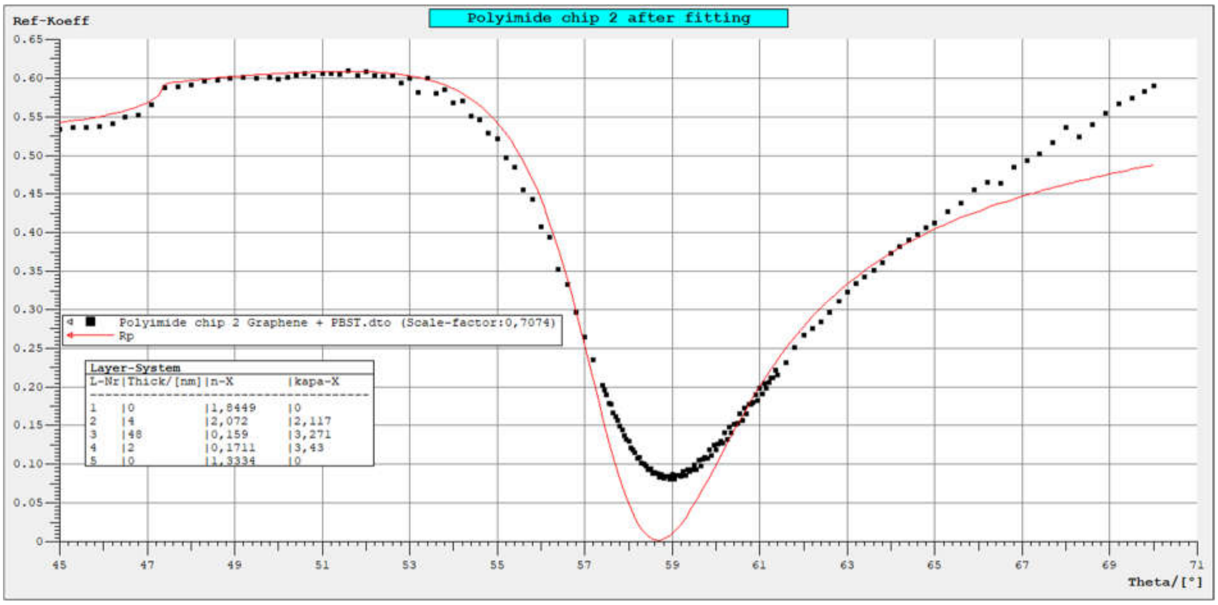

```
Layer-System
L-Nr|Thick/[nm]|n-X        |kapa-X
-----------------------------------
1   |0         |1,8449     |0
2   |4         |2,072      |2,117
3   |48        |0,159      |3,271
4   |2         |0,1711     |3,43
5   |0         |1,3334     |0
```

Figure 72. Fitting of the simulated sensogram with the measured one by changing only the optical constants of the graphene layer. The fitting was done with an iterative simulation in WinsPall 3.01

From **Figure 72** it is visible how the simulated angle scan represented by the red curve, has a plasmonic resonance falling at 2° more compared to the measured resonance peak. Since all the parameters of the polyimide chip were known, the software was allowed to fit only the n and k parameters of graphene's refractive index. In **Figure 73** it can be seen how the new optical parameters of the graphene are n = 0.1711 and k = 3.43, which differ too much from the initial values present in **Figure 72**. This is might be due again to a distortion of the polyimide layer that is causing the plasmonic resonance to deviate from the ideal resonance conditions.

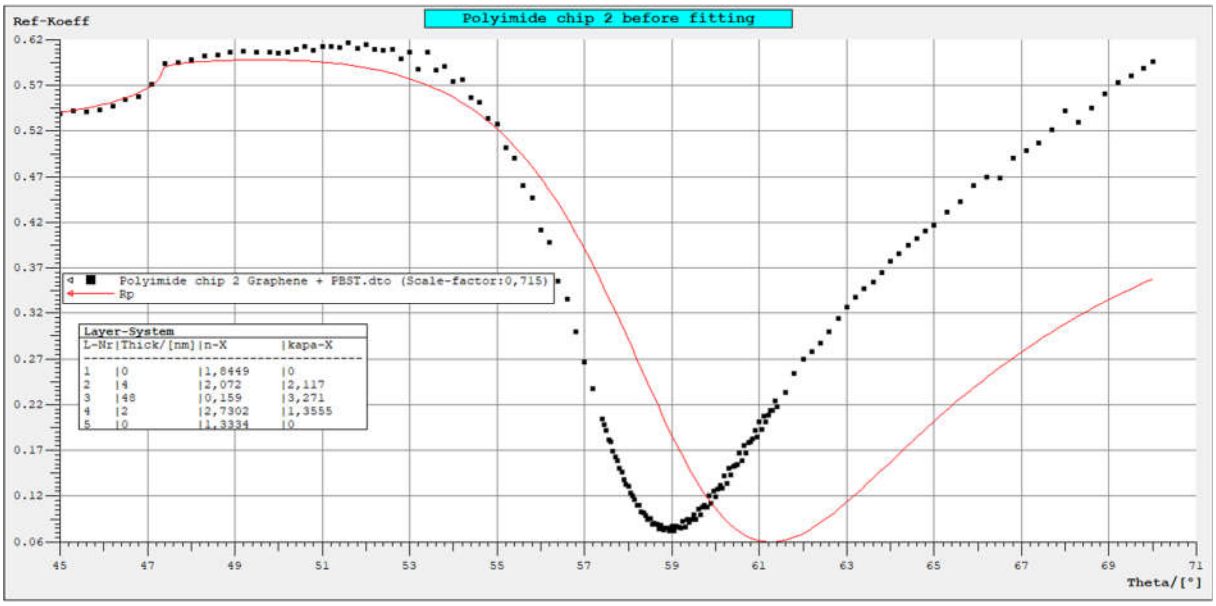

Layer-System

L-Nr	Thick/[nm]	n-X	kapa-X
1	0	1,8449	0
2	4	2,072	2,117
3	48	0,159	3,271
4	2	2,7302	1,3555
5	0	1,3334	0

Figure 69. Comparison between the angle scan of the polyimide chip 2 in PBST media and the simulated angle scan with the software WinSpall 3.01.

The SPR scans performed on the polyimide chip 6 during the kinetic measurements are displaying in **Figure 74** an increase of the signal noise over time. In the smoothed sensorgram of **Figure 75** a slight shift towards higher angle is visible between the two scans measured before and after the elution of the nanobody, confirming the successful formation of the HER2-ECD adlayer.

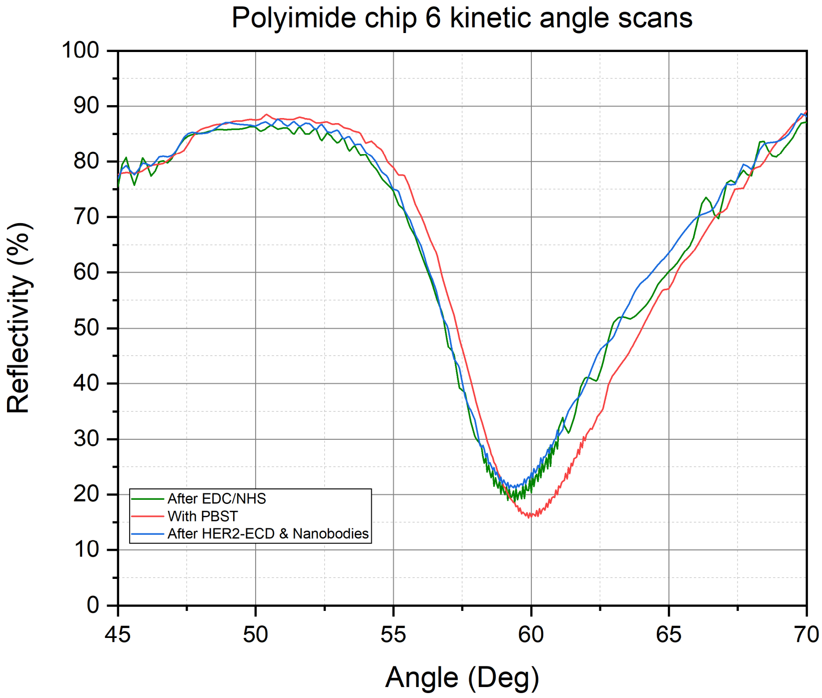

Figure 74. Polyimide chip 6 SPR angle scans measured in PBBST before the surface activation, after the EDC/NHS surface activation and after the HER2-ECD functionalization and nanobody elution

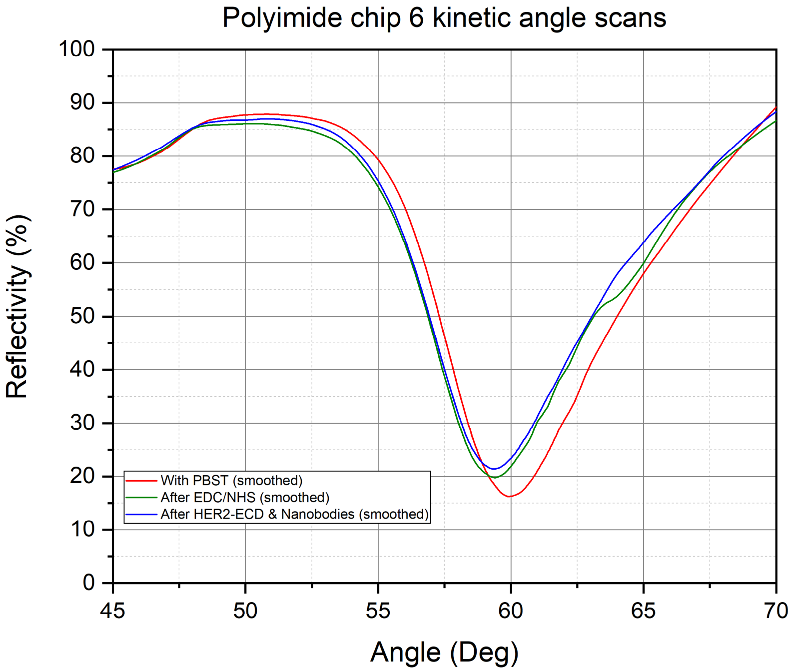

Figure 75. Polyimide chip 6 Smoothed SPR angle scans measured in PBBST before the surface activation, after the EDC/NHS surface activation and after the HER2-ECD functionalization and nanobody elution

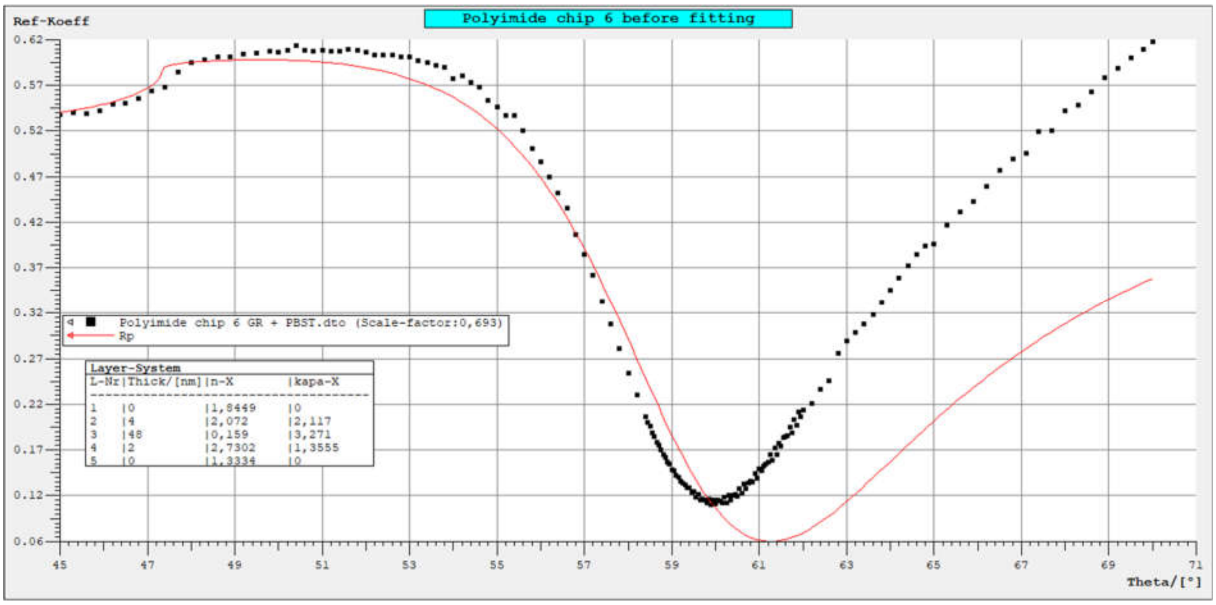

Layer-System

L-Nr	Thick/[nm]	n-X	kapa-X
1	0	1,8449	0
2	4	2,072	2,117
3	48	0,159	3,271
4	2	2,7302	1,3555
5	0	1,3334	0

Figure 70. Comparison between the angle scan of the polyimide chip 6 in PBST media and the simulated angle scan with the software WinSpall 3.01.

In **Figure 76**, the SPR angle measured in PBST was compared with the simulated one. The difference between the resonance dip angles this time was around 1°, confirming a better alignment of the polyimide chip. In **Figure 77** the fitting of the simulated angle scan generated new optical constants of the graphene that are closer to the initial one, showing an overall improvement of the biosensor, which might be connected to the reduced mechanical stress after the use of the double sided tape at the interface between the polyimide chip and the fluidic cell instead of the PDMS layer.

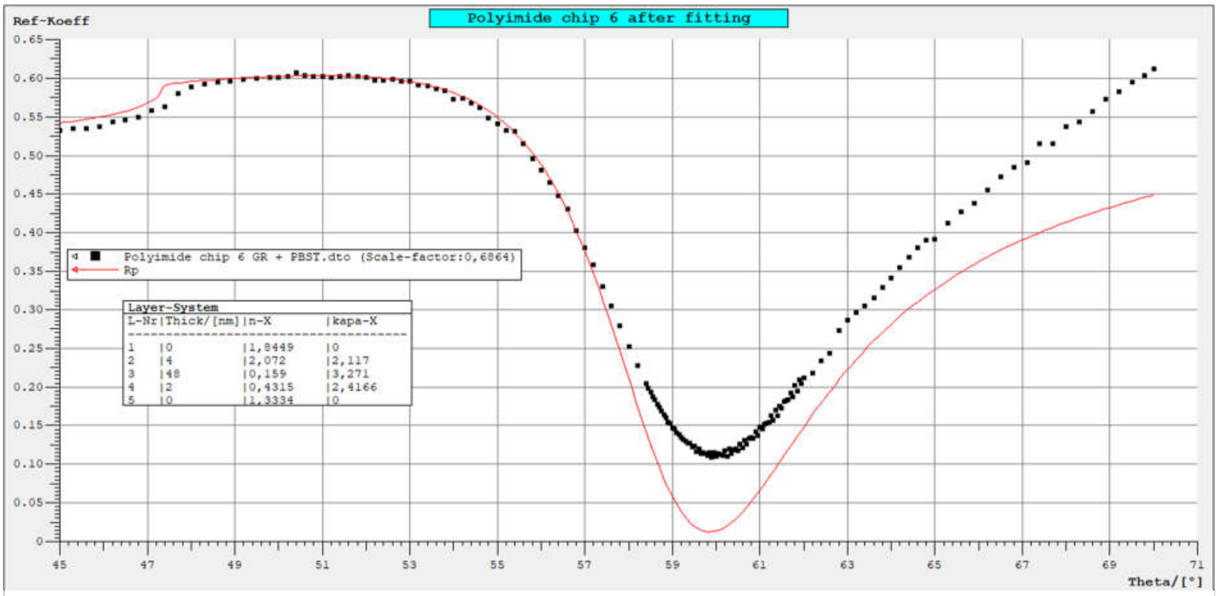

Layer-System

L-Nr	Thick/[nm]	n-X	kapa-X
1	0	1,8449	0
2	4	2,072	2,117
3	48	0,159	3,271
4	2	0,4315	2,4166
5	0	1,3334	0

Figure 71. Fitting of the simulated sensogram with the measured one by changing only the optical constants of the graphene layer. The fitting was done with an iterative simulation in WinsPall 3.01.

CHAPTER 4 CONCLUSIONS AND OUTLOOKS

In this thesis work the use of the ellipsometry technique was successfully implemented to study and characterize the optical constants of graphene functionalized SPR substrate. The optical constants for the gold and titanium oxide layers were accurately measured and employed to determine the correct layer thickness to be deposited on top of the transparent polyimide chip. The graphene optical constants were successfully calculated by fitting the measured ellipsometric values with the graphene's layer thickness obtained from the AFM measurements. An optimized graphene transfer protocol provided very clean graphene transfers, which were used to perform a thorough characterization of the graphene layer lateral distribution with the AFM and optical microscopy. The accurately determined substrate's optical and physical constants were used to generate exact simulations of the substrate plasmonic resonance scans, which were used as a reference to compare the polyimide chips, which were employed as a substitute for the more expensive and fragile high refractive index glass. This robust analytical protoocol was used as a powerful tool to solve all the challenges related to the use of a flexible polyimide layer, in particular the distortions of the polyimide layer and the instability of the reflectivity signal due to the moisture absorption and mechanical stress. The development of an optimal surface modification based of the EDC/NHS protocol was successfully implemented for the bio-functionalization of the HER2-ECD biomarker on the graphene surface. The so obtained biosensor was able to detect two different novel nanobodies receptors, which were eluted through a microfluidic system over the chip in a wide range of concentrations from 1 pM up to the 1 μM.

Further optimization of the newly developed 2D bio-nanointerface would require employment of high refractive index glass to increase the stability of the signal and the accuracy of the measurements. As discussed in this work, heterogeneities of 2D layers affect the SPR response and one must take it into account when performing an SPR analysis aimed at studying the interactions occurring at such interfaces. Further improvements in the physical models for graphene and other 2D materials require more accurate studies of influences arising from stacks of multiple layers of 2D materials and other physical and chemical aspects affecting both the electronic and optical properties. This way the sensor chip performance could be studied in relation with different nanoengineered 2D interfaces and sensor configurations. The direct functionalization of the graphene surface with the nanobodies as receptor molecules will be the next step to provide a sensing platform capable of providing an enhanced sensitivity toward the detection of HER2-ECD biomarker protein, as its higher molecular weight would lead to a steeper change of the plasmonic resonance angular shift. The SPR-based biosensor developed in this thesis work is a robust and reliable tool to test and implement novel analytical tools featuring also the characterization of the kinetic parameters stemming from the interaction between a cancer biomarker protein and the capturing nanobodies. A SPR optimized 2D bio-nanointerface, such as those shown in this work, are expected to be an advantageous outcome, as a precursor to the development of highly optimized electrical biosensors for point-of-care applications.

ACKNOWLEDGMENT

I would like to express my special thanks to Prof. Sven Ingebrandt for letting me be part of the IWE1 institute at RWTH Aachen. My special thanks also to Dr. Vivek Pachauri and Dr. Federico Polo for lending me supervision and support during my research work and thesis writing. I would like to pay my special regards to Prof. Alessandro Angelini from Ca' Foscari University of Venice for providing me with the nanobodies that I employed in the kinetic analyses. I am also grateful to Dr. Stefan Scholz from the IHT institute at RWTH Aachen for introducing and helping me with the optical characterizations and ellipsometry analyses. I would like to recognize the invaluable assistance provided by Mr. Jochen Heiss, Ms. Dorothee Breuer and Ms. Ewa Sekula, whose work was crucial for the development of the sensor substrate and the functionalization protocols.

Bibliography

1. Oh, D.Y. and Y.J. Bang, *HER2-targeted therapies - a role beyond breast cancer.* Nature Reviews Clinical Oncology, 2020. **17**(1): p. 33-48.
2. Organization, W.H., *Latest global cancer data: Cancer burden rises to 18.1 million new cases and 9.6 million cancer deaths in 2018.* International Agency for Research on Cancer, 2018. **Press Release 263**.
3. Organization, W.H., *https://gco.iarc.fr/today/online-analysis-pie?v=2018&mode=cancer&mode_population=continents&population=900&populations=900&key=total&sex=0&cancer=39&type=0&statistic=5&prevalence=0&population_group=0&ages_group%5B%5D=0&ages_group%5B%5D=17&nb_items=7&group_cancer=1&include_nmsc=1&include_nmsc_other=1&half_pie=0&donut=0&population_group_globocan_id=*. 2018.
4. Henry, N.L. and D.F. Hayes, *Cancer biomarkers.* Molecular Oncology, 2012. **6**(2): p. 140-146.
5. Allegra, C.J., et al., *American Society of Clinical Oncology Provisional Clinical Opinion: Testing for KRAS Gene Mutations in Patients With Metastatic Colorectal Carcinoma to Predict Response to Anti-Epidermal Growth Factor Receptor Monoclonal Antibody Therapy.* Journal of Clinical Oncology, 2009. **27**(12): p. 2091-2096.
6. Organization, W.H., *https://gco.iarc.fr/today/online-analysis-pie?v=2018&mode=cancer&mode_population=continents&population=900&populations=900&key=total&sex=2&cancer=39&type=0&statistic=5&prevalence=0&population_group=0&ages_group%5B%5D=0&ages_group%5B%5D=17&nb_items=7&group_cancer=1&include_nmsc=1&include_nmsc_other=1&half_pie=0&donut=0&population_group_globocan_id=*. 2018.
7. Tabatabaeian, H., S. Sadeghi, and Z. Hojati, *The Molecular Role of Human Epidermal Growth Factor 2 (HER2) In Breast Cancer.* International Journal of Analytical, Pharmaceutical and Biomedical Sciences, 2015. **4**: p. 78-91.
8. Chang, J.C., *HER2 inhibition: From discovery to clinical practice.* Clinical Cancer Research, 2007. **13**(1): p. 1-3.
9. Carney, W.P., et al., *Monitoring the Circulating Levels of the HER2/neu Oncoprotein in Breast Cancer.* Clinical Breast Cancer, 2004. **5**(2): p. 105-116.
10. Hicks, D.G. and S. Kulkarni, *HER2+breast cancer.* American Journal of Clinical Pathology, 2008. **129**(2): p. 263-273.
11. Schubert, M., *Infrared ellipsometry on semiconductor layer structures - Phonons, plasmons, and polaritons - Introduction*, in *Infrared Ellipsometry on Semiconductor Layer Structures: Phonons, Plasmons, and Polaritons*. 2004, Springer-Verlag Berlin: Berlin. p. 1-6.
12. de Mol, N. and M. Fischer, *Surface Plasmon Resonance: Methods and Protocols*. 2010.
13. Horn, N. and M. Kreiter, *Plasmon Spectroscopy: Methods, Pitfalls and How to Avoid Them.* Plasmonics, 2010. **5**(4): p. 331-345.
14. Jung, L.S., et al., *Quantitative Interpretation of the Response of Surface Plasmon Resonance Sensors to Adsorbed Films.* Langmuir, 1998. **14**(19): p. 5636-5648.
15. Salamon, Z., H.A. Macleod, and G. Tollin, *Surface plasmon resonance spectroscopy as a tool for investigating the biochemical and biophysical properties of membrane protein systems .1. Theoretical principles.* Biochimica Et Biophysica Acta-Reviews on Biomembranes, 1997. **1331**(2): p. 117-129.

16. Homola, J., *Present and future of surface plasmon resonance biosensors.* Analytical and Bioanalytical Chemistry, 2003. **377**(3): p. 528-539.
17. Islam, M.S., et al., *Comparison of Performance Parameters for Conventional and Localized Surface Plasmon Resonance Graphene Biosensors*, in *2011 Annual International Conference of the Ieee Engineering in Medicine and Biology Society*. 2011, Ieee: New York. p. 1851-1854.
18. Novoselov, K.S., et al., *Electric field effect in atomically thin carbon films.* Science, 2004. **306**(5696): p. 666-669.
19. De Arco, L.G., et al., *Synthesis, Transfer, and Devices of Single- and Few-Layer Graphene by Chemical Vapor Deposition.* Ieee Transactions on Nanotechnology, 2009. **8**(2): p. 135-138.
20. Yang, G., et al., *Structure of graphene and its disorders: a review.* Science and Technology of Advanced Materials, 2018. **19**(1): p. 613-648.
21. Koppens, F.H.L., D.E. Chang, and F.J.G. de Abajo, *Graphene Plasmonics: A Platform for Strong Light-Matter Interactions.* Nano Letters, 2011. **11**(8): p. 3370-3377.
22. Qi, P.W., et al., *Wax-assisted crack-free transfer of monolayer CVD graphene: Extending from standalone to supported copper substrates.* Applied Surface Science, 2019. **493**: p. 81-86.
23. Sam, S., et al., *Semiquantitative Study of the EDC/NHS Activation of Acid Terminal Groups at Modified Porous Silicon Surfaces.* Langmuir, 2010. **26**(2): p. 809-814.
24. Wang, C., et al., *Different EDC/NHS Activation Mechanisms between PAA and PMAA Brushes and the Following Amidation Reactions.* Langmuir, 2011. **27**(19): p. 12058-12068.
25. Jans, H., et al., *Impact of pre-concentration to covalently biofunctionalize suspended nanoparticles.* Nanotechnology, 2010. **21**(34): p. 8.
26. Fischer, M.J.E., *Amine Coupling Through EDC/NHS: A Practical Approach*, in *Surface Plasmon Resonance: Methods and Protocols*, N.J. Mol and M.J.E. Fischer, Editors. 2010, Humana Press: Totowa, NJ. p. 55-73.
27. Yao, Y.X., et al., *Histogram method for reliable thickness measurements of graphene films using atomic force microscopy (AFM).* Journal of Materials Science & Technology, 2017. **33**(8): p. 815-820.
28. Weber, J.W., V.E. Calado, and M.C.M. van de Sanden, *Optical constants of graphene measured by spectroscopic ellipsometry.* Applied Physics Letters, 2010. **97**(9).
29. Kolomenski, A., et al., *Propagation length of surface plasmons in a metal film with roughness.* Applied Optics, 2009. **48**(30): p. 5683-5691.